

**AN EXAMINATION OF EXTRATROPICAL CYCLONE SENSITIVITY TO ENVIRONMENTAL  
VARIABILITY**

**by**

**Gregory E. Tierney**

**A dissertation submitted in partial fulfillment  
of the requirements for the degree of  
Doctor of Philosophy  
(Atmospheric, Oceanic, and Space Sciences)  
in the University of Michigan  
2017**

**Doctoral Committee:**

**Associate Professor Christiane Jablonowski, Co-Chair  
Derek J. Posselt, Jet Propulsion Laboratory, Co-Chair  
Associate Professor Mark G. Flanner  
Associate Professor Seth D. Guikema  
Professor Richard B. Rood**

Gregory E. Tierney

gtierney@umich.edu

ORCID iD: 0000-0001-9981-7552

© Gregory Tierney 2017  
All Rights Reserved

*For Mom and Dad*

## **Acknowledgments**

By convention, every dissertation ever written lists a single author: the student who the primary designer, creator, and writer of that work. However, no dissertation is truly possible through the work of just one person. Just as it takes a village to raise a child, it also takes a village to write a dissertation – and this dissertation is no different. In conceptualizing and designing the experiments within this dissertation, along with guidance on research issues big and small, I owe an enormous debt of gratitude to Derek, who has endured many weekly meetings over the past number of years, whether in person or via Skype. In asking me during my REU experience 7 years ago whether I'd like to try my hand at modeling, I'm not sure he knew the Pandora's Box he had opened: the litany of questions, the tangential research directions, the (sometimes wild) explanations. His guidance and continual support has kept me going even in times when I thought that perhaps this dissertation would never be written. Even after moving to JPL, he has continued to provide support from afar as I completed my degree, along with numerous opportunities to network and travel to various conferences. Special thanks also must go out to Christiane, who was kind enough to step in as an additional advisor once Derek moved. Her willingness to take on an additional student made the transition during the final year of my studies much smoother. Her expertise in modeling configurations and the mechanics of numerical models has made my dissertation much more complete than it would have otherwise been, and has reminded me not to model blindly. Thank you also the rest of my committee – Mark, Ricky, and Seth, who have provided me with support and guidance on this work as well; and in Ricky's case, an office during my first stay at Michigan as an REU. Thank you also to

professors outside of Michigan, those who helped lead me on my path here. Prof. Peter Gierasch, who took a chance offering a summer research position to a freshman who didn't really know what he had gotten into. And of course, the professors in EAS at Cornell, especially Wysocki, Colucci, and Art, who have inspired me to try and make atmospheric science as enjoyable as they did – teaching with passion and purpose. I can only hope to pass on my passion for this field as you have.

Of course, the support I've received extends far beyond professors and mentors. At its most ideal, graduate school is also a community effort at the student level – and I have had many friends along the way that have made it ideal, even when it didn't seem to be. Most notably, those in the AOSS Lab have had to sit through many pointless questions that often lead nowhere, muttering at broken code, and oodles of sports talk. David, Sam, Fei, Juan, Annareli, and Omar: thank you so much for putting up with me these past 5 years (and more for some of you). David, I'm sorry for all of the WRF questions, especially during the REU – I think I've got a better handle on how it works now... maybe. Juan, your Purdue is still showing, but that's alright. Outside the classroom and office, broomball and softball with Red Zeppelin gave me a competitive outlet, and provided many great championship memories and some hilarious moments. Even more, the community of graduate students outside of my lab has allowed me to keep my sanity when I thought I might lose it. Stacey and Jared, thanks so much for dealing with my crazy talk at times. Mary, thanks for listening to all of my random GUSStO ideas over the years. I'm so proud of what we were able to build to strengthen the graduate community – I can't wait to see you as the NOAA administrator. Special thanks also to the staff within AOSS/CLaSP: Sandy, all your help in navigating the paperwork of graduate school is indispensable. Tonya, thanks for always providing a laugh... and the reimbursements! Marti, thanks for always making

sure that everything was cared for in the building – your help with MGU accommodations always made the early morning setup much easier than it should’ve been. There are many more staff members that I haven’t mentioned, I’m sure, but to fully recognize everyone would result in acknowledgments that are dissertation-length by themselves.

Finally, to my family – who been there every step of the way, and will continue to be there as I go forward – there is a debt a gratitude beyond words. Nothing that I’ve accomplished has been without their love and support. Through struggles both familiar and unfamiliar, they have listened and tried to help me, whether through their own advice, or through letting me talk myself in circles about it. I can’t list anything here would possibly do justice to the love shown to me by my family, especially my Aunt Dianne, my grandparents, and of course my Mom and Dad. Please know that everything I’ve accomplished is because of your guidance and all that I’ve learned from you, the most influential teachers in my life.

When I was little and my grandparents saw me after school, they would often ask me if I had learned anything that day. In hindsight, the amount of times I answered “no” must have been a lie. Grandma and Grandpa – it seems I must have learned some things. I’ve learned not only facts, numbers, and statistics, but also how to be a better person, how you should always attempt to improve yourself, and to try and raise up those around you with your support whenever possible – these are perhaps the greatest lessons someone can be taught. And dear reader, while you probably won’t learn those types of things here, I hope you too learn something while reading this dissertation.

## TABLE OF CONTENTS

<b>Dedication</b> .....	<b>ii</b>
<b>Acknowledgments</b> .....	<b>iii</b>
<b>List of Tables</b> .....	<b>viii</b>
<b>List of Figures</b> .....	<b>ix</b>
<b>Abstract</b> .....	<b>xiii</b>
<b>Chapter 1: Introduction</b> .....	<b>1</b>
1-1: Background Literature .....	1
1-2: Dissertation Outline .....	7
<b>Chapter 2: Methodology</b> .....	<b>13</b>
2-1: Methodology Survey .....	13
2-2: Model Configuration .....	17
2-3: Model Initialization Procedure .....	18
2-4: Experiment Design .....	22
<b>Chapter 3: Evaluation and Extension of ETC Sensitivity Experiments on an <math>f</math>-plane</b> .....	<b>29</b>
3-1: Introduction .....	29
3-2: Methods and Experiment Design .....	31
3-3: Univariate Sensitivity Results .....	32
3-3.1 <i>Dry Simulations</i> .....	32
3-3.2 <i>Moist Simulations</i> .....	34
3-4: Bivariate Sensitivity Results .....	36
3-5: The Role of Diabatic Heating .....	39
3-6: Conclusions .....	44
<b>Chapter 4: Evaluation of ETC Sensitivity Using Latitudinally-Varying Coriolis Configurations</b> .....	<b>58</b>
4-1: Introduction .....	58
4-2: Methods and Experiment Design .....	61
4-3: Univariate Sensitivity Results .....	62
4-3.1 <i>Dry Simulations</i> .....	62
4-3.2 <i>Moist Simulations</i> .....	64
4-4: Bivariate Sensitivity Results .....	66
4-5: Inclusion of a Spherical Coriolis Configuration .....	67
4-6: Discussion .....	68

4-7: Comparison of Beta-Plane and f-Plane Results -----	74
4-8: Conclusions -----	76
<b>Chapter 5: The Impact of Radiative Processes on Extratropical Cyclones -----</b>	<b>94</b>
5-1: Introduction -----	94
5-2: Methods and Experiment Design -----	96
5-3: Univariate Sensitivity Results -----	98
5-4: Bivariate Sensitivity Results -----	101
5-5: Discussion -----	104
5-6: Understanding the Root of Radiative Effects -----	110
5-7: Conclusions -----	113
<b>Chapter 6: Conclusions -----</b>	<b>133</b>
<b>References -----</b>	<b>139</b>

## List of Tables

<b>Table 2-1.</b> Vertical levels used in the simulations.-----	26
<b>Table 2-2.</b> Conversion table between reference temperatures (southern boundary surface initialization temperatures) and initial surface temperature at the center of the domain. ----	26
<b>Table 3-1.</b> F-plane experiment descriptions. -----	48
<b>Table 3-2.</b> Time to maximum EKE and minimum SLP for dry univariate sensitivity tests (in hours)-----	48
<b>Table 3-3.</b> Time to maximum EKE and minimum SLP for moist univariate sensitivity tests (in hours)-----	48
<b>Table 4-1.</b> Beta-plane experiment descriptions. -----	79
<b>Table 5-1.</b> Radiation experiment descriptions. -----	116

## List of Figures

<b>Figure 1-1.</b> Outgoing longwave radiation product from a model-simulated extratropical cyclone off of the East Coast of the United States in November 2006. The classical “comma head” structure of the cloud field in ETCs is visible in white. ....	11
<b>Figure 1-2.</b> Schematic demonstrating the position of the Warm Conveyor Belt (in orange) within an extratropical cyclone. Adapted from the COMET module on mesoscale banded precipitation (courtesy UCAR MetEd program). ....	12
<b>Figure 2-1.</b> Initialization cross-sections of the jet profile (Figure 2-1a) and temperature (Figure 2-1b) for the control run, with a southern boundary surface initialization temperature of 300 K and a jet amplitude factor of 1.0, on an <i>f</i> -plane. ....	27
<b>Figure 2-2.</b> Environmental initialization for the perturbed parameter in the univariate baroclinicity test (Figure 2-1a, left), where the amplitude of the jet profile is modified; and for the univariate bulk temperature sensitivity test (Figure 2-1b, right), where temperature is changed within the domain. ....	28
<b>Figure 3-1.</b> Column-summed EKE averaged within the entire domain (dashed lines) and minimum SLP (solid lines) for the 6 runs spanning the dry baroclinicity univariate test (a) and dry bulk temperature univariate test (b) on an <i>f</i> -plane. ....	49
<b>Figure 3-2.</b> Full domain-averaged column-summed EKE (dashed lines) and minimum SLP (solid lines) for the 6 runs spanning the moist baroclinicity univariate test (Figure 3-2a, left panel) and moist bulk temperature univariate test (Figure 3-2b, right panel) on an <i>f</i> -plane. ....	50
<b>Figure 3-3.</b> Plan view map of the distribution of EKE at time of maximum EKE for three ETCs in the bulk temperature test on an <i>f</i> -plane. Initial surface temperature at the center of the domain is given in each title, and correspond to the southern boundary initialization temperatures of 292 K (left), 300 K (middle), and 308 K (right). Bolded contour in each figure is representative of the storm size diagnostic used in the bivariate tests. On the ordinate axis, 0 indicates the northern edge of the model domain. ....	51
<b>Figure 3-4.</b> Minimum SLP (in hPa) during the lifetime of each ETC tested in the bivariate sensitivity test on an <i>f</i> -plane. The 9 point minimum SLP is determined by taking the average SLP of a 3 by 3 gridpoint box centered on the minimum SLP point in the domain. ....	52
<b>Figure 3-5.</b> Maximum value of the average column-summed EKE (in $(J/m^2)*10^5$ ) during the lifetime of each ETC in the bivariate sensitivity test on an <i>f</i> -plane. ....	53
<b>Figure 3-6.</b> Storm size (in $km^2$ ) at the times of maximum EKE (Figure 3-6a, left panel) and minimum SLP (Figure 3-6b, right panel) for the bivariate experiment on an <i>f</i> -plane. Storm size is determined by taking the area within a threshold contour with a value of the minimum SLP of the ETC at that time plus 30 hPa. ....	54
<b>Figure 3-7.</b> Frontal maps of three selected ETCs in each univariate test on an <i>f</i> -plane at 24 hours after the first precipitation, with overlaid precipitation contours. Fronts are displayed by contouring a specific equivalent potential temperature value representative of the frontal	

area at intervals of 100 hPa. Overlaid precipitation hatching indicates areas where precipitation rates of over 1 mm hr<sup>-1</sup> are recorded for convective (red hatching) and non-convective (blue hatching) modes of precipitation. Figure 3-7a (top row) displays the 292 K, 300 K, and 308 K runs from the bulk temperature univariate test, while Figure 3-7b (bottom row) displays the 0.6, 1.0, and 1.4 runs from the baroclinicity univariate test..... 55

**Figure 3-8.** Averaged latent heat release (LHR) profiles in a 40 by 40 gridpoint box centered on the cyclone center. For each of the two univariate experiments on an *f*-plane, contributions to the LHR profiles are broken down into microphysical contributions (3-8a for the univariate bulk temperature cases, 3-8c for the univariate baroclinicity cases) and cumulus parameterization contributions (3-8b for the univariate bulk temperature cases, 3-8d for the univariate baroclinicity cases) ..... 56

**Figure 3-9.** Potential vorticity anomaly analysis (in PVU) midway through development (as measured by EKE) for both the 292K and 308 K simulations on an *f*-plane, with sea level pressure contours overlaid (in hPa). PV anomalies are taken relative to the first 12 hours of each simulation. .... 57

**Figure 4-1.** Magnitudes of the Coriolis parameter approximations (*f* plane in red, beta-plane in blue) and the calculated Coriolis parameter (for a sphere), for latitudes within the idealized channel domain used for sensitivity experiments..... 80

**Figure 4-2.** Average column-summed EKE (dashed lines) and minimum SLP (solid lines) for the 6 runs spanning the dry baroclinicity univariate test (Figure 4-2a, top panel) and dry bulk temperature univariate test (Figure 4-2b, bottom panel) on a beta-plane..... 81

**Figure 4-3.** Average column-summed EKE (dashed lines) and minimum SLP (solid lines) for the 6 runs spanning the dry baroclinicity univariate test on a beta-plane, run without surface fluxes. .... 82

**Figure 4-4.** Average column-summed EKE (dashed lines) and minimum SLP (solid lines) for the 6 runs spanning the moist baroclinicity univariate test (Figure 4-4a, top panel) and moist bulk temperature univariate test (Figure 4-4b, bottom panel) on a beta-plane..... 83

**Figure 4-5.** Minimum SLP (in hPa) during the lifetime of each ETC tested in the bivariate sensitivity test on a beta-plane. The 9pt minimum SLP is determined by taking the average SLP of a 3 by 3 gridpoint box centered on the minimum SLP point in the domain. .... 84

**Figure 4-6.** Maximum value of the average column-summed EKE (in (J/m<sup>2</sup>)\*10<sup>5</sup>) during the lifetime of each ETC tested in the bivariate sensitivity test on a beta-plane..... 85

**Figure 4-7.** Average column-summed EKE (dashed lines) and minimum SLP (solid lines) for the 6 runs spanning the moist baroclinicity univariate test (Figure 4-7a, top panel) and moist bulk temperature univariate test (Figure 4-7b, bottom panel), run with a spherical Coriolis configuration..... 86

**Figure 4-8.** Averaged (over the full domain and entire simulation) values of convective precipitation (mm/day, Figure 4-8a), non-convective precipitation (mm/day, Figure 4-8b), and convective percentage of precipitation (Figure 4-8c) for each ETC in the bivariate sensitivity test on a beta-plane..... 87

**Figure 4-9.** Times A-D of the four-panel analysis overlaid on the average column-summed EKE (dashed lines) and minimum SLP (solid lines) for the 6 runs spanning the moist bulk temperature univariate test on a beta-plane. Time D is at the time of maximum EKE. .... 88

<b>Figure 4-10.</b> Four-panel PV anomaly and precipitable water vapor analysis, conducted at Times A, B, and C (indicated in Figure 4-9) and at the time of maximum EKE, with overlaid sea level pressure contours (hPa) for the 292 K bulk temperature case on a beta-plane.....	89
<b>Figure 4-11.</b> Four-panel PV anomaly and precipitable water vapor analysis, conducted at Times A, B, and C (indicated in Figure 4-9) and at the time of maximum EKE, with overlaid sea level pressure contours (hPa) for the 308 K bulk temperature case on a beta-plane.....	90
<b>Figure 4-12.</b> Maximum EKE response to changes in temperature/moisture content for both <i>f</i> -plane and beta-plane configurations. The jet amplitude factor is equal to 1.0 for all runs. ..	91
<b>Figure 4-13.</b> Cross-section of initial domain temperature differences (in K) between the beta-plane and <i>f</i> -plane configurations. Differences are taken for the control case at a bulk temperature of 300 K and jet amplitude factor of 1.0, with the southern boundary on left and northern boundary on the right of the figure. Red (blue) colors indicate that the beta-plane simulation is warmer (colder) than its <i>f</i> -plane analog. ....	92
<b>Figure 4-14:</b> Sketch (not to scale) demonstrating the three regimes of extratropical cyclogenesis present in the parameter space, overlaid on a generalization of the maximum EKE response to temperature. ....	93
<b>Figure 5-1.</b> Figure 5-1a, left: Difference of zonally-averaged 700 hPa temperatures (K) between one-quarter and three-quarters of the way into the domain (from the south) for the univariate baroclinicity sensitivity test. Figure 5-1b, right: Full-domain averaged temperatures (K) for the univariate bulk temperature sensitivity test. ....	117
<b>Figure 5-2.</b> Average column-summed EKE (dashed lines) and minimum SLP (solid lines) for the 6 runs spanning the moist baroclinicity univariate test on a beta-plane with radiative processes enabled. ....	118
<b>Figure 5-3.</b> Average column-summed EKE (dashed lines) and minimum SLP (solid lines) for the 6 runs spanning the moist bulk temperature univariate test on a beta-plane with radiative processes enabled. ....	119
<b>Figure 5-4.</b> Longitudinally-averaged atmospheric profile taken one-quarter of the way into the domain (from the south) at initialization of the 304 K simulation on a beta-plane with radiative processes enabled. Within this sounding, plotted on a Skew-T Log-P diagram, the black line indicates the environmental temperature and blue line indicates the environmental dewpoint. The red dashed line is the theoretical temperature of a parcel raised from the surface and allowed to freely convect, and indicates the boundary of integration for CAPE, calculated as the area between the black and red lines.....	120
<b>Figure 5-5.</b> Average column-summed EKE (dashed lines) and minimum SLP (solid lines) for 11 runs spanning (in steps of 2 K) the moist beta-plane bulk temperature univariate test with radiative processes. ....	121
<b>Figure 5-6.</b> Maximum EKE response to changes in temperature/moisture content for beta-plane configurations with and without radiative processes enabled. The jet amplitude factor is equal to 1.0 for all runs.....	122
<b>Figure 5-7.</b> Minimum SLP (in hPa) during the lifetime of each ETC tested in the bivariate sensitivity test on a beta-plane with radiative processes enabled. The 9 point minimum SLP is determined by taking the average SLP of a 3 by 3 gridpoint box centered on the minimum SLP point in the domain. ....	123

**Figure 5-8.** Maximum value of the full-domain averaged column-summed EKE (in  $(J/m^2)*10^5$ ) during the lifetime of each ETC tested in the bivariate sensitivity test on a beta-plane with radiative processes enabled. .... 124

**Figure 5-9.** Temporally and spatially averaged (across the entire domain) values of convective precipitation (mm/day, Figure 5-9a), non-convective precipitation (mm/day, Figure 5-9b), and convective percentage of precipitation (Figure 5-9c) for each ETC in the bivariate sensitivity test on a beta-plane with radiative processes enabled. .... 125

**Figure 5-10.** Temporally (over the duration of the simulation) and spatially (from 25 – 72°N, between the 100<sup>th</sup> and 300<sup>th</sup> row of grid points within the model) averaged values of convective precipitation (mm/day, Figure 5-10a), non-convective precipitation (mm/day, Figure 5-10b), and convective percentage of precipitation (Figure 5-10c) for each ETC in the bivariate sensitivity test on a beta-plane with radiative processes enabled. .... 126

**Figure 5-11.** Longitudinally-averaged atmospheric profiles taken one-quarter of the way into the domain (from the south) at initialization of the 288 K simulation (Fig. 5-11a, dashed lines), 00Z on Day 5 of the 288K simulation (Fig. 5-11a, solid lines), initialization of the 296 K simulation (Fig. 5-11b, dashed lines), and 00Z on Day 5 of the 296K simulation (Fig. 5-11b, solid lines). .... 127

**Figure 5-12.** Four-panel PV anomaly and precipitable water vapor analysis of the 292 K bulk temperature case on a beta-plane with radiative processes enabled, conducted at Times A-C (indicated at the top of the figure), with overlaid sea level pressure contours (hPa). .... 128

**Figure 5-13.** Four-panel PV anomaly and precipitable water vapor analysis of the 308 K bulk temperature case on a beta-plane with radiative processes enabled, conducted at Times A-D (indicated at the top of the figure), with overlaid sea level pressure contours (hPa). .... 129

**Figure 5-14.** Longitudinally-averaged atmospheric profiles taken one-quarter of the way into the domain (from the south) at 06 Z on Day 7 of the 308 K simulation. Within these soundings, plotted on Skew-T Log-P diagrams, black lines indicate the environmental temperature and blue lines indicate the environmental dewpoint. Red dashed lines are the theoretical temperatures of parcels raised from the surface and allowed to freely convect, and indicate the boundary of integration for CAPE, calculated as the area between the black and red lines. .... 130

**Figure 5-15.** Average column-summed EKE (dashed lines) and minimum SLP (solid lines) for the 6 runs spanning the moist baroclinicity univariate test with radiation enabled (Fig. 5-15a), without cloud radiative forcing (Fig. 5-15b), without interactions with water in all forms, including vapor (Fig. 5-15c), and without any radiative processes (Fig. 5-15d). All experiments presented are run on a beta-plane. .... 131

**Figure 5-16.** Longitudinally-averaged atmospheric profiles taken one-quarter of the way into the domain (from the south) at 00 Z on Day 5 of the 300 K simulation, without radiative interactions with water (Fig. 5-16a), and without all radiative processes (Fig. 5-16b). Within these soundings, plotted on Skew-T Log-P diagrams, black lines indicate the environmental temperature and blue lines indicate the environmental dewpoint. Red dashed lines are the theoretical temperatures of parcels raised from the surface and allowed to freely convect, and indicate the boundary of integration for CAPE, calculated as the area between the black and red lines. .... 132

## **Abstract**

As primary drivers of synoptic-scale midlatitude atmospheric variability, extratropical cyclones (ETCs) are an important influence on the day-to-day weather in the most populated regions of the planet. Given their environmental connections at multiple length scales, the impacts of ETCs in a future climate are difficult to predict. Some facets of a future climate, such as a weaker equator-to-pole temperature gradient, may weaken ETCs, while other factors, such as an increase in atmospheric moisture content, may strengthen ETCs. Separating these effects is complicated by incomplete observational coverage and the nonlinear response of the system to environmental perturbations. Therefore, we use numerical modeling to systematically explore ETC response to changes in environmental characteristics.

Improving upon previous unrealistic and unphysical perturbation schemes, we developed a novel scheme for perturbing environmental temperature (as a proxy for moisture) and baroclinicity. Using the Weather Research and Forecasting model, we have run several suites of experiments focused on ETC sensitivity to each environmental characteristic individually. Additionally, we performed the first examination of a bivariate parameter space, combining simultaneous perturbations to environmental temperature and baroclinicity. We find non-monotonic responses in strength due to the increasing effect of moist processes on ETCs with increasing temperature, and interplay between the perturbed environmental characteristics. Additional experiments with a latitudinally-varying, beta-plane Coriolis configuration demonstrate the sensitivity of ETC response to a seemingly small configuration modification.

Finally, we examine ETC sensitivity to the inclusion of radiative processes, largely neglected in idealized sensitivity literature.

These experiments reveal that extratropical cyclone development can be divided into three regimes: baroclinic, diabatically-limited, and diabatically-driven. As environmental temperature warms, ETCs stray from the canonical development mechanisms of the baroclinic regime and are increasingly impacted by diabatic heating and the formation of diabatic Rossby vortices. The inclusion of radiative processes consistently increases the strength of ETCs, primarily affecting development through interactions with atmospheric water vapor. While not a complete examination of all environmental variables, this suite of simulations demonstrates the need to consider ETC sensitivity to multiple variables simultaneously, as there are a breadth of scales at which ETCs are affected by changes to the Earth's climate system.

## Chapter 1: Introduction

### *1-1: Background Literature*

As defined in the American Meteorological Society's glossary, extratropical cyclones (ETCs) are "any cyclonic-scale storm that is not a tropical cyclone, usually referring only to the migratory frontal cyclones of middle and high latitudes." These synoptic-scale systems span thousands of kilometers (as seen in Figure 1-1) and play a pivotal role in midlatitude weather, responsible for at least half of the climatological precipitation in those regions, with the fraction exceeding 70-80% in storm tracks (Catto 2012; Hawcroft et al. 2012), as well as damaging wind events (eg. Browning 2004). Some projections predict an increase of 23% in damage and economic losses from ETCs in Western Europe by the year 2100 (Ranson et al. 2014). ETCs have many alternate names within the literature: midlatitude cyclones, baroclinic waves, even "cyclone waves" in early work by Eady (1949).

Regardless of the label, their defining dynamical characteristic is development through the baroclinic mechanism, which evolves from the natural disparity in solar heating between the tropics and the poles. Using the thermal wind relationship, this equator-to-pole temperature gradient results in vertical wind shear in both horizontal directions, formulated:  $\frac{\delta u_g}{\delta \ln(p)} = \frac{R}{f} \left(\frac{\delta T}{\delta y}\right)_p$  and  $\frac{\delta v_g}{\delta \ln(p)} = -\frac{R}{f} \left(\frac{\delta T}{\delta x}\right)_p$ , respectively.  $U_g$  and  $v_g$  represent the components of the geostrophic wind,  $p$  represents pressure,  $R$  is the gas constant of dry air,  $f$  is the Coriolis parameter, and  $T$  is the temperature.  $X$  and  $y$  symbolize the step size over which the temperature gradient is considered

in the longitudinal and latitudinal directions. Perturbations to the geostrophic wind (for example, due to orography) result in advection which displaces parcels into new thermodynamic environments and creates potential energy, which is converted into kinetic energy as the parcels continue to rise or sink (depending on their relative temperature). The final result is a baroclinic instability, an unstable flow commonly analyzed using the potential vorticity (PV) perspective, first introduced by Rossby (1936) but popularized by Hoskins et al. (1985). PV can be formulated in several ways, including the isobaric form used in this dissertation:

$$PV = -g \left[ -\frac{\delta v}{\delta p} \frac{\delta \theta}{\delta x} + \frac{\delta u}{\delta p} \frac{\delta \theta}{\delta y} + \eta \frac{\delta \theta}{\delta p} \right] \quad (\text{Eqn. 1.1})$$

where  $g$  represents gravitational acceleration,  $u$  and  $v$  are the horizontal components of the wind in the  $x$  and  $y$  directions,  $\theta$  represents the potential temperature of the environment,  $p$  is the pressure, and  $\eta$  is the absolute vorticity (which must also be calculated on isobaric surfaces). Regardless of formulation, PV is widely used because it considers the interplay of two atmospheric properties critical to midlatitude weather phenomena: vorticity and static stability. The key to the PV perspective is its conservation in adiabatic, frictionless flow – making it an ideal quantity for studies seeking to understand the contributions made to ETC development by diabatic processes, such as friction, latent heat release, and radiative heating/cooling.

Given their important role in the Earth's climate system as poleward transporters of momentum, energy, and moisture (Hartmann 1994), it is not surprising that understanding the influence of moist processes (such as convection) on ETCs has been an important line of work in understanding the development and dynamics of these powerful systems (eg. Davis et al. 1993; Dudhia 1993; Whitaker and Davis 1994; Chagnon 2013). The general consensus of this body of literature highlights latent heat release (LHR) as one of the most dynamically influential products

of moist processes. LHR refers to the release (absorption) of energy into (from) the surrounding environment as water undergoes a physical phase change. While all phase changes of water contribute to atmospheric LHR, the most common form is condensational heating, when water vapor condenses into cloud droplets. While this process occurs on a molecular level, the sum total of LHR is impressive, as latent heat flux makes up approximately half of the total poleward energy flux throughout the midlatitudes (Pierrehumbert, 2002; Trenberth and Stepaniak, 2003).

The impact of this energy flux is not without consequence to ETCs, as a number of dynamical implications result. Previous work has demonstrated more rapid ETC cyclogenesis in the presence of LHR (eg. Kuo et al. 1991). In addition, LHR has been found to strengthen the low-level circulation within ETCs, usually through development of low-level positive PV anomalies (Ahmadi-Givi et al. 2004). Estimates for the increase in strength range between 20% - 70% (Reed et al. 1988; Davis and Emanuel 1991; Davis 1992; Stoelinga 1996). LHR also has impacts at even finer scales, such as along frontal boundaries (Posselt and Martin 2004; Reeves and Lackmann 2004; Igel et al. 2013; Joos and Wernli, 2012; Igel and van den Heever 2014). Moist processes enhance ETC deepening rates by increasing vertical motion (eg. Gall 1976; Smith et al. 1984; Kuo and Reed 1988; Lapeyre and Held 2004). Significant amounts of diabatic heating have also been shown to modify the development processes and structure of ETCs (eg. Mak 1982; Čampa and Wernli 2012) and downstream development (Schemm et al. 2014). Inclusion of moisture can also lead to scale contraction, restricting the region of vertical motion within ETCs (Emanuel et al. 1987; Fantini 1993). Other previous work has focused on the impact of LHR within ETCs in particularly cyclogenetic regions, such as in the North Atlantic (Willison et al. 2013) or along East Coast of the United States (Marciano et al. 2015).

If we consider the distribution of moisture and precipitation within an ETC as a pathway to understanding where moist processes are most impactful, our focus turns to the warm conveyor belt (WCB). Beginning near the surface ahead of the cold frontal region, this stream of air ascends over the warm front before splitting west over the central low pressure minimum, and forming the “trough of warm air aloft” (trowal) to the east, as shown in Figure 1-2. The WCB is responsible for the transportation of warm, moist air into the ETC, maintaining environmental baroclinicity. More importantly, the WCB lifts this warm, moist air, and is responsible for approximately one third of the total upward flux in ETCs, with mass fluxes comparable to mesoscale convective systems (Eckhardt et al. 2004). The condensational LHR that results from lifting such moist parcels results in significant PV generation in the WCB (Grams et al. 2011), further adding to the impact of moist processes on the entire ETC.

With the impressive amount of literature written on the importance of moist processes at all scales of an ETC, and understanding their high-impact nature, the impacts of climate change will undoubtedly have some influence on ETCs in future climates. However, this influence on ETC frequency and intensity is complicated, as ETCs may exhibit varying responses depending on exactly how the climate system changes. Global temperature is expected to increase in the coming decades (IPCC 2014), with the largest warming taking place in the Arctic (Screen and Simmonds 2010; Overland and Wang 2010; Serreze and Barry 2011; Screen and Simmonds 2013). Changes in the equator to pole temperature gradient caused by differential patterns of warming have consequences for planetary baroclinicity, the primary driver of ETC development (Charney 1947; Eady 1949; Hoskins et al. 1985). Increases in temperature also affect the moisture capacity of the atmosphere due to the Clausius-Clapeyron relationship, which relates saturation vapor pressure and temperature as follows:  $\frac{\delta e_s}{\delta T} = \frac{L e_s}{R_v T^2}$ , where  $e_s$  symbolizes the

saturation vapor pressure of water,  $T$  symbolizes temperature,  $L$  is the latent heat of vaporization, and  $R_v$  is the gas constant of water vapor. Substituting in representative temperatures for near-surface conditions, one finds that the increase in saturation vapor pressure with temperature is approximately 6-7%/K of warming (eg. Held and Soden 2000; Trenberth et al. 2003). It should be no surprise then, that atmospheric moisture content is expected to increase in a warming atmosphere (Frei et al. 1998; Allen and Ingram 2002; Held and Soden 2006), which may lead to increased latent heating in extratropical cyclones (Watterson 2006). These two changes (weakening baroclinicity and increasing LHR) have competing effects on the possible strength of future ETCs, a signal that may depend on which metric is used to define ETC intensity.

With the uncertainty around ETC response to changing climate conditions, and given their societal impact, the natural question to ask is: How do extratropical cyclones respond to varying environmental conditions? While this question can be placed within the natural context of climate change, it also applies to understanding ETC development across basins, regardless of climate. As observed by Zillman and Price (1972), "...no two vortices are ever quite the same: it follows that no idealised cloud configuration or model structure can do justice to the individual diverse systems...". Indeed, the incredible diversity in ETCs results in multiscale interactions and environmental influences such as temperature, LHR, baroclinicity, sea surface temperatures, stability, etc. Understanding the isolated influence of each factor is difficult due to complex feedback relationships between these variables. Therefore, we must subdivide the question at-large by balancing consideration of factors that we can reliably control and consideration of factors that are climate-relevant. These requirements lead to focusing on the relationship of ETC development to environmental temperature, moisture, and baroclinicity.

In considering these specific variables, there are a few prime environments around the planet in which ETCs thrive. These regions are known as “storm tracks” and contain the highest incidence of ETCs through the North Atlantic, North Pacific, and Southern Oceans (Hoskins et al. 2002, 2005). It is within these regions that the combinations of environmental temperature, sea surface temperature, and existing environmental baroclinicity combine to provide ideal genesis and propagation conditions for ETCs. Indeed along many of these tracks, the maximum ETC activity coincides with wintertime peaks of maximum baroclinicity, and ETC activity minima coincide with summertime baroclinicity minima (Chang et al. 2002). As key regions for ETC genesis, work has naturally focused on the impact of a changing climate in storm track regions. Most notably, an analysis of the models within the Coupled Model Intercomparison Project (CMIP5) found a poleward shift of ETC storm tracks with a warming climate, indicating that the location of environments for ETC genesis and development may change over the coming decades (Simpson 2014). When attempting to project future changes for individual cyclones within these tracks, however, there has been considerable disagreement (Shaw et al. 2016), likely due to the inability of many global climate models to be run at grid scales that can represent small-scale physical processes, especially when used in a climate context.

Given the significance of extratropical cyclones in midlatitude weather, it is no surprise that much of the early curiosity about their structure and dynamics was borne from forecasting concerns. Early groups such as the Bergen School of Meteorology, from which was produced the early work of Bjerknes and the Norwegian cyclone model (Bjerknes 1919), strived to understand these phenomena better in order to predict their impact more accurately. This forecaster’s curiosity continues to drive meteorology, and is a major impetus behind the documentation of baroclinic life cycles. As previously mentioned, many of these studies have made it clear that

moist processes play an important role in the development and maintenance of ETCs. Indeed, it has been shown that there are significant differences in cyclone strength between dry and moist life cycle simulations, as measured through minimum sea level pressure and eddy kinetic energy (EKE), a measure of the mean energy of a vortex in turbulent flow (Boutle et al. 2010, 2011). This work was expanded upon by Booth et al. (2013; hereafter B2013), who increased the range of relative humidity and adjusted moisture content via modification of the saturation vapor pressure. Their results confirmed that increasing relative humidity from 0% to levels consistent with observations of real-world ETCs increases ETC strength. In addition, B2013 performed a series of runs with the same initial relative humidity, but artificially manipulated the effect of LHR by modifying the saturation vapor pressure with a multiplicative coefficient. These runs corroborated their previous conclusions about the importance of moisture in cyclogenesis and cyclone maintenance. Recently, Pfahl et al. (2015) performed experiments that merged these two areas by modifying optical thickness in order to simulate different climate regimes in a general circulation model (GCM). They found non-monotonic responses of both the minimum sea level pressure and eddy kinetic energy of ETCs to climates with increasing temperature/moisture. These results agree with the EKE results for B2013's experiments that utilized an increased saturation vapor pressure factor, but the two studies exhibit different responses of ETCs' minimum sea level pressure to warmer environments with more moisture.

### ***1-2: Dissertation Outline***

While providing a satisfactory answer to all aspects of a question such as “How do extratropical cyclones respond to varying environmental conditions?” is likely enough material for several dissertations, this work focuses on the effects of major environmental characteristics, potentially providing a partial answer to the entire question, while also aiming to stimulate

discussion about the as-yet unanswered portions. Chapter 2 outlines our means to answering this question – an idealized modeling configuration based on the work of B2013, with updates to both the model version as well as the initialization procedure. Previous methodologies are reviewed, with an emphasis on their applicability to the multivariate sensitivity problem that our science question proposes. It is found that many of the current methods, while useful for other applications, fail to provide the necessary representative resolution or flexibility to meet the requirements for our proposed sensitivity tests. Therefore, we devise a novel initialization procedure with precise control over the dynamic and thermodynamic aspects of the basic state used in our idealized configuration. Environmental characteristics for perturbation and output metrics for evaluation are selected before experiments are run. These experiments are separated into three main categories, each building towards a fuller understanding of ETC sensitivity in various environments.

Chapter 3 presents the most direct extension of B2013, and aims to explore the accuracy of the new initialization methodology in replicating similar results to the existing literature, before extending to experiments wherein multiple environmental factors are modified simultaneously. Most crucially, we construct a methodology in which the bulk temperature of the simulation can be adjusted without affecting other environmental characteristics, isolating the effect of moisture (and thus LHR) on ETCs in a more realistic manner than past work. We also adjust the environmental baroclinicity within the domain by adjustment of the jet profile. With the new initialization in place on an  $f$ -plane configuration, we obtain similar results to previous work by B2013 and Pfahl et al. (2015), finding non-monotonic responses of simulation-minimum sea level pressure and simulation-maximum eddy kinetic energy to increasing temperature and moisture. It is theorized that the non-monotonic response is due to size

constriction at warmer temperatures. We then extend the work to include a bivariate sensitivity experiment confirming the response behavior. Interplay between baroclinicity and bulk temperature is also noted, allowing for equivalencies to be made between the two environmental characteristics.

Having established the fidelity of our initialization method, Chapter 4 moves experiments towards a fully realistic configuration, repeating the experiments with non-constant Coriolis parameters more representative of the Earth's Coriolis force. Consistent with other idealized baroclinic wave studies (eg. Feldstein and Held 1989; Ullrich et al. 2015), we use a linear beta-plane approximation, although a full non-linear Coriolis plane is used to check that results are robust. While ETC strength again is non-monotonic, as in Chapter 3, the response is much different, as strength decreases with increasing temperature before increasing again at the warmest temperatures. Further investigation finds that strength declines due to the increasing influence of diabatic heating from convection, with the warmest end of the univariate experiments exhibiting diabatically-driven modes of ETC genesis and development. A comparison between the  $f$ -plane experiments in Chapter 3 and beta-plane experiments in Chapter 4 is made, wherein it is found that a qualitatively similar response of simulation-maximum EKE to temperature exists, with a transposition of the response to cooler temperatures in the beta-plane experiment. A three regime model for extratropical cyclogenesis is then proposed and described, spanning baroclinic, diabatically-limited, and diabatically-driven regimes. While these regimes have been sporadically discussed in existing literature, there has been little work done to systematically document the dynamical transitions between them until now.

In Chapter 5 we build upon the previous two chapters by enabling radiative processes within the model, reaching an idealized configuration close to the Earth's climate system. The

impact of radiative processes on ETCs has been a largely neglected topic of study in the literature, perhaps due to the complications it adds into the response of the system. Although the response of ETC strength is significantly more variable with radiative processes enabled, comparisons are made to the corresponding experiments without radiation in Chapter 4, with qualitatively similar results realized. Subsequent comparison of simulated upper-air soundings and PV anomaly analyses allows direct analysis of radiative effects on the dynamical environment. Finally, a suite of four separate sensitivity experiments are combined to create a larger experiment to radiative interaction. Using this suite of experiments, the contributions of radiative interactions with clouds, water vapor, atmospheric gases, and the surface can be compared, allowing specification of the primary radiative forcing mechanism. Finally, Chapter 6 summarizes and synthesizes the findings presented within the dissertation with a list of conclusions and offers suggestions for future work.

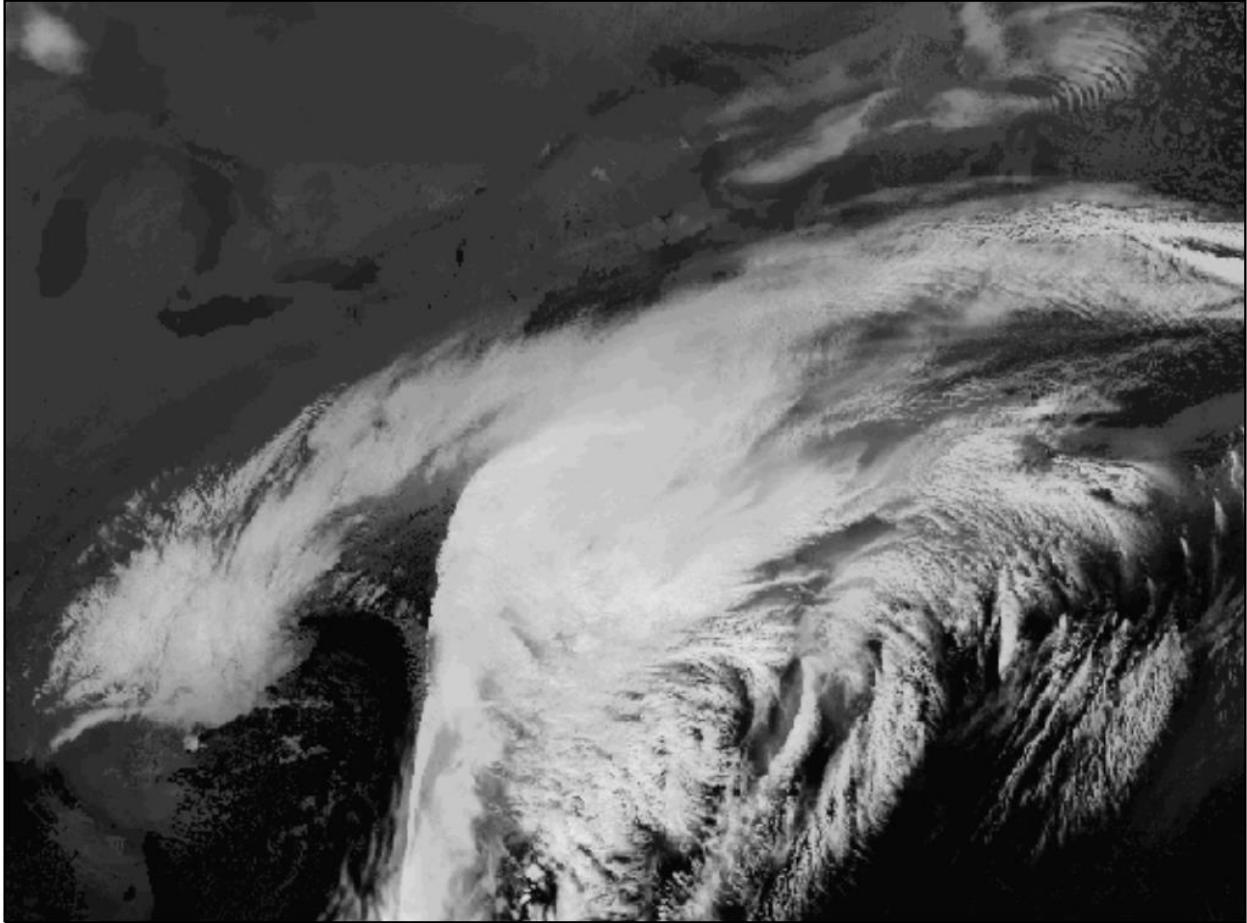


**Figure 1-1.** Outgoing longwave radiation product from a model-simulated extratropical cyclone off of the East Coast of the United States in November 2006. The classical “comma head” structure of the cloud field in ETCs is visible in white.

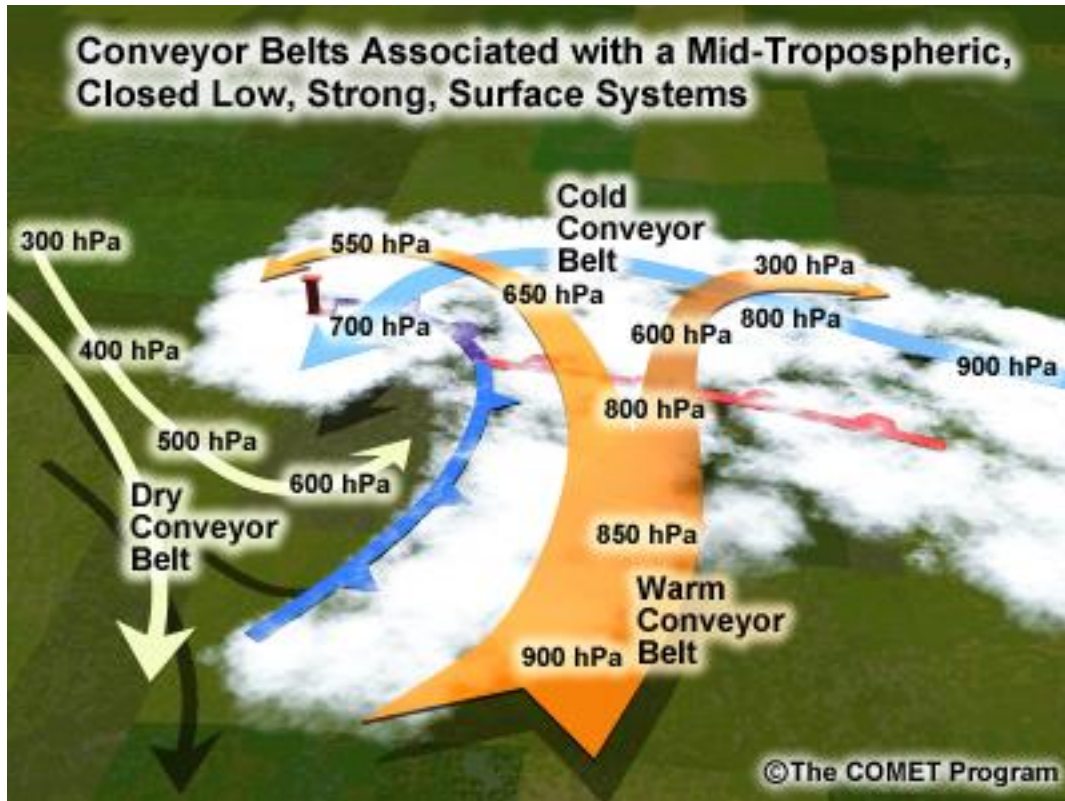


**Figure 1-2.** Schematic demonstrating the position of the Warm Conveyor Belt (in orange) within an extratropical cyclone. Adapted from the COMET module on mesoscale banded precipitation (courtesy UCAR MetEd program).

## **Chapter 2: Methodology**

### ***2-1: Methodology Survey***

Creating observational datasets for ETCs while maintaining comprehensive temporal and spatial coverage is extraordinarily difficult. The large spatial size of ETCs requires a grounded observational network of either a vast array of weather stations with upper air observations or remote observing platforms in Earth orbit. Unfortunately, the ground-based network is sparse, especially over the ocean, and while satellite observations are improving, there are still issues of revisit time versus resolution and coverage through the depth of the atmosphere. Moreover, neither of these methods allow for fine resolution observation capturing sub-cloud scale interactions, such as microphysical effects. In attempting a sensitivity test with such data, although trivial to note, observations are limited to the real world – all dynamical systems adhere to the laws of physics and include all physical processes. This means that systematic sensitivity studies are virtually impossible, given the number of variables within the atmosphere that must be held constant in order to determine multivariate sensitivity to a small number of variables.

Therefore, it is beneficial to utilize a modeling approach. Using numerical modeling techniques allows the construction of spatially and temporally consistent datasets capable of capturing processes across a range of scales. Moreover, numerical modeling is not beholden to incorporate all physical processes of the real world, allowing for greater control of atmospheric variables in constructing sensitivity tests. Numerical modeling can be described along a continuum from representative to idealized modes. In representative numerical modeling

simulations, the top priority is a faithful representation of a specific phenomenon, usually a single event (or case study), from which the understanding of dynamical aspects of the system is improved. Using this approach to understand the sensitivity in ETC development would likely be imperfect, as ETC morphology is diverse, exhibiting differences even between ocean basins, as noted by Chang and Song (2006). Therefore, it is difficult to perform general sensitivity experiments with a representative mindset, due to the demonstrated reliance on geography.

However, by abandoning location-specific simulations, idealized modeling can control for regional differences that arise from geographical, dynamical, and surface changes. Generally, idealized modeling methodology defines a representative base state for the unperturbed background flow of the environment. A perturbation is then placed into this environment which can take many forms such as atmospheric noise, fixed-amplitude temperature perturbation, or a seed vortex for a tropical cyclones – whatever necessary for the phenomenon of interest to develop when the model is run. This resulting control simulation can then be used as a base for subsequent sensitivity tests, which modify the basic state to tease out relationships between environmental characteristics and the phenomenon of interest.

The idealized approach to modeling baroclinic life cycles has a long history, beginning with the earliest linear mathematical models of Charney (1947), Eady (1949), and Kuo (1949). Realizing that linear solutions were not sufficient to describe the dynamics of the atmosphere (eg. Green 1970), early non-linear behavior was investigated by Simons (1972), Gall (1976), and Simmons and Hoskins (1978), among others. With the advent of increased computational power, improvements to these first dry dynamical studies were made in work by Davies et al. (1991), Thorncroft et al. (1993), and Rotunno et al. (1994), for example. The explicit addition of moisture into these idealized dry dynamical models expanded physical understanding, especially

as moist processes were found to be important contributors to ETC cyclogenesis and development (Emanuel et al. 1987). Early multi-level models (such as Balasubramanian and Yau 1994) were then expanded, giving way to a variety of idealized modeling initialization methods. Methods today define basic states by taking advantage of balance within the atmosphere: geostrophic, thermal wind, hydrostatic, or some combination thereof (for various examples, see Jablonowski and Williamson 2006; Olson and Colle 2007; Polvani and Esler 2007; Ullrich et al. 2015; Terpstra and Spengler 2015, etc.). While these methods vary, the goal is similar: define a balanced initial state that can be perturbed to initiate a baroclinic wave.

Configuration differences also extend beyond initialization procedure to even more basic model characteristics, such as model domains. Most recent modeling studies examining ETC-environment interaction have utilized general circulation models (GCMs). These methods have proven to be useful in examining the frequency of ETCs in future climate scenarios, the changing behaviors of these cyclones, and also examining the sensitivity of ETCs as a whole within such climates. However, when compared to limited-area domains, such as a channel bounded to the north and south and with infinite east-west dimension, GCMs are computationally limited by grid spacing and resolution, important to correctly resolving aspects such as ETC strength and precipitation distribution. For example, previous work has demonstrated ETC strength increases when grid spacing is reduced from approximately 100 km to 20 km, with little change in storm strength at grid spacing finer than 20 km (Jung et al. 2006; Champion et al. 2011; Li et al. 2011). Similar results have been obtained for idealized simulations of tropical cyclones (F. He, 2017; personal communication). The effects of coarse resolution on capturing diabatic features was also shown by Willison et al. (2013), who demonstrated the need to reduce grid spacing down to 20 km to capture these features accurately, even in limited-area or regional models. Incorrect

position and magnitude of diabatic processes in coarse resolution simulations can lead to unrealistic synoptic system evolution.

Finally, just as there is diversity in model configuration, there is also considerable diversity in the approaches taken to environmental modification when considering ETC sensitivity. These methods, used for both representative and idealized modeling studies, often focus on the effects of moist processes on ETCs within the context of a changing climate system. First, the most straightforward approach is a continuum test between dry and moist conditions created by modifying the environmental relative humidity. Previous work has modified relative humidity as a bulk quantity of the atmosphere (eg. Boutle et al. 2011; Booth et al. 2013; Schemm et al. 2003) and also restricted modification to specific latitude bands (Pavan et al. 1999). While this method is straightforward and useful for exploring the bulk effect of moist processes, it is not readily applicable to future climates, given that atmospheric moisture content is projected to increase while surface relative humidity values remain approximately constant in a warming climate (Held and Soden 2006; Schneider et al. 2010; Sherwood et al. 2010). Second, other work has attempted to understand the effect of moist processes on ETCs by adding a control on latent heat release through the addition of an adjustable parameter to the Clausius–Clapeyron equation (Frierson et al. 2006; Booth et al. 2013). While this method holds moisture content to realistic levels, it is not a physically possible scenario, and thus is not well-suited to exploring ETC sensitivity in future climates. Third, previous work with radiative processes enabled has developed a tunable parameter to adjust the optical depth of the atmosphere to longwave radiation (O’Gorman and Schneider 2008; Pfahl et al. 2015), resulting in a change in atmospheric temperature and moisture. However, this is not a feasible scheme for evaluating ETC sensitivity in the absence of radiative processes. Moreover, radiative water vapor feedbacks

and radiative effects of clouds also are not taken into account in this work. Finally, the most popular approach to evaluating ETC sensitivity in future climates is to modify the concentration of CO<sub>2</sub> or other atmospheric constituents. Common methods include benchmark tests doubling or quadrupling CO<sub>2</sub> concentrations (eg. Catto et al. 2011; Caballero and Hanley 2012) or following a prescribed IPCC emission scenario (eg. Bengtsson et al. 2009; Champion et al. 2011; Pepler et al. 2016). While appropriate for multi-model ensembles, these experiments are inherently dependent on scenario assumptions, and generalizing these conclusions would prove difficult. While these novel sensitivity approaches have their applications, they fall short of meeting our goal of generalizing ETC response among a range of future climates. Therefore, we create a new idealized framework under which we can precisely control the environment to fit our experimental goals.

## ***2-2: Model Configuration***

Our sensitivity experiments utilize Version 3.5.1 of the Weather Research and Forecasting model (WRF) (Skamarock et al. 2008) in an idealized mode that consists of a channel domain, with an east-west periodic boundary and north-south symmetric boundaries. The channel spans 181 x 361 x 50 grid points in the x, y, and z directions, respectively, with 25 km horizontal grid spacing. There are 49 midpoint model levels where prognostic variables are stored. This combination results in a channel width of 9000 km in latitudinal extent, spanning approximately 81 degrees of latitude. The channel is 4000 km in length before reaching the periodic boundary and has a height of 23 km. Unless noted as otherwise, the model is set up with a configuration identical to that used with WRF Version 3.0.1 by B2013 and Booth et al. (2015), including use of WRF's adaptive time stepping, and is run in a "full physics" idealized mode, with the YSU boundary layer scheme (Hong et al. 2006), Kain-Fritsch cumulus scheme (Kain and Fritsch

1993), and Monin-Obukhov similarity surface layer option for consistency and comparability with B2013. Rather than the Purdue-Lin scheme (Lin et al., 1983; Chen and Sun 2002), we use the Morrison two-moment microphysics scheme (Morrison et al. 2005, 2008), as two-moment schemes have been demonstrated to improve representation of microphysical processes (eg. Morrison et al. 2009; Dawson et al. 2010). No shallow cumulus scheme is used with the Kain-Friess cumulus scheme. Other parameterizations and configuration choices specific to each chapter will be noted within their respective chapters, with Chapter 3 using an f-plane Coriolis parameter anchored at 43°N, Chapter 4 using a beta-plane Coriolis parameter also anchored at 43°N, and Chapter 5 introducing the RRTM and Dudhia radiation schemes into the beta-plane experiments.

A liquid water surface underlies the entire domain with no topography, with sea surface temperatures initialized 0.5 K cooler than the temperature of the lowest atmospheric model level, and set constant in time during each simulation. The relative humidity at each level is determined as in B2013 (see Eq. 2.13 below), with a base relative humidity of 80% in the lowest atmospheric layer. With surface moisture and sensible heat fluxes enabled, the surface is allowed to interact with the overlying atmosphere; however, we note that this interaction is one-way as the ocean surface temperature is fixed.

### ***2-3: Model Initialization Procedure***

In initializing the domain, we follow the method used in B2013, based on the idealized baroclinic wave case described by Polvani and Esler (2007, hereafter PE2007). We begin by specifying the number of levels ( $N = 50$ ), a height for the top of the atmosphere ( $z_{\text{top}} = 23$  km), and the vertical distance for the first model level above the surface ( $dz_{\text{surf}} = 50$  m). We then

define the height of each level (by looping between  $k = 1$  to  $k = 50$ ) using the following equation for  $z$ , the position of the model interface levels:

$$z(k) = ak^2 + bk + c \text{ (Eqn. 2.1), where:}$$

$$a = \frac{z_{top} - (N-1) * dz_{surf}}{N^2 - 3N + 2}, b = dz_{surf} - 3 * a, \text{ and } c = 2a - dz_{surf}. \quad \text{(Eqns. 2.2 - 2.4)}$$

From here, a reference temperature profile,  $T_r$ , is calculated following the appendix of Polvani and Esler (2007), and formulated thusly:

$$T_r(k) = T_0 + \frac{\Gamma_0}{(z_t + z(k) - \alpha)^{1/\alpha}} \quad \text{(Eqn. 2.5)}$$

Within this formulation,  $T_0$  is the surface reference temperature, set to 300 K in the control run, but can be adjusted (as demonstrated in later experiments). From this surface temperature, temperatures decrease with height (indicated at each level by  $z(k)$ ) by a constant lapse rate  $\Gamma_0$  until height  $z_t$  (chosen to be 13km for these simulations). Above this height, the temperature is uniform.  $\Gamma_0$  is chosen to be 6.5 K/km, following the 1976 US Standard Atmospheric Temperature profile. The sharpness of the transition between these two temperature regimes is controlled by the parameter  $\alpha$ , which is chosen to equal 10 in these simulations, following PE2007 and B2013.

With a reference temperature profile complete, pressures at each level above the first level (which is set equal to 1000 hPa) are calculated as follows ( $k$  is looped between 2 and 50):

$$p(k) = p(k - 1) * e^{-\frac{g}{2R} \left( \frac{1}{T_r(k-1)} + \frac{1}{T_r(k)} \right) (z(k) - z(k-1))} \quad \text{(Eqn 2.6)}$$

Here,  $p$  is the pressure of each level,  $g$  is the gravitational acceleration (set equal to 9.81 m/s<sup>2</sup>), and  $R$  is the gas constant of dry air, 287 J kg<sup>-1</sup> K<sup>-1</sup>. Finally, the sigma coordinate for each interface level is calculated using the following:

$$\sigma(k) = \frac{p(k) - p(k=N)}{p_{surf} - p(k=N)} \quad (\text{Eqn. 2.7})$$

where  $p_{surf}$  is the surface pressure, and  $p(k=N)$  is the pressure at level N, the uppermost level. Having created an approximate reference state of the atmosphere to establish sigma levels, we find the midpoint sigma levels,  $znu(k) = \frac{1}{2}(\sigma(k+1) + \sigma(k))$ , and calculate the pressure at these midpoint levels (using  $pp$  to distinguish from the reference state) with  $pp(k) = znu(k)(p_{surf} - p_{top}) + p_{top}$ , where  $p_{top} = 50$  hPa and  $p_{surf} = 1000$  hPa, both consideration of dry pressure. Heights at these sigma levels (represented by  $zz$ ) are then calculated by  $zz(k) = -H \log\left(\frac{pp(k)}{p_{surf}}\right)$ , where  $H$  is the scale height of the atmosphere, set to 7500 m.

We then proceed to specify our wind profile within the domain. As the flow is initiated in a purely zonal orientation, we only need to worry about initiating the u-component of the wind, and consider changes only in the latitudinal direction,  $j$ , and height,  $k$ . Our wind profile takes the functional form:

$$u(j, k) = U_0 * F(j) * G(k) \quad (\text{Eqn. 2.8})$$

$U_0$ , the speed at the jet maximum, is set to 45 m/s.  $F(j)$  and  $G(k)$  are functions for the variation with latitudinal direction and height, respectively:

$$F(j) = \sin(\pi * \sin(lat(j)^2))^3 \quad \text{and} \quad G(k) = \frac{zz(k)}{z_t} * e^{-\frac{1}{2}\left(\frac{zz(k)}{z_t}\right)^2 + \frac{1}{2}} \quad (\text{Eqns. 2.9 - 2.10})$$

The latitude of the selected row of grid points is specified by  $lat(j)$ .  $F(j)$  is chosen following PE2007, which itself attempts to mimic Thorncroft et al. (1993).  $G(k)$  also follows PE2007, which follows a latitude dependence from Simmons and Hoskins (1977). Together these profiles produce a reasonable jet shape, with wind velocity at the surface initialized at 0 m/s.

Additionally, the latitudinal width of the jet is confined to the middle third of the domain and centered around 43° N, a reasonable position of the jet during the winter months. Meridional and vertical velocities are also set to 0 m/s.

Finally, we can complete the balanced temperature field at initialization. Again, following the appendix of PE2007, we can arrive at a temperature formulation as follows:

$$T(j, k) = T_r(k) - T_c(j, k) \quad (\text{Eqn. 2.11})$$

The formulation depends on a reference temperature profile, presented earlier, and utilizes a correction factor of  $T_c$  to iteratively bring temperature field into balance with the wind field:

$$T_c(j, k) = T_c(j - 1, k) + \left( \frac{du}{dz}(j, k) + \frac{du}{dz}(j - 1, k) \right) * \frac{1}{2} \Delta y * \frac{H}{R} * f, \text{ for } j > 1 \quad (\text{Eqn. 2.12})$$

At  $j=1$ , the southern boundary of the domain,  $T_c$  is set equal to 0 and the temperature is equal to the reference value.  $T_c$  includes the change in jet speed ( $\frac{du}{dz}$ ), meridional grid spacing used within the model ( $\Delta y$ ), and the Coriolis parameter  $f$ , which will be modified in future experiments in Chapters 3 and 4. For simplicity, latitudinally-varying Coriolis parameters are substituted directly into equation 2.12 for  $f$ , and are approximations. Afterwards, the potential temperatures ( $\theta$ ) at initialization are calculated:  $T(j, k) = T \left( \frac{p_{surf}}{p(j, k)} \right)^\kappa$ , where  $\kappa = 2/7$ , as in PE2007. Finally, a perturbation in temperature is added at the center of the domain, with a functional form of  $T_p(i, j, k) = \theta_{p0} * \cos^2 \left( \frac{r\pi}{2} \right)$ , where  $T_p$  represents the perturbation amount (with index  $i$  representing the zonal direction), the maximum of which is  $T_{p0}$ , which is set equal to 2 K, and the distance to the center of the perturbation given by  $r$ . We use a perturbation radius of 1000 km, so at  $r > 1000$ ,  $T_p$  is equal to 0. Cross-sections of these initial conditions are presented in Figure 2-1.

After the dry initialization is complete, moisture is then added; and as in B2013, the initial relative humidity profile is given by:

$$RH = RH_0 * \begin{cases} (1 - 0.85 * \frac{Z}{Z_t})^{1.25} & \text{for } Z < Z_t \\ 0.15 & \text{for } Z > Z_t \end{cases} \quad (\text{Eqn. 2.13})$$

For all experiments, the surface relative humidity ( $RH_0$ ), is set to 80%, and the moisture scale height ( $Z_t$ ) is set to 12 km. From these RH values, we calculate the vapor pressure, and eventually the mixing ratio at every point within the domain to initialize moisture. This two-step initialization leaves the initial conditions slightly unbalanced, but, following B2013, we do not make a final iterative correction. The atmosphere is then left to evolve naturally over a 14-day simulation. This initialization process results in Type-A cyclogenesis of ETCs, as initially defined by Petterssen and Smebye (1971). While these may comprise a small portion of real-atmospheric ETCs (Deveson et al. 2002; Plant et al. 2003), this initialization method allows freedom to adjust other environmental characteristics in a consistent manner, as described later in this section.

#### ***2-4: Experiment Design***

Our sensitivity experiments center on two key environmental characteristics relevant to ETC development: baroclinicity and bulk temperature. Note that the bulk temperature is correlated with column water vapor through the fixed initial relative humidity profile, and an increase in the (fixed) ocean surface temperature also implies a larger surface equilibrium vapor pressure via the Clausius-Clapeyron relationship. These controls on cyclone characteristics are distilled into easily modifiable scalar parameters within the model, enabling a straightforward gridded exploration of the cyclone perturbation - response relationship. Since the model begins in thermal wind balance, changes to the jet profile also result in modifications to baroclinicity.

To modify baroclinicity, we fix the southern boundary surface temperature at a value of 300 K, and a multiplicative factor of between 0.4 and 1.4 in steps of .2, is applied to the initial jet profile at all levels to adjust the baroclinicity of the domain, as demonstrated in Figure 2-2a for the *f*-plane simulations that will be presented in Chapter 3. Applying a single multiplicative, rather than additive, factor to the entire profile avoids introduction of surface friction associated with non-zero initial-time surface wind. At the location of the jet maximum, 13 km, the initial-time jet core maximum speeds associated with our distribution of multiplicative factors range from 18 m s<sup>-1</sup> to 63 m s<sup>-1</sup>, with a default of 45 m s<sup>-1</sup> (Fig. 2-2a). Maximum baroclinicity in the domain ranges from 0.55 K / 100 km to 1.9 K / 100 km, with a default of 1.49 K / 100 km in the meridional direction.

Bulk temperature is modified within the domain by adjusting the initial surface temperature at the southern boundary of the domain in steps of 4 K (i.e., the initial surface temperature ranges between 288 K – 308 K). This temperature change is applied equally across all levels, so with a warmer/cooler initialization temperature, the entire temperature profile shifts, and the initial dry static stability remains nearly constant (Fig. 2-2b, again for the *f*-plane simulations presented in Chapter 3). For conciseness, simulations with bulk temperature modifications will be referenced by the initial surface temperature at the southern boundary of the domain. Changing this reference temperature results in initial surface temperatures at the domain center (where the baroclinic wave will be generated) between 269.1-287.6 K, as demonstrated in Table 2-1. Furthermore, use of the same initial RH profile in each experiment means water vapor content increases with increasing temperature. Because of this, the bulk temperature test is also a proxy for a moisture sensitivity test. Modifying temperature in this manner constitutes a more realistic method of assessing actual atmospheric moisture changes in

future climates, compared to other moisture adjustment methods described previously in this chapter.

In order to isolate the effect of moisture and temperature, the bulk temperature experiments require an additional alteration at the time of model initialization. The two-step initialization methodology used by B2013 (Polvani and Wang, 2011) assumes a dry domain. Once water vapor is inserted (in the second step of initialization), each run exhibits a different initial dry static stability, obfuscating experimental results. To ensure a consistent initial dry static stability and baroclinicity profile in all bulk temperature experiments, a modification to the thermodynamic profile must be made to accommodate the effects of water vapor on atmospheric density. A one-time adjustment is made within the start-up procedure of WRF to carry over the potential temperatures obtained from the dry initialization, rather than recalculating the potential temperature in the initialization of the model. Once the run begins, no further adjustments are made, and WRF calculates potential temperature as usual. This modification to the initialization allows variations in temperature/moisture to be isolated for study. The dry static stability of the domain is nearly identical in all perturbed temperature runs, with a maximum lapse rate difference of  $0.5 \text{ K km}^{-1}$  between the extreme members of a set that spans a 20 K range in reference temperature.

The effect of perturbations in temperature and baroclinicity is compared across the set of simulations using a consistent set of output metrics that cover an array of meteorologically and societally relevant ETC properties. Strength is represented by the minimum sea level pressure (SLP), which is calculated as a 9-point box-average centered on the SLP minimum at each time. While minimum SLP does not singularly capture ETC strength, it provides meteorological context to strength, and allows for an approximate comparison with historical observed ETCs.

We also analyze storm intensity by calculating the average column-summed eddy kinetic energy (EKE) throughout the domain, the sums of which are evaluated as follows:

$$\sum_{k=0}^{N-1} \frac{p_k - p_{k+1}}{g} * \frac{1}{2} ((u'_k)^2 + (v'_k)^2) \quad (\text{Eqn. 2.14})$$

where N is the number of vertical levels in the model (k increases going up in the atmosphere), p is the pressure at each level, g is gravitational acceleration, and  $u'_k$  and  $v'_k$  are perturbations defined by subtracting the full wind field at each time from the averaged flow over the first 12 hours of the simulation. Finally, we use the precipitation output from WRF, which is automatically partitioned into large-scale, resolved precipitation and convective precipitation due to the use of a convective parameterization, which has been tested for robustness at multiple resolutions.

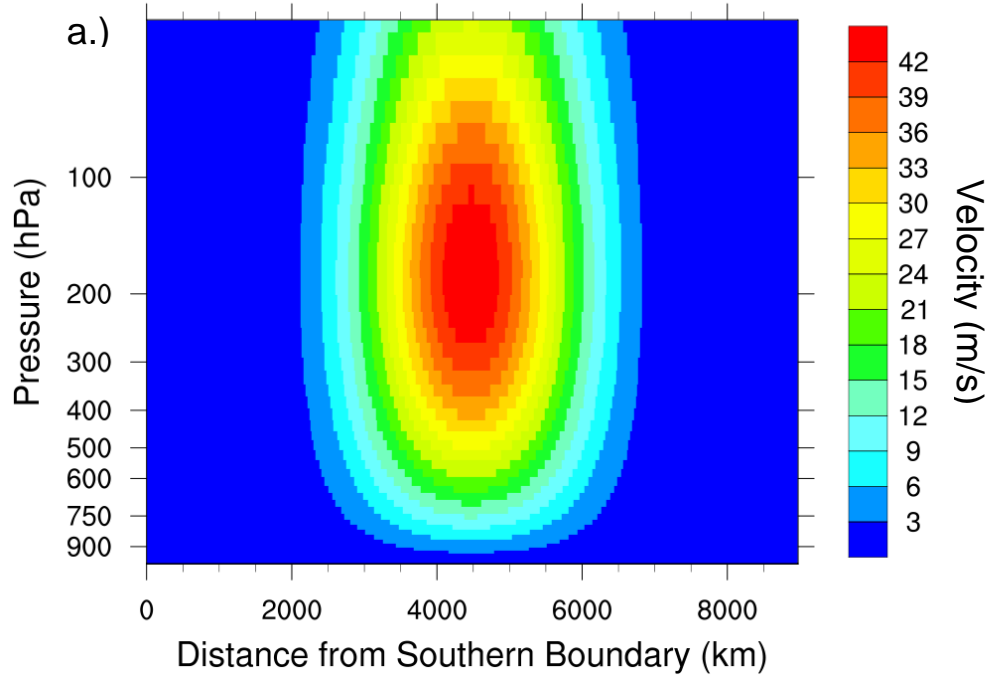
<i>Level #</i>	<i>Pressure (hPa)</i>	<i>Height (km)</i>		<i>Level #</i>	<i>Pressure (hPa)</i>	<i>Height (km)</i>
1	1000.00	0.00		26	450.58	6.49
2	994.32	0.05		27	422.25	6.98
3	986.69	0.12		28	394.43	7.48
4	977.15	0.20		29	367.24	8.01
5	965.75	0.30		30	340.75	8.54
6	952.54	0.42		31	315.06	9.10
7	937.59	0.56		32	290.24	9.68
8	920.97	0.72		33	266.37	10.27
9	902.75	0.89		34	243.51	10.88
10	883.02	1.08		35	221.75	11.50
11	861.88	1.29		36	201.13	12.15
12	839.41	1.51		37	181.73	12.81
13	815.74	1.75		38	163.60	13.49
14	790.96	2.01		39	146.75	14.18
15	765.19	2.29		40	131.20	14.90
16	738.54	2.58		41	116.93	15.63
17	711.14	2.90		42	103.89	16.38
18	683.11	3.23		43	92.03	17.15
19	654.56	3.57		44	81.29	17.93
20	625.62	3.94		45	71.60	18.73
21	596.42	4.32		46	62.88	19.55
22	567.07	4.72		47	55.08	20.39
23	537.70	5.14		48	48.10	21.24
24	508.42	5.57		49	41.89	22.11
25	479.34	6.02		50	36.39	23.00

**Table 2-1.** Vertical levels used in the simulations.

Reference Temperature	288 K	292 K	296 K	300 K	304 K	308 K
Initial Surface Temperature, Southern Boundary	269.1 K	272.8 K	276.5 K	280.2 K	283.9 K	287.6 K

**Table 2-2.** Conversion table between reference temperatures (southern boundary surface initialization temperatures) and initial surface temperature at the center of the domain.

Initial Jet Profile, 300 K Run, Jet Amp. Factor = 1.0



Initial Temperature, 300 K Run, Jet Amp. Factor = 1.0

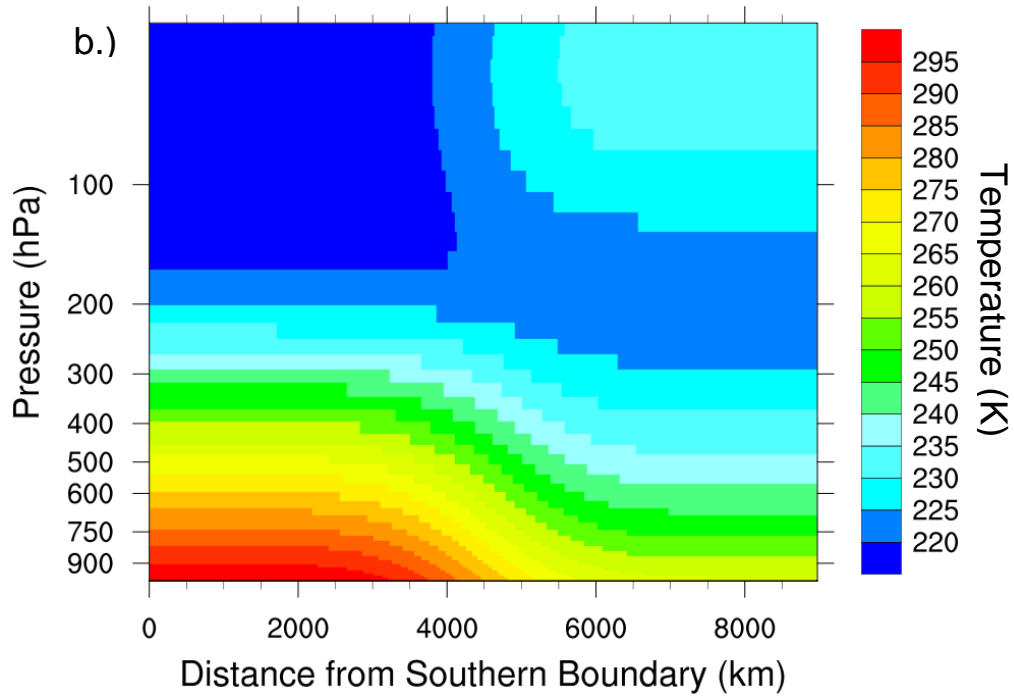


**Figure 2-1.** Initialization cross-sections of the jet profile (Figure 2-1a) and temperature (Figure 2-1b) for the control run, with a southern boundary surface initialization temperature of 300 K and a jet amplitude factor of 1.0, on an  $f$ -plane.

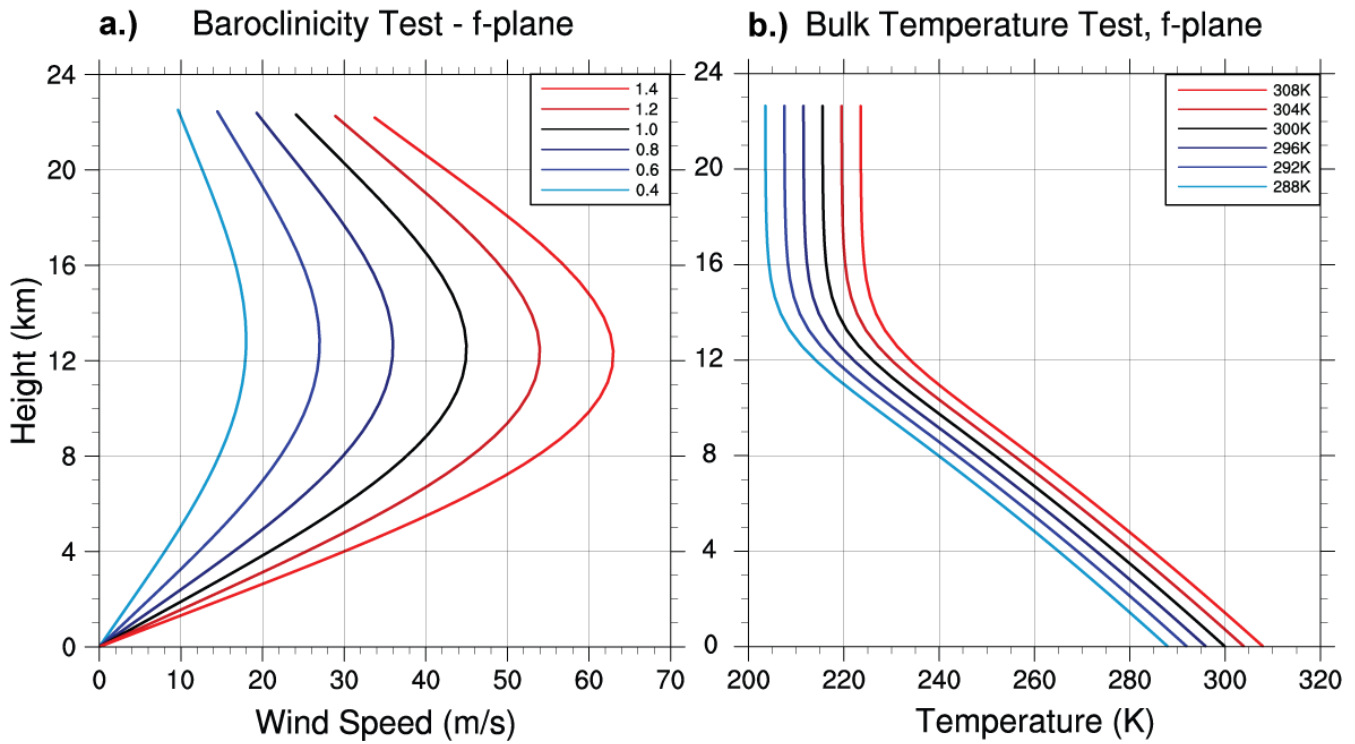


**Figure 2-2.** Environmental initialization for the perturbed parameter in the univariate baroclinicity test (Figure 2-1a, left), where the amplitude of the jet profile is modified; and for the univariate bulk temperature sensitivity test (Figure 2-1b, right), where temperature is changed within the domain.

## **Chapter 3: Evaluation and Extension of ETC Sensitivity Experiments on an $f$ -plane**

### ***3-1: Introduction***

While more recent work has been able to quantify upscale growth of predictive errors due to moist processes (Tan et al. 2004), comparison of dry and moist models of high-impact case studies has a long history. Chang et al. (1982), for example, compared dry and moist simulations with a grid spacing of approximately 140 km (by today's standards, a very coarse spacing, but referred to as a "fine-mesh" at the time) to survey the impact of moist processes on a developing ETC that brought heavy rains to the Great Plains. They found that the model could not reproduce the system without the inclusion of moist processes. Fantini (1995) noted that "...the introduction of moist processes even in a simple model like the present one generates a number of uncommon features that deserve further study."

Perhaps the most relevant portions of that body of work to this dissertation are sensitivity tests exploring the space between simple dry-wet binary tests. Some of the earliest work in this context was done by Pavan et al. (1999), who used the UK Met Office global climate model to perform variations of dry-moist experiments, with bands of relatively dry and moist regions, along with fully dry, semi-moist, and fully moist runs. They found varied signal across the moisture continuum, depending on the relative humidity configuration used within the model, positing that perhaps moist storm tracks are as energetic as dry ones. However, they also note that their exploration of moist sensitivity largely reveals uncertainty about its role.

In attempting to diagnose moisture transport within ETCs, Boutle et al. (2011) expanded on previous binary dry-moist experiments in Boutle et al. (2010) using the UK Met Office Unified Model (MetUM) at a resolution of  $0.4^\circ$  (approximately 44 km). Running 14-day simulations in an idealized channel model, they adjusted the maximum surface value of relative humidity ( $RH_0$ ) between 40% and 90%. While differences in evolution between the ETCs in the experiment did not appear until cyclogenesis began 4 days into the simulation, ETCs in environments with increasingly larger  $RH_0$  values tended to have slight increases in eddy kinetic energy, indicating a stronger, more energetic cyclone. In addition, they performed a sensitivity test of their idealized configuration to surface temperature, fixing relative humidity but adjusting the surface temperature of the entire domain, with resulting surface temperatures of between 270 and 285 K at the center of the jet ( $45^\circ$  N). While development time remained relatively unaffected, increasing temperature resulted in increasing values of EKE, indicating the presence of more intense cyclones. Finally, they tested sensitivity of the system to the meridional temperature gradient by adjusting the peak jet speed between 35-50 m/s, finding that faster jet speeds (and thus greater meridional temperature gradients) result in stronger cyclones.

This work was then followed on by Booth et al. (2013) who aimed to reproduce and extend the results of Boutle et al. (2011) with the explicit intention of examining the dynamical impacts of moisture on ETCs, rather than moisture transport. Booth et al. (2013) also utilized the WRF model rather than the MetUM model, running the majority of their experiments at a 50 km grid spacing. They analyze more metrics than previous studies, considering changes in minimum sea level pressure, eddy kinetic energy, precipitation at the 99<sup>th</sup> percentile and wind speeds at the 99<sup>th</sup> percentile, adding an extreme weather context to their sensitivity experiments. In their first set of experiments, maximum relative humidity within the domain was stepped between 0 –

95%. While similar to Boutle in finding an increase in EKE with humidity, there were also differences in the magnitude of variation, and an EKE decrease within the most humid environments. Focusing in on moist processes, Booth et al. also performed a second set of experiments adjusting the saturation vapor pressure coefficient between 0 to 2 – from simulations with no impact from LHR, to simulations where this effect was doubled. In this non-physical analog to the relative humidity experiments, similar results were obtained.

In this chapter, we aim to extend the results of Booth et al. (2013), by building upon their modeling configuration with a more realistic adjustment to moisture content. We combine this extension with a consideration of the other perturbations performed in Boutle et al. (2011). A description of the specifics of our modeling configuration and experimental outline are presented in Section 3-2, with the results of the univariate and bivariate experiments presented in Sections 3-3 and 3-4, respectively. Section 3-5 contains a discussion of dynamical features of interest within our experiments, before concluding and summarizing the work in Section 3-6.

### ***3-2: Methods and Experiment Design***

Following on the work of Booth et al. (2013, hereafter B2013), we use the methodology and model configuration described in Chapter 2, with the modifications of Wang and Polvani (2011) placing the jet on an  $f$ -plane with Cartesian geometry. This configuration results in a constant Coriolis parameter of  $1 \times 10^{-4} \text{ s}^{-1}$  regardless of latitude, equivalent to the Coriolis force at  $43^\circ\text{N}$  latitude. While not representative of the Earth's Coriolis force, which varies with latitude, utilization of the  $f$ -plane has two key advantages as a starting point for our sensitivity tests. First, it provides a base for future evaluation by simplifying the model configuration. After understanding ETC response sensitivity on an  $f$ -plane, the additional complication of a non-

constant Coriolis parameter can be added (as will be seen in Chapter 4) to understand the contribution of individual physical processes to ETC sensitivity. Use of an  $f$ -plane also allows evaluation of our novel mechanism for environmental adjustment of temperature, moisture, and baroclinicity against previous work by Boutle et al. (2011) and B2013. For now, we also omit the use of a radiative scheme, as in B2013, for ease of comparison with previous work. All other parameterization packages and configuration choices are as listed in Chapter 2.

In designing our sensitivity tests, we overlap with previous work while incorporating more realistic explorations of future climates. We construct 3 experiments on our  $f$ -plane configuration, outlined in Table 3-1, beginning with two 6-simulation univariate tests of ETC sensitivity to bulk temperature and baroclinicity, in line with the existing literature. The final experiment is a 121-simulation bivariate experiment which utilizes simultaneous changes to both bulk temperature and baroclinicity, an approach new to the literature. The result is a comprehensive examination of a parameter space relevant to present and future climate conditions among a range of environments across the planet.

### ***3-3: Univariate Sensitivity Results***

#### ***3-3.1 Dry Simulations***

Before conducting a sensitivity analysis using the full set of moist processes within the model, a baseline test of the ETC initialization is conducted by running both Experiment 1 and Experiment 2 in a dry setting. All moist processes are disabled, and as such, water vapor in the domain acts as a passive tracer. The results are presented in Figure 3-1, which displays the minimum SLP and column-summed EKE of each simulated ETC throughout its lifetime

(averaged across the entire domain). Figure 3-1a presents the results from the baroclinicity test, while Figure 3-1b presents results from the bulk temperature test.

Figure 3-1a demonstrates the known effect that changing the baroclinicity of the dry domain has on the developing ETC. As first demonstrated theoretically by Eady (1949), increases in the meridional temperature gradient result in greater wave amplitudes (i.e. stronger ETCs) with more rapid development, even in the absence of moisture. Those that do mature (jet amplification factors of 0.8 to 1.4) exhibit a range of approximately 30 hPa between their SLP minima, with strength increasing in more baroclinic environments. Similar responses in strength are demonstrated in the EKE metric. In addition, ETCs in higher-baroclinicity environments exhibit shorter times to genesis and more rapid development, while ETCs within the weakest-baroclinicity environments (jet amplification factors of 0.4 and 0.6) fail to fully mature by the conclusion of the simulation. These results are summarized in Table 3-2, which displays times to simulation-minimum SLP and simulation-maximum EKE for the dry versions of Experiments 1 and 2. This result confirms that perturbations to environmental baroclinicity result in expected response functions. Figure 3-1b presents the EKE and minimum SLP results for the dry variation of Experiment 2. Here, an almost negligible response in both metrics is observed, in contrast with the results from perturbing environmental baroclinicity. Table 3-2 demonstrates that the times of the EKE maxima and SLP minima are nearly equivalent among runs conducted with the dry variant of Experiment 2. As our initialization method holds dry static stability nearly constant between runs, minimal sensitivity in the absence of moist processes is expected, and verifies that our method for adjusting temperature has minimal effect on the dry dynamical mode of an ETC.

### 3-3.2 *Moist Simulations*

Next, we enable the moist portion of the initialization and repeat Experiments 1 and 2, the univariate baroclinicity and bulk temperature experiments. The minimum SLP and maximum EKE results of these simulations can be found in both Table 3-3 and Figure 3-2. Table 3-3 presents the times to maximum strength (measured by both maximum EKE and minimum SLP) for all ETCs in both experiments. Figure 3-2a displays the minimum SLP and maximum EKE results from the baroclinicity univariate test and Figure 3-2b from the bulk temperature univariate test.

Comparison of Table 3-2 (dry univariate results) and Table 3-3 demonstrates that moist ETCs develop faster than their counterparts in the dry environments, with peak intensity reached 12-21 hours sooner in moist environments than in dry environments, regardless of metric. The exception to this is the ETC in the coldest environment, with a southern boundary initialization temperature of 288 K, for which the dry and moist variations exhibit the same time to peak strength. While the presence of water vapor has a noticeable impact on simulation-maximum EKE, ETC growth rate is unaffected.

Baroclinicity perturbations in a moist environment (Fig. 3-2a) exhibit a qualitatively similar response as their dry counterparts. ETCs in environments with minimal baroclinicity fail to fully develop, and increasing baroclinicity leads to more rapid development, lower minimum SLP values, and greater values of maximum EKE. However, the inclusion of moist processes leads to amplification of differences in strength, increasing dramatically in environments with stronger baroclinicity. For example, at a scale factor of 1.4, the addition of moist processes leads to a doubling of maximum EKE and an approximate deepening of 12 hPa in minimum SLP. The results demonstrate not only the robustness of the response of strength metrics to increases in

baroclinicity, but also the amplification to this response that the addition of moist processes provides.

When moist processes are added to the bulk temperature sensitivity test (Fig. 3-2b), minimum SLP decreases monotonically with temperature, except in the warmest/moistest case. This indicates a limitation on storm strength at the upper end of our chosen parameter range, the causes of which will be discussed further in Section 3-5. Table 3-3 quantifies the developmental differences visible in Figure 3-2b between two seemingly separate regimes of runs. The cooler simulations (288 K-296 K) exhibit a slower, 10-12 day timeline to peak strength, while warmer simulations at 304 K and 308 K reach peak strength just after 9 days. Moreover, the timing between peaks in strength in minimum SLP and EKE also changes with temperature. Simulations in cooler environments demonstrate a 12-24 hour period between these two maxima, while simulations at the warmer end exhibit both maxima nearly simultaneously. Changes to the inter-maxima period are not consistently linear or monotonic with increasing temperature/water vapor; this is likely partially due to the noisiness that minimum SLP fields can exhibit at coarser spatial resolutions. Figure 3-2b also demonstrates that the maximum value of the EKE during an ETC's lifetime exhibits a non-monotonic behavior with respect to changes in temperature, suggesting limiting behavior as seen in B2013 and Pfahl et al. (2015). Peak values of simulation-maximum EKE occur in ETCs with an initialization temperature of between 296 K-300 K, with decreasing maxima when temperature and moisture content are raised further, even while warmer ETCs experience more rapid development. Unlike the baroclinicity sensitivity test, increases in temperature and moisture content work against enabling deeper and more powerful ETCs, indicating that the diabatic effects brought about by the addition of moist processes are not always beneficial to the amplified development of the ETC.

Figure 3-3 presents cyclone-centered maps of the spatial distribution of EKE at the time of maximum EKE, for cyclones with southern boundary initialization temperatures of 292 K, 300 K, and 308 K. When considering the maximum point value of EKE in the domain, we observe an increase with increasing temperature and moisture content, representing the increased strength of these cyclones shown previously through minimum SLP and maximum ETC metrics. Conversely, Figure 3-3 also demonstrates that ETC size at maturity decreases with increasing temperature, especially at the warmest end of the parameter range. This reduction in size limits EKE growth in ETCs with increasing temperature, reflecting the scale contraction described by Emanuel et al. (1987), and is similar to B2013 and others who have adjusted relative humidity or LHR parameters to achieve this result, rather than leveraging the increased moisture capacity of a warmer atmosphere. Reduction in the size of the ETC leads to the non-monotonic behavior of maximum EKE displayed in Figure 3-2b, and suggests there may be a range of intermediate temperatures for which the cyclone EKE is maximized. Mechanisms for ETC size contraction will be explored in Section 3-5.

#### ***3-4: Bivariate Sensitivity Results***

After completion of both univariate tests, we conduct a bivariate test, simultaneously varying both bulk temperature and baroclinicity. The bivariate experiment is made up of 121 model runs spanning southern boundary initialization temperatures of 288 K-308 K in steps of 2 K and jet amplitude factors of 0.8 to 1.2 in steps of 0.04. We maintain the same range of bulk temperatures in order to consider a diverse array of cyclogenetic environments (e.g., formation of storms at various latitudes and at various times of year) in both current and future climates. In contrast, we restrict the range of jet amplitudes to enhance coverage within the climate-relevant

portion of our parameter space. All other model parameters and settings in the bivariate runs are identical to those used in the moist univariate tests. This experiment allows more realistic exploration of future climate scenarios by acknowledging that climate changes along more than one parameter. Such a test also allows identification of possible feedbacks within the system.

Figures 3-4 – 3-6 depict the results of the bivariate tests for the entire parameter space, with bulk temperature varying on the vertical axis and the jet amplitude factor (and thus baroclinicity) varying on the horizontal axis. Each run is represented by a single box covering the portion of the parameter space to which it is nearest. Figure 3-4 displays the minimum SLP for each ETC, which exhibits more complexity than the univariate response. Response of minimum SLP to temperature and moisture content is relatively linear until a threshold of 304 K, after which a limiting behavior (also demonstrated in the univariate experiment) exists. In addition, it is also important to note that the degree of non-monotonicity is influenced by environmental baroclinicity, as ETCs in higher baroclinicity environments demonstrate a more rapid decrease in maximum EKE values in the warmest and most moist environments.

This bivariate experiment also allows for comparisons among pairs of perturbed parameters. For example, using the baseline baroclinicity (jet amplitude factor of 1.0), and a starting southern boundary initialization temperature of 300 K, a 4 K increase in bulk temperature (from 300 K to 304 K) has approximately the same effect on the minimum SLP of an ETC as an 8% increase in baroclinicity. A 4 K decrease in temperature (from 300 K to 296 K) is equivalent to a 12% decrease in baroclinicity. In much of the parameter space, for which southern boundary initialization temperatures are below 300 K, the relationship between baroclinicity and minimum SLP is approximately linear, as a 4% increase in baroclinicity has the same effect as a 4 K increase in temperature. Above 300 K, this same increase in temperature

corresponds to a larger change in baroclinicity, consistent with differences in developmental timelines and ETC size. The changes near a bulk temperature of 300 K indicate the presence of a new response regime at higher temperatures, in which diabatic heating plays an increased role.

Figure 3-5 presents the maximum value of each ETC's domain-average column-summed EKE in the bivariate sensitivity experiment. As in the univariate results, there is a non-monotonic response of maximum EKE to increasing temperature, and the general functional response of maximum EKE to temperature perturbations is not dependent on baroclinicity. As in the minimum SLP plot (Fig. 3-4), separate ETC regimes are evident, as the maximum EKE response differs on either side of the peak values at approximately 298 K. At temperatures below this threshold, response of maximum EKE to increasing temperatures at all baroclinicity values is consistently linear. However, beyond the 298 K threshold, the decrease is rapid, especially in the most baroclinic environments, where overall diabatic heating would increase the most. This thresholding behavior indicates that diabatic heating may be playing a role in the disruption of ETC strengthening.

Finally, we revisit the conclusion of the univariate experiments, which demonstrated a decrease in ETC size as the primary limitation on maximum EKE with increasing temperature. For robustness, we compute ETC size at both the time of maximum EKE (Fig. 3-6a) and minimum SLP (Fig. 3-6b), as defined by computing the area enclosed by a SLP contour 30 hPa greater than the minimum SLP (20 hPa and 40 hPa thresholds were also tested and yield qualitatively similar results). As in the univariate bulk temperature experiment (Fig. 3-3), ETC size generally decreases with increasing temperature at all baroclinicity values, as well as decreasing with increasing baroclinicity. These decreases begin to occur at the peak strength in both metrics, indicating that the size difference between these ETCs are robust and not subject to

time-sampling bias. While the response is qualitatively similar along both axes, the magnitude of response variation depends on the portion of the parameter space, with greater decreases in ETC size at cooler temperatures and weak baroclinicity values. These rapid changes over small perturbations reflect the acceleration of the ETC development timeline. Conversely, ETC size begins to converge towards a restricted range at warmer temperatures and higher baroclinicities, indicating some constraint on minimum size. Whether this constraint is due to dynamics or model configuration requires further investigation.

### ***3-5: The Role of Diabatic Heating***

Examination of the three experiments performed within this study reveals two key responses of ETCs to environmental variation: (1) an increase in speed of cyclone development when moist processes are active, and (2) a decrease in storm size with increasing temperature and baroclinicity in a moist environment. Considering that both of these responses only exist with moisture present, we conduct an analysis exploring the mechanisms by which moist processes may act to modify ETC size and accelerate development. In this section, we will first analyze the spatial distribution of diabatic heating, especially in the vicinity of the cyclone center – first in the latitudinal and longitudinal directions (Figures 3-7a & 3-7b), followed by an analysis of the vertical distribution in Figures 3-8a through 3-8d. Finally, dynamical effects of the diabatic heating are evaluated through analysis of PV anomalies, in Figure 3-9.

Figure 3-7a presents a map displaying the frontal surfaces of 3 ETCs selected from the univariate bulk temperature test (those with initialization temperatures of 292, 300, and 308 K) 24 hours after a precipitation rate of  $1 \text{ mm hr}^{-1}$  is recorded anywhere within the domain. Following Posselt and Martin (2004), this map is constructed by tracing the contour of a single

equivalent potential temperature ( $\theta_E$ ) value along pressure levels every 100 hPa between 500 hPa – 1000 hPa. Progressively darker colors on the figure indicate the  $\theta_E$  level at progressively higher pressures. The specific value of  $\theta_E$  mapped is chosen to be most representative of the warm side of the frontal surface and is adjusted consistently with increases in bulk temperature. Overlaid in cross-hatching are areas in which the precipitation rate exceeds  $1 \text{ mm hr}^{-1}$ , with red hatching indicating precipitation generated by the convective parameterization scheme and blue hatching indicating precipitation generated by the microphysical scheme. It is important to note that while these results can be sensitive to model grid spacing and choice of convective parameterization, these results were tested at both coarser (50 km) grid spacing, and with an alternate convective parameterization (Grell and Dévényi 2002), with robust results. As temperatures warm, non-convective precipitation shifts from being the dominant precipitation mode to equality with its convective counterpart in the warmest/moistest runs. The shift in temperature occurs alongside a decrease in moist static stability in the warmest runs, increasing convective activity and redistributing the associated LHR throughout the depth of the atmosphere, rather than simply at low levels (Fig. 3-8). As a result of the increased convection and differing vertical distribution of LHR, structural differences begin early during development, a result indicated by greater frontal surface deformation with increasing temperature.

Figure 3-7b presents a similar frontal analysis for 3 ETCs from the univariate baroclinicity test, with jet amplitude factors of 0.6, 1.0, and 1.4. As in Figure 3-7a, frontal maps are displayed 24 hours after the first incidence of precipitation rates greater than  $1 \text{ mm hr}^{-1}$ . Unlike Figure 3-7a, the  $\theta_E$  value used to define the frontal surface is constant between simulations in the univariate baroclinicity experiment. Again, the dominant precipitation regime shifts with increasing baroclinicity; however, the area of convective precipitation remains

relatively constant, while the area of non-convective precipitation expands, suggesting an increase of resolved-scale LHR within the ETC. LHR-induced deformation of the frontal surfaces is documented, as ETCs within the least baroclinic environments exhibit the highest convective fractions of precipitation and the greatest deformation. When considering Figures 3-7a and 3-7b together, the differences in the spatial extent of precipitation indicate differing distributions of LHR, as the increases in LHR are spread over a much larger spatial area in the univariate baroclinicity test, rather than being redistributed vertically throughout the atmosphere, as shall be demonstrated next in Figure 3-8.

Differences in the distribution of LHR are also visible in vertical profiles sampled during ETC development. Using the LHR products produced in WRF, profiles are calculated by averaging over a 1000 km by 1000 km box centered on the SLP minimum 2-3 days prior to the time of maximum EKE. Results are displayed for both the univariate baroclinicity experiment (Figs. 3-8a and 3-8b), and the univariate bulk temperature sensitivity experiment (Figs. 3-8c and 3-8d). In addition, the LHR is partitioned between two sources: the microphysics scheme (Figs. 3-8a and 3-8c), and the convective parameterization scheme (Figs 3-8b and 3-8d).

Consideration of these profiles, in conjunction with the frontal surface maps, yields a three-dimensional view of the influence of LHR early in the life of these ETCs. In the univariate bulk temperature test, LHR distribution changes follow the expected increase in convection within the ETC. Primarily, convection redistributes diabatic heating vertically, rather than increasing its latitudinal and longitudinal extent – a clear conclusion from analysis of Figures 3-8a and 3-8b, and antithetical to the response to increases in baroclinicity (Figs. 3-8c and 3-8d). Increases in temperature and moisture content demonstrate primarily little response through the coolest 4 runs of the bulk temperature baroclinicity test. However, a significant change in

response behavior at the 304K threshold again matches with previous thresholds that indicate a shift towards diabatically-limited and diabatically-driven ETCs. Regime shift is also signaled by a discontinuity in the shape of the LHR profile. While cooler cyclones generally exhibit LHR below approximately 500 hPa, the convectively-forced diabatic regime exhibits LHR maxima at levels above 500 hPa, producing little to no positive LHR through the low levels of the atmosphere. Moreover, sensitivity to increasing temperature in the diabatically-driven regime of ETCs is greater than in the cooler, baroclinic regime - the maximum LHR is more sensitive in the 4 K step between the two warmest runs than in the 12 K of steps between the four coldest runs.

In the univariate baroclinicity test (Figure 3-8c for microphysical LHR, and 3-8d for cumulus scheme LHR), the primary pattern is a growth of LHR throughout the middle and lower levels of the atmosphere with increasing environmental baroclinicity, reflective of the increasing strength in the simulation-maximum EKE and simulation-minimum SLP metrics, as well as the increasing horizontal extent of precipitation and diabatic processes. Moreover, the growth is consistent between runs, demonstrating a lack of regime change within the parameter space. Of note is the additional LHR from the cumulus scheme in the most baroclinic environment, aiding further development and contributing to the scale contraction seen in storm size results. Profiles with enhanced LHR from the cumulus scheme also exist for the ETC in the weakest baroclinic environment; however, this is a byproduct of the failure of the ETC to mature during the run, and reflective of the disorganized convection that is able to develop in its place. In this experiment, the additional baroclinic energy available contributes to a horizontal expansion of the diabatic heating fields and leads to minimal size reduction of ETCs in more baroclinic environments,

unlike increases in temperature, which result in thresholding behavior that indicates separate regimes of ETC cyclogenesis and development.

Finally, the influence of increasing diabatic development within the univariate bulk temperature test is reflected in the potential vorticity (PV) anomalies associated with the ETCs in the sensitivity experiment. As discussed in Hoskins et al. (1985), the adiabatic conservation of PV facilitates the isolation of diabatic influence on development during the cyclogenesis process, providing a window into the transition between baroclinic and diabatic modes of initial cyclogenesis. Figure 3-9 presents an analysis of PV anomalies midway through development (as measured by EKE strength) for two ETCs from the bulk temperature sensitivity test: the baroclinically-driven 292 K case (top row), and the diabatically-driven 308 K case (bottom row). Times are chosen to represent analogous stages within the life cycle between the two runs, given the offset in development timelines between ETCs with differing initialization temperatures. Anomalies are relative to the initial background flow, which is defined as the mean over the first 12 hours of the simulation.

Although both of the ETCs presented in Figure 3-9 are in similar stages of their lifecycle (as determined by the temporal evolution of EKE), the contrasting structures between the two simulations demonstrate the different influences driving cyclogenesis. Development of the ETC in the warmer, moister environment does not appear to be supported by significant upper-level forcing, as demonstrated by comparing the upper-level PV analyses presented in Figures 3-9a and 3-9d. Negative PV anomalies associated with the underlying convection are present above the cyclone center in the 200-300 hPa layer, and the positive upper level PV generally associated with baroclinic development is located well to the west of the low-level cyclone. In contrast, baroclinically-driven large-scale ascent at upper levels is already present at the same relative

time in the cooler case, where a large, positive PV anomaly sits just to the west of the center of circulation. At mid-levels (Figures 3-9b and 3-9e), the anomaly maps between the two simulations differ, with the cooler environment exhibiting positive PV anomalies in the cold sector of the cyclone and also along the warm conveyor belt as it travels north of the cyclone center, while the ETC in the warmer environment exhibits positive PV anomalies along mesoscale frontal regions extending from the center of the SLP minima – a signal of circulation induced by localized convective activity in the warmer simulation. Finally, the distributions of low-level PV in Figures 3-9c and 3-9f indicate contrasting distributions of diabatic heating and generation of positive PV anomalies. Anomalies are generally spread out across the cyclone in the cooler, baroclinic case compared to a concentration of PV in intense, small-scale anomalies in the warmest case, which includes a significant amount of diabatic forcing.

Consideration of the entire PV structure for both systems demonstrates varied processes at work between the two simulations. The 292 K case, a cooler and drier simulation, is characterized by large-scale motions, with little distortion of large scale PV anomalies. These ETCs are reminiscent of the classic Norwegian cyclone model (Bjerknes 1919; Bjerknes and Solberg 1922). However, the increase in diabatic influence with additional moisture content and temperature leads to diabatic surrogates for the canonical PV gradient in ETC development. Such a process is more reminiscent of diabatic Rossby waves from Parker and Thorpe (1995), a diabatically-driven mode of cyclogenesis explored further in Chapter 4, and a transition in development regime compared to the cooler, drier ETCs of the baroclinic regime.

### ***3-6: Conclusions***

To examine the effects of a changing climate system on extratropical cyclones, a set of sensitivity experiments was constructed within an idealized modeling environment. This set of

experiments covered two aspects of a future changing climate: changes in baroclinicity (due to modification of the jet speed) and changes in moisture content (due to changes in temperature and water vapor). Both of these factors were first investigated in isolation in univariate sensitivity tests that explored the effect of moisture. These experiments were followed by a bivariate experiment simultaneously modifying both parameters in a wider examination of future climate scenarios.

Modifications to the baroclinicity of the domain resulted in stronger ETCs in both dry and moist experiments, with increasing maximum EKE and decreasing SLP minima in environments with stronger baroclinicity. This result follows traditional baroclinic theory, and an increase in LHR at mid and lower levels was also observed within ETCs in environments with progressively greater baroclinicity. This LHR increase mirrored an increase in the spatial extent of non-convective precipitation within the ETCs, eventually becoming the dominant mode of precipitation for ETCs in the most baroclinic environments. While cyclone size decreased slightly in more powerful ETCs, increases in LHR were broad and spatially spread out throughout the cyclone, leading to minimal scale contraction and continued strengthening, and to consistently monotonic responses in our strength metrics.

This behavior stood in contrast to the thresholding behavior exhibited in the bulk temperature sensitivity test. As temperature and moisture content increased, both ETC strength metrics exhibited non-monotonic behavior. These results are consistent with Booth et al. (2013) and Pfahl et al. (2015), but have been achieved via a coupled moisture-temperature scheme that lends greater realism to our perturbations. Decreases in strength occurred beyond southern boundary initialization temperatures of approximately 300 K – 304 K, a point after which cyclone size also decreased sharply. In these warmer, moister ETCs, diabatic heating played an

increasing role, especially early in the development process. Shifts in diabatic heating occurred vertically, rather than expanding horizontally. LHR profile maxima shifted upwards at this same temperature threshold. In addition, PV analysis revealed the existence of a diabatic Rossby vortex during cyclogenesis within warmest simulations.

These responses suggest that ETCs can be separated into at least two distinct regimes along their sensitivity to temperature and moisture content. ETCs within cooler and drier environments exhibit slower development times, but grow to larger sizes at maturity, during which the times of maximum EKE and minimum SLP are separated by 12-24 hours. Precipitation within these ETCs is dominated by a non-convective, stratiform mode. The diabatically-driven regime consists of ETCs within warmer, moister environments. These rapidly forming ETCs exhibit quicker development but are smaller in horizontal extent. At maturity, their times of maximum EKE and minimum SLP are closely aligned. In these ETCs, convective processes restrict the conversion of potential energy in the surrounding environment by increasing the vertical redirection of energy and momentum, limiting the meridional extent.

Building beyond previous univariate-based studies, we expanded the parameter space to encompass simultaneous changes in two environmental variables, allowing for a more comprehensive examination of future climate conditions. These bivariate sensitivity tests focused on a reduced parameter range to gain better computational coverage of a more climate-relevant parameter space, and allowed for examinations of feedbacks and interaction between our selected parameters. The results from the bivariate test matched the conclusions of both univariate tests, and demonstrated non-monotonic EKE response with changes in bulk temperature for all baroclinicities tested. ETC size was also shown to decrease with increasing temperature/moisture as well as increasing baroclinicity, regardless of the metric used to define

the time of maximum strength. The advantages of the bivariate testing also allowed relative comparisons to be made about ETC dependencies on the parameters, with a 4 K increase in temperature equivalent to an 8% change in baroclinicity across the linearly responding portions of the parameter space. This work demonstrates the need to examine future climate scenarios by examining changes in multiple variables (or forcing factors) simultaneously. Such an analysis will facilitate a more complete understanding of the response of ETCs to changes in climate, in which changes to environmental variables such as temperature, moisture, and baroclinicity occur not in isolation, but simultaneously. It should also be noted that results were insensitive to changes in convective and/or microphysical parameterizations.

In aiming to explore the sensitivity of ETCs within a wide range of current and future climates, rather than specific climate scenarios, our focus on understanding the dynamics and intricacies of the parameter space led us to simplify this environment, choosing to use a constant  $f$ -plane configuration for the Coriolis parameter and disabling radiative processes. Chapters 4 and 5 will expand upon these circulations, providing further steps toward untangling the web of complex feedbacks within ETCs by introducing a non-constant Coriolis parameter and radiative processes into the model configuration.

Experiment #	Description	# of Runs	Southern Boundary Surface Initialization Temperatures (K)	Jet Amplitude Factors
1	Univariate Baroclinicity Test	6	[300]	[0.4, 0.6, 0.8, 1.0, 1.2, 1.4]
2	Univariate Bulk Temperature Test	6	[288, 292, 296, 300, 304, 308]	[1.0]
3	Bivariate Test	121	[288, 290, 292, 294, 296, 298, 300, 302, 304, 308]	[0.8, 0.84, 0.88, 0.92, 0.96, 1.00, 1.04, 1.08, 1.12, 1.16, 1.20]

**Table 3-1.** F-plane experiment descriptions.

Test type:	Dry Bulk Temperature Test						Dry Jet Amplitude/Baroclinicity Test					
Run Parameter:	288 K	292 K	296 K	300 K	304 K	308 K	0.4	0.6	0.8	1.0	1.2	1.4
Minimum SLP Time	255	243	249	249	240	246	N/A	354	294	249	225	204
Maximum EKE Time	276	276	273	273	273	273	N/A	N/A	321	273	240	216
Difference	21	33	24	24	33	27	N/A	N/A	27	24	15	12

**Table 3-2.** Time to maximum EKE and minimum SLP for dry univariate sensitivity tests (in hours)

Test type:	Moist Bulk Temperature Test						Moist Jet Amplitude/Baroclinicity Test					
Run Parameter:	288 K	292 K	296 K	300 K	304 K	308 K	0.4	0.6	0.8	1.0	1.2	1.4
Minimum SLP Time	255	258	255	234	228	228	N/A	321	282	234	207	186
Maximum EKE Time	276	276	267	252	231	228	N/A	N/A	300	252	219	201
Difference	21	18	12	18	3	0	N/A	N/A	18	21	12	15

**Table 3-3.** Time to maximum EKE and minimum SLP for moist univariate sensitivity tests (in hours)

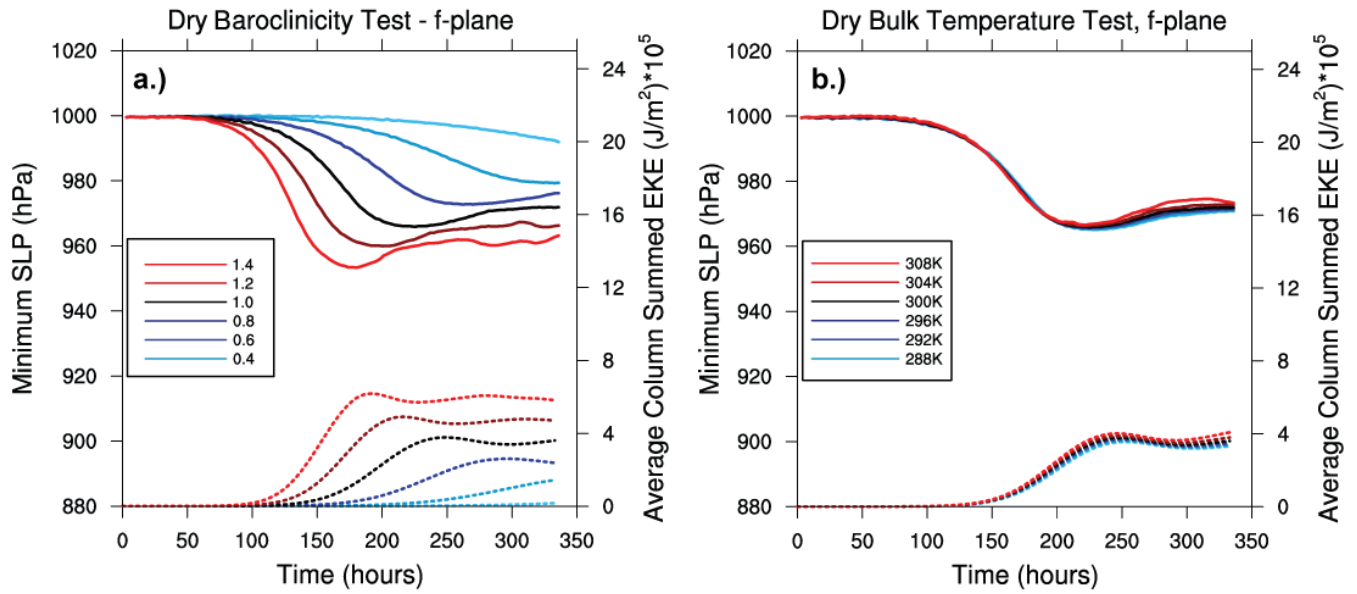


**Figure 3-1.** Column-summed EKE averaged within the entire domain (dashed lines) and minimum SLP (solid lines) for the 6 runs spanning the dry baroclinicity univariate test (a) and dry bulk temperature univariate test (b) on an *f*-plane.

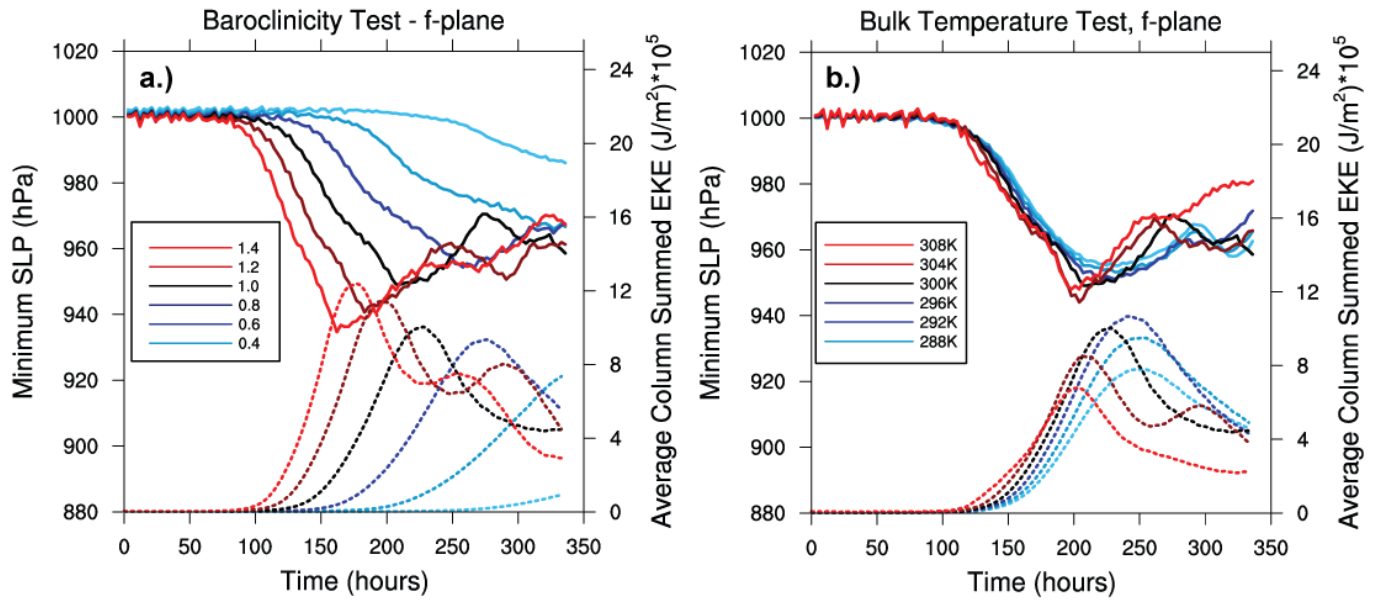


**Figure 3-2.** Full domain-averaged column-summed EKE (dashed lines) and minimum SLP (solid lines) for the 6 runs spanning the moist baroclinicity univariate test (Figure 3-2a, left panel) and moist bulk temperature univariate test (Figure 3-2b, right panel) on an  $f$ -plane.

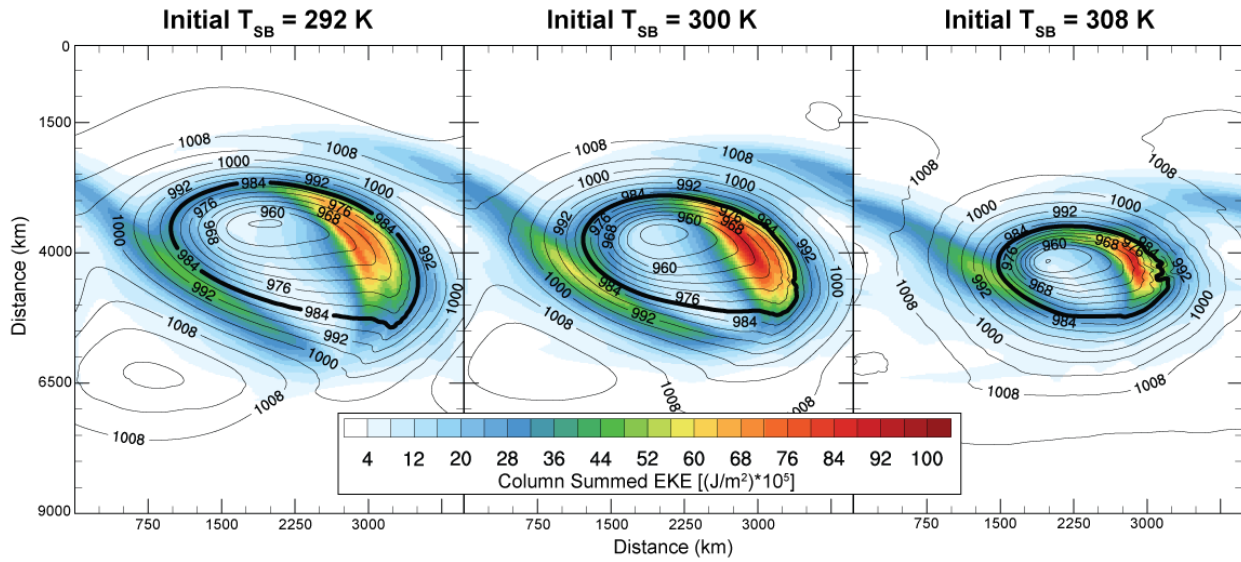


**Figure 3-3.** Plan view map of the distribution of EKE at time of maximum EKE for three ETCs in the bulk temperature test on an  $f$ -plane. Initial surface temperature at the center of the domain is given in each title, and correspond to the southern boundary initialization temperatures of 292 K (left), 300 K (middle), and 308 K (right). Bolded contour in each figure is representative of the storm size diagnostic used in the bivariate tests. On the ordinate axis, 0 indicates the northern edge of the model domain.

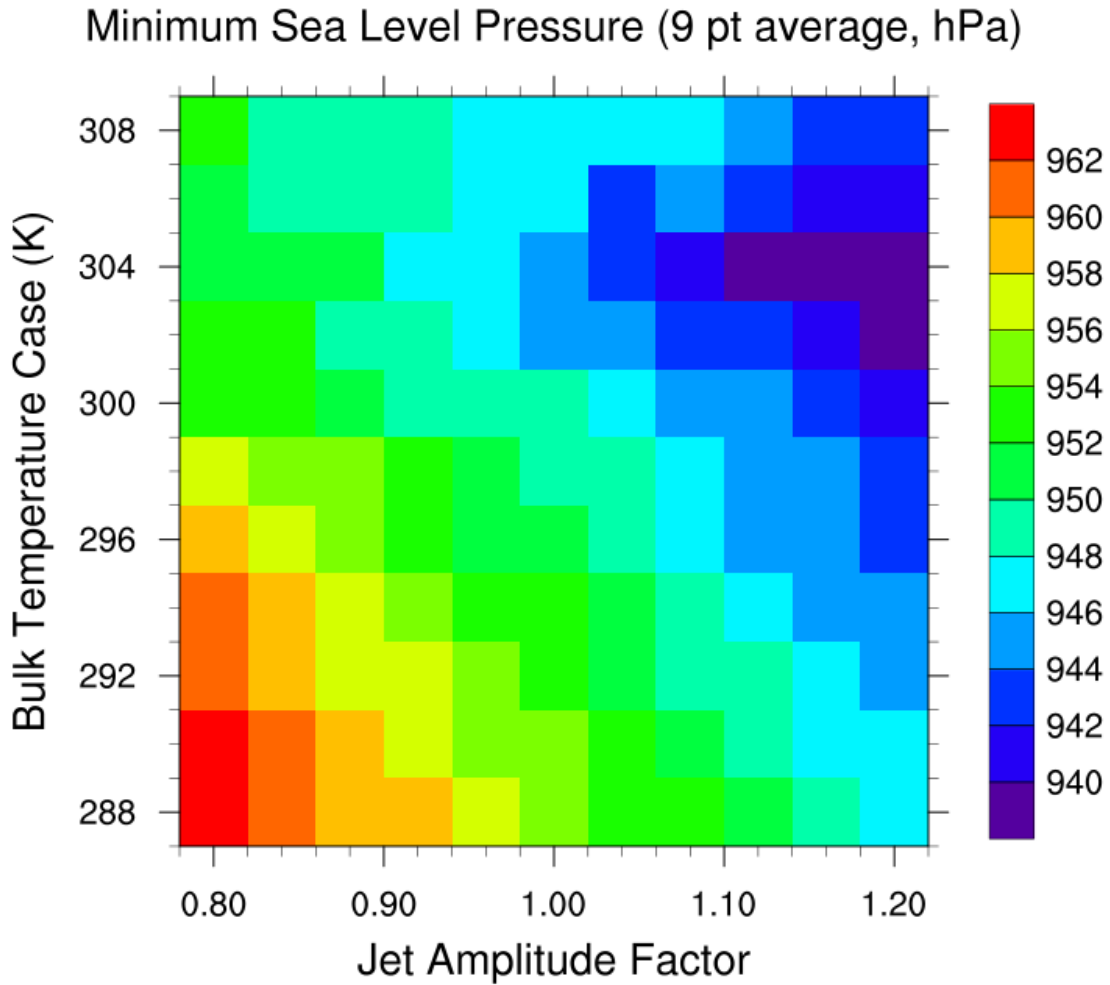


**Figure 3-4.** Minimum SLP (in hPa) during the lifetime of each ETC tested in the bivariate sensitivity test on an  $f$ -plane. The 9 point minimum SLP is determined by taking the average SLP of a 3 by 3 gridpoint box centered on the minimum SLP point in the domain.

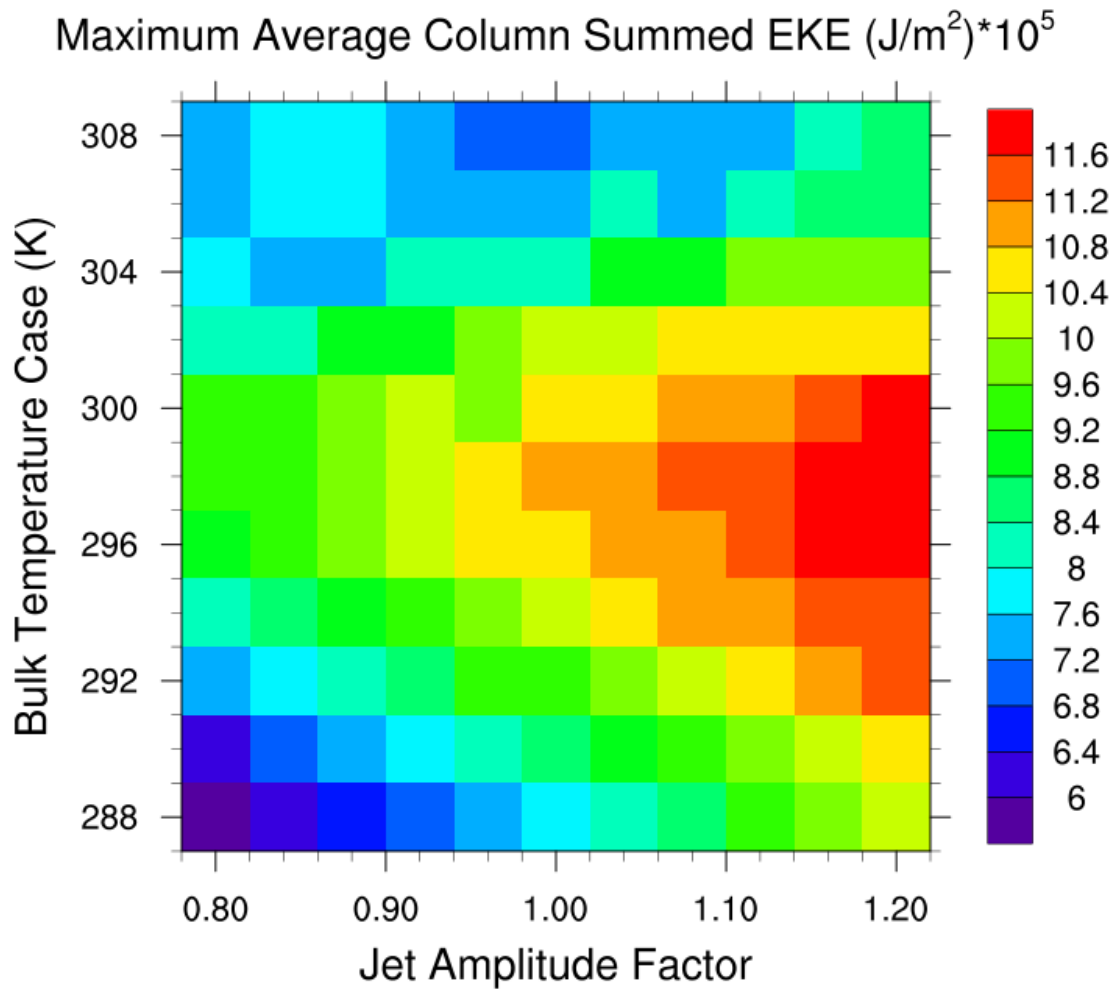


**Figure 3-5.** Maximum value of the average column-summed EKE (in  $(\text{J/m}^2)*10^5$ ) during the lifetime of each ETC in the bivariate sensitivity test on an  $f$ -plane.

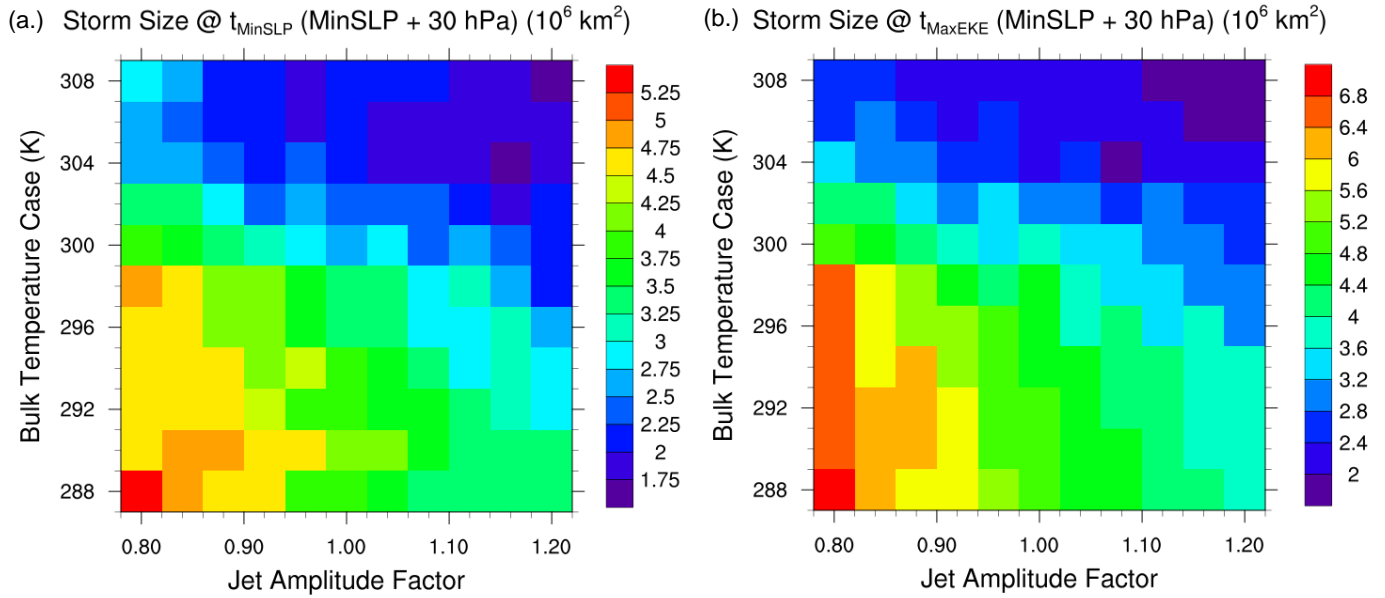


**Figure 3-6.** Storm size (in  $\text{km}^2$ ) at the times of maximum EKE (Figure 3-6a, left panel) and minimum SLP (Figure 3-6b, right panel) for the bivariate experiment on an  $f$ -plane. Storm size is determined by taking the area within a threshold contour with a value of the minimum SLP of the ETC at that time plus 30 hPa.

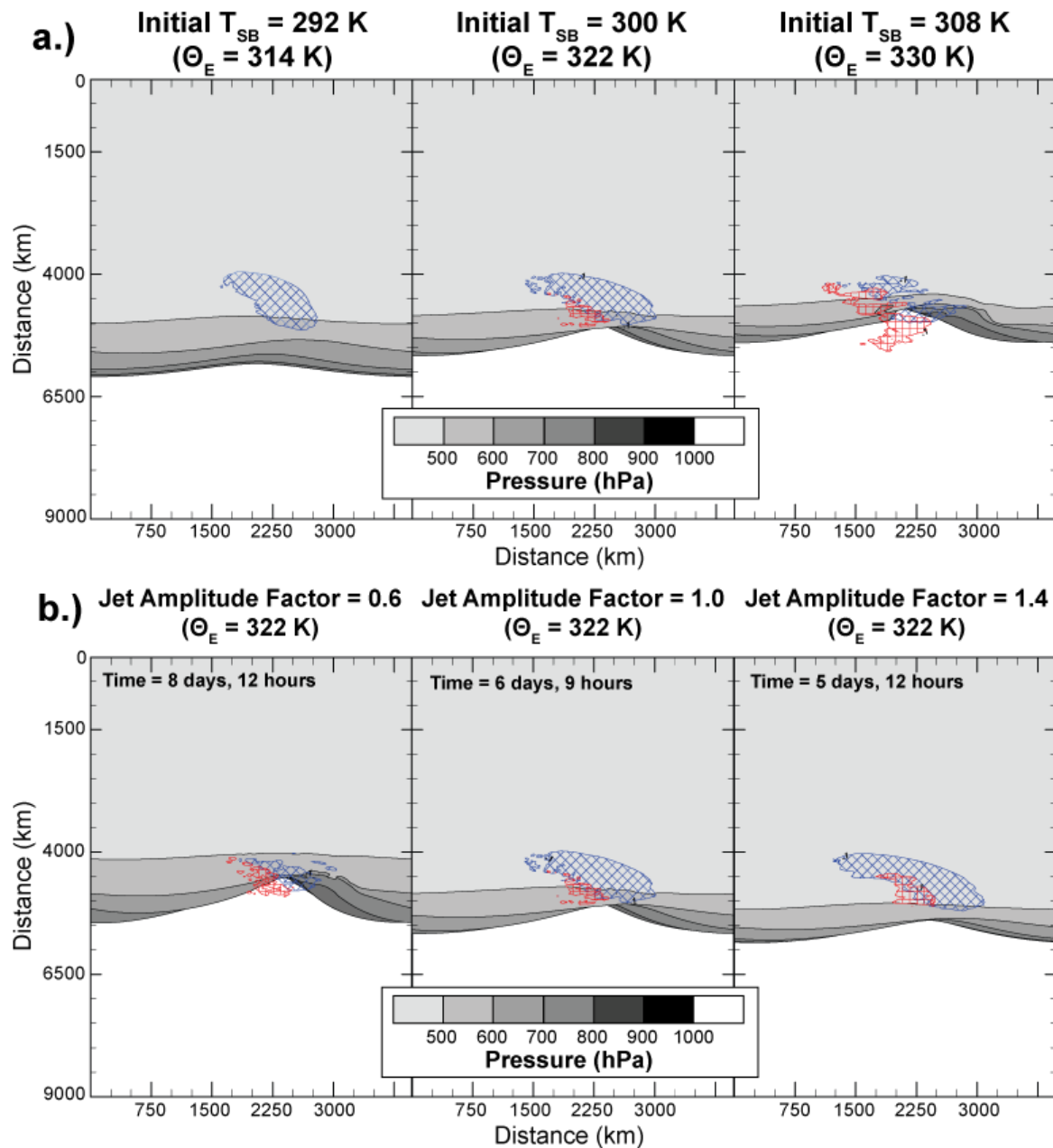


**Figure 3-7.** Frontal maps of three selected ETCs in each univariate test on an  $f$ -plane at 24 hours after the first precipitation, with overlaid precipitation contours. Fronts are displayed by contouring a specific equivalent potential temperature value representative of the frontal area at intervals of 100 hPa. Overlaid precipitation hatching indicates areas where precipitation rates of over  $1 \text{ mm hr}^{-1}$  are recorded for convective (red hatching) and non-convective (blue hatching) modes of precipitation. Figure 3-7a (top row) displays the 292 K, 300 K, and 308 K runs from the bulk temperature univariate test, while Figure 3-7b (bottom row) displays the 0.6, 1.0, and 1.4 runs from the baroclinicity univariate test.

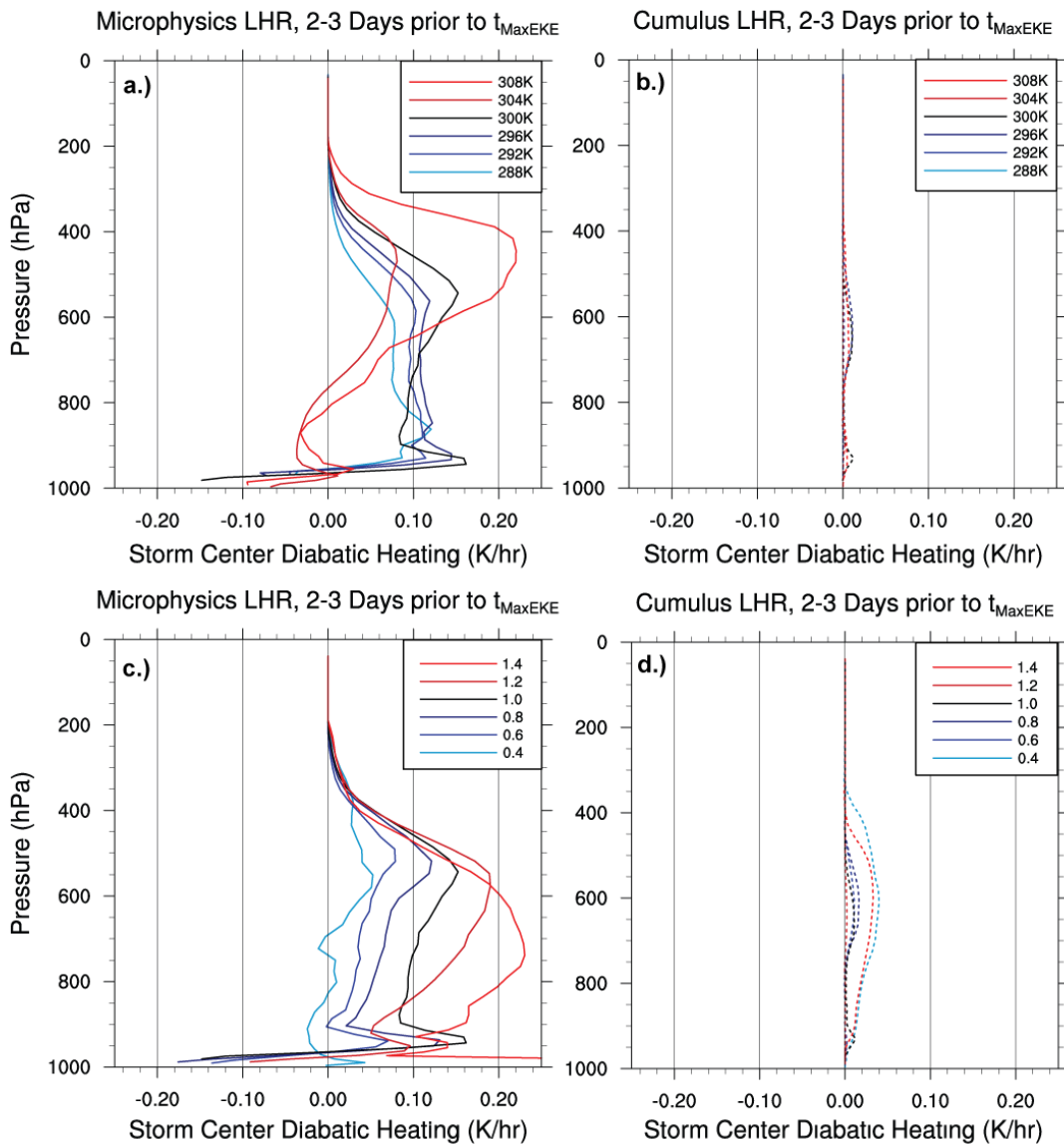


**Figure 3-8.** Averaged latent heat release (LHR) profiles in a 40 by 40 gridpoint box centered on the cyclone center. For each of the two univariate experiments on an  $f$ -plane, contributions to the LHR profiles are broken down into microphysical contributions (3-8a for the univariate bulk temperature cases, 3-8c for the univariate baroclinicity cases) and cumulus parameterization contributions (3-8b for the univariate bulk temperature cases, 3-8d for the univariate baroclinicity cases)

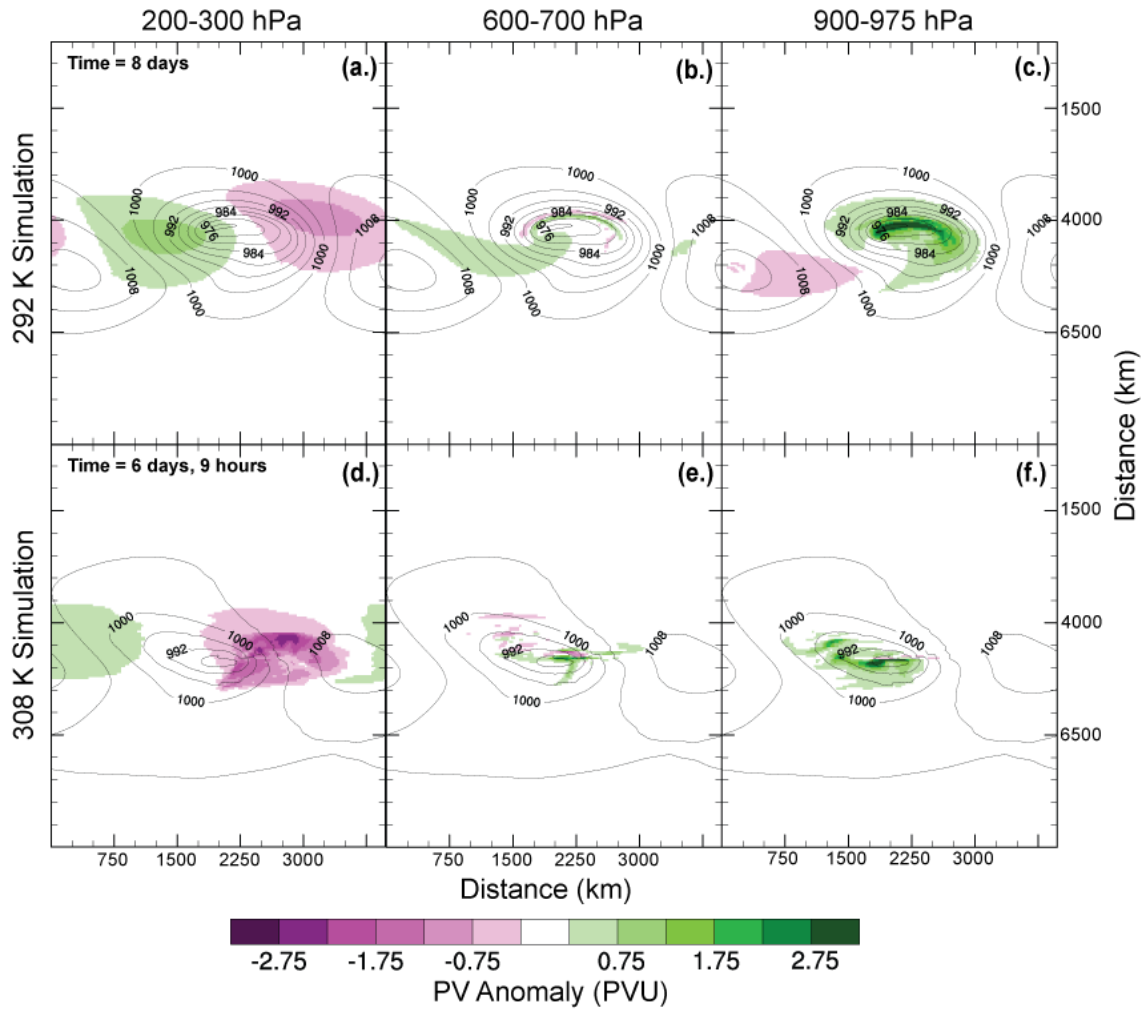


**Figure 3-9.** Potential vorticity anomaly analysis (in PVU) midway through development (as measured by EKE) for both the 292K and 308 K simulations on an  $f$ -plane, with sea level pressure contours overlaid (in hPa). PV anomalies are taken relative to the first 12 hours of each simulation.

## Chapter 4: Evaluation of ETC Sensitivity Using Latitudinally-Varying Coriolis Configurations

### *4-1: Introduction*

With our suite of sensitivity experiments on an  $f$ -plane complete, we now consider the assumptions inherent in this constant-value construction used in some idealized sensitivity work. Although sometimes dictated by model architecture, Coriolis configurations are frequently viewed as a choice – not a sensitivity factor. Regardless, the configuration used should accurately reflect the environment around the phenomenon of interest. While the constant value of the  $f$ -plane configuration is of correct order, it fails to capture the latitudinal variation of the Coriolis force in the midlatitudes. Therefore, we adjust our model setup to employ a linear approximation of the Coriolis parameter known as the beta-plane approximation, first introduced by Rossby (1939). Furthermore, we will not view this adjustment as a choice without consequence; rather, we will examine its potentially far-reaching effects on ETCs. In considering the effect of the beta-plane on ETC genesis and development, we will find that we must consider the maximum extent to which diabatic influences can affect ETC cyclogenesis and development. Canonical models of development solely rely on baroclinic methods to explain ETC morphology. However, it was demonstrated in Chapter 3 that developing ETCs also are affected by non-baroclinic influences, including the introduction of a diabatic Rossby vortex (DRV).

The concept of diabatic modes of development has its roots in convective convergence and tropical cyclogenesis, with the work of Charney and Eliassen (1964), who introduced the

concept of “conditional instability of the second kind” (CISK), which forms when low-level convergence results in significant LHR. In examining the evolution of polar lows, Craig and Cho (1988) combined the Eady model of baroclinic instability with CISK, finding that disturbances brought about purely through the release of CISK were indeed possible within the extratropical latitudes under the right conditions. This work was extended by work by Raymond and Jiang (1990) & Snyder and Lindzen (1991), who observed that diabatic heating could act as a stand-in for PV gradients within baroclinic waves.

Over time, these CISK-related features became known as “diabatic Rossby waves” (DRW), a term likely coined by Parker and Thorpe (1995). DRWs grow and propagate by diabatic generation of positive low-level PV anomalies after initiation of warm thermal advection. Propagation and growth of DRWs continues as long as there is enough baroclinicity present to provide a trigger for low-level convergence along a frontal boundary. Convergence triggers more convection and the release of further diabatic heating, and the propagation of the system continues. In a DRW framework, baroclinicity takes on a supporting role in cyclogenesis, with diabatic heating arising as the dominant mechanism. Interest in DRWs increased with reanalysis of the 1999 winter storm “Lothar” which found that a DRW was an instrumental precursor to its formation (Wernli et al. 2002). Moore and Montgomery (2004, 2005) further expanded on these shorter-scale diabatic disturbances and introduced the terminology “diabatic Rossby vortices” (DRVs), attributing their existence to both baroclinic and diabatic effects that are independent of upper-level forcing. Since then, the importance of recognizing and forecasting DRVs has led to significant work in the area, including a climatology of these features (eg. Boettcher and Wernli 2013, 2015; Moore et al. 2013).

As a side note, while confusing, the use of both DRWs and DRVs in labeling these features is equivalent – each term emphasizes different aspects of the feature. While early work like Snyder and Lindzen (1991) and Parker and Thorpe (1995) emphasized the self-propagating wave-like nature of the feature, Moore and Montgomery (2004, 2005) focused on the vortex-like isolation of the PV anomaly. An excellent summary of the semantic history of the feature can be found in the appendix of Boettcher and Wernli (2013).

Regardless of nomenclature, the existence of DRVs is the result of significant latent heat release within moderately baroclinic environments, and represents the opposite extreme from the traditional baroclinic models of ETCs, such as Bjerknes (1919). A continuum can be theoretically established covering this wide range of features, including DRVs that serve as the seed for ETC genesis. Within this chapter, we move our idealized model configuration towards a more realistic consideration of the Earth system by including a latitudinally-varying Coriolis parameter. In doing so, we find ETCs that span across this continuum from baroclinic to diabatic, and propose a three-regime classification of these systems. Specifics of the modeling configuration used along with an explanation of the experiments performed are presented in Section 4-2. The results of these experiments are presented in Section 4-3 (univariate) and Section 4-4 (bivariate). After comparison of the results to a fully realistic Coriolis configuration in Section 4-5, we move to a discussion of some of the dynamical features in Section 4-6. Finally, in Section 4-7, we compare the results in this chapter with the previously presented  $f$ -plane results, before summarizing our conclusions in Section 4-8.

## 4-2: Methods and Experiment Design

For consistency and comparability with the results from the previous chapter, we again perform our experiments using Version 3.5.1 of the Weather Research and Forecasting Model, the full configuration of which is described in Chapter 2. As in the previous chapter, we again omit the usage of any radiative scheme for simplification and ease of comparison with Booth et al. (2013) and other results. However, we now diverge from the previous model configuration by acknowledging the latitudinal dependence of the Earth's Coriolis force by utilizing the beta-plane approximation. A suite of univariate sensitivity tests using a spherical calculation of the Coriolis parameter is also performed (presented in Section 4-5) to test the robustness of the beta-plane approximation within these simulations.

First proposed by Rossby (1939), the beta-plane approximation attempts to find a middle ground between the constant value assumption of the  $f$ -plane and the non-linear complexity of the actual Coriolis parameter. It is a linear approximation of the Coriolis parameter, and for the midlatitudes, is formulated as follows:  $f = f_0 + \beta_0 (y - y_0)$ , where  $f_0 = 2\Omega\sin(\varphi_0)$  and  $\beta_0 = 2\Omega\cos(\varphi_0)/a$ . The radius of the Earth is symbolized by  $a$ , the Earth's angular velocity ( $7.292 \times 10^{-5} \text{ rad s}^{-1}$ ) is symbolized by  $\Omega$ , and  $y_0$  symbolizes the center point of the domain in the  $y$ -direction, a reference point from which distance can be calculated. The reference latitude at this point,  $\varphi_0 = 43^\circ\text{N}$ , is chosen so that the center of the domain has an identical Coriolis magnitude for both the  $f$ -plane and beta-plane configurations, as well as being nearly identical with the actual value of the Coriolis parameter at that latitude. Figure 4-1 demonstrates the values for both the  $f$ -plane and beta-plane assumptions as well as the calculated values of the Coriolis parameter for latitudes in our domain. Immediately evident is the improved realism of the beta-plane approximation over the constant  $f$ -plane assumption, especially through the

midlatitudes of the domain, where the ETC will be forming. In improving the realization of the Coriolis parameter within the model configuration and acknowledging the importance of the Coriolis force in ETC development, we make another step toward representing the full climate system. Moreover, we consider the change in Coriolis configuration as a sensitivity, a stark change from much of the idealized literature which considers the Coriolis configuration as a methodology choice within their model setup, often opting for the simpler  $f$ -plane.

As in Chapter 3, we design our experiments to have some comparability with our own past results. Therefore we repeat the three experiments from Chapter 3, now with the beta-plane configuration. For reference, these experiments are listed in Table 4-1. This experimental construction allows direct comparison between the two sets of results, as all other variables are held constant between the  $f$ -plane and beta-plane simulations. As before, the first two experiments are 6-simulation univariate sensitivity experiments testing ETC univariate sensitivity to bulk temperature and baroclinicity. The final experiment is a 121-simulation bivariate experiment utilizing simultaneous changes within the range of the univariate experiments.

### ***4-3: Univariate Sensitivity Results***

#### ***4-3.1 Dry Simulations***

As with the  $f$ -plane results, we first perform the univariate experiments in a dry configuration. At initialization, no moisture is present, a cumulus parameterization is not used, and latent heat release from the microphysics scheme is neutralized. Figure 4-2a shows the minimum SLP and maximum EKE results from the dry variation of Experiment 1, the univariate baroclinicity test. As expected from baroclinic theory and the corresponding experiment in

Chapter 3, increasing the baroclinicity of the domain results in stronger ETCs, regardless of metric – simulation-minimum SLP decreases and simulation-maximum EKE increases. Furthermore, the timing of cyclogenesis and time to maturity are accelerated as baroclinicity increases. Within the most baroclinic domain, cyclogenesis begins approximately 100 hours into the simulation, 24-36 hours sooner than in the control baroclinicity case with a jet amplitude factor of 1.0. In the most weakly baroclinic environment (a jet amplitude factor of 0.4) development barely begins prior to the end of the 14 day simulation. In addition, the development timeline is accelerated in the most baroclinic environments, with the time between genesis and maturity decreasing and deepening rates increasing – all indications of robust developmental changes.

The dry configuration is also applied to Experiment 2, the univariate bulk temperature test, with Figure 4-2b displaying the results for both strength metrics. Unlike the dry baroclinicity results, changing the bulk temperature of the domain in a dry configuration has a negligible effect during cyclogenesis and development of the ETC, with small differences post-maturity due to surface fluxes. With surface fluxes removed, results are nearly identical through the entire the 14-day simulation, as demonstrated in Figure 4-3. These dry configurations of Experiments 1 and 2 thus confirm that our beta-plane modifications to the original B2013 channel model are accurate and behave consistently prior to the addition of moisture. Indeed, the results presented in Figure 4-2 are quite similar to the corresponding  $f$ -plane experiments presented in Figure 3-1. While the  $f$  and beta planes are consistent in dry dynamical conditions (perhaps leading to assumptions that the choice of Coriolis configuration is irrelevant), the differences between these two configurations are clear once the effects of moisture are included.

### 4-3.2 Moist Simulations

Having established the performance of the beta-plane initialization procedure in dry dynamics cases, we then move to the moist variations of Experiments 1 and 2. As in Chapter 3, this involves using the second step of our initialization procedure to insert water vapor into the domain and the activation of moist processes and diabatic heating within the model. Otherwise, model configuration and parameterizations are identical to the dry variations of Experiments 1 and 2.

Figure 4-4a displays the two strength metrics for the moist variation of Experiment 1, the univariate baroclinicity test. ETCs in environments with weaker and stronger baroclinicity than our default value are depicted with blue and red lines, respectively. While both minimum SLP and EKE values demonstrate run-to-run behavior consistent with the theoretical work of Eady, QG theory, and the corresponding results from Chapter 3, there are notable deviations. All ETCs in Figure 4-4a are approximately half as strong as their f-plane counterparts, using the simulation-maximum EKE metric. Exact percentages range from a minimum decrease in strength of 47.7% at a jet amplitude factor of 0.8 to a maximum decrease in strength of 53.4% at a jet amplitude factor of 1.0. Response of simulation-maximum EKE between dry and moist variations of this experiment is similar, especially between jet amplitude factors of 0.8 and 1.4. Increasing the jet amplitude factor, and thus the environmental baroclinicity, does increase EKE, but only slightly. Moreover, there is a glimpse of non-monotonicity in the response of the simulation-maximum EKE value for each run between jet amplitude factors of 0.8 – 1.2, the causes of which will be discussed further in Section 4-6. In contrast, the response of minimum SLP to environmental baroclinicity is monotonic, as minimum SLP decreases with increasing baroclinicity, although this response is not linear.

We then turn to the results of the moist bulk temperature sensitivity test. The combined results for minimum SLP and EKE are presented in Figure 4-4b, with the warmest runs in red and the coldest runs in blue. Initial development of each ETC takes place at slightly different rates, with warmer runs developing quicker, indicating that the addition of more moisture at warmer temperatures leads to more rapid development, as also seen in the  $f$ -plane results. However, the later stages of cyclogenesis differ significantly from the  $f$ -plane simulations, with the warmest two runs (304 K and 308 K), demonstrating a secondary period of cyclogenesis after a pause in development about 160 hours (7 days) into the simulation. The cooler runs exhibit traditional cyclogenesis patterns resulting in a U-shaped graph of minimum SLP. Furthermore, as temperature increases, the simulation-minimum SLP increases with increasing temperature; and, due to the two-stage cyclogenesis, the timing of the minimum is delayed in the warmest runs.

The EKE values in Figure 4-4b also contrast with this experiment's  $f$ -plane counterpart (Fig. 3-3b). The two-stage cyclogenesis observed in the warmest runs is also evident in the EKE results, as the 308 K simulation develops sooner and deepens quicker than cooler runs. While more subtle, two-stage cyclogenesis can be inferred in EKE timeline of the 304 K run, and even in the 300 K run, in which the two stages are concurrent enough that the EKE timeline appears as a plateau at peak strength between 220-270 hours. Shifting to the values of cyclone-maximum EKE, non-monotonicity again exists, as in the  $f$ -plane counterpart. However, the non-monotonic trend is now reversed, with simulation-maximum EKE values decreasing between 288 K – 300 K, and increasing in strength at temperatures warmer than 300 K. We can therefore infer that moist processes hamper the development of the ETC up until this point. Furthermore, the sensitivity to individual steps on either side of the minimum value displays different behaviors, as the decreases of the cooler runs are large when compared to the small increases in EKE

between the 300 K – 308 K runs. This unequal sensitivity could indicate separate growth factors, explored further in Section 4-6.

#### ***4-4: Bivariate Sensitivity Results***

While univariate tests are useful, we also acknowledge that they are an incomplete examination of ETC sensitivity, especially when considered in isolation. Therefore, we now include simultaneous perturbation of both the bulk temperature/moisture in the domain as well as the baroclinicity. Simultaneous perturbations nudge our idealized framework towards a fuller evaluation of future climates, with changes in multiple environmental characteristics.

Figure 4-5 displays bivariate results for the simulation-minimum SLP output metric. The dominant sensitivity is to baroclinicity, as ETCs in both relatively colder/drier and warmer/moister environments exhibit decreases in minimum SLP with increases in baroclinicity. Again, this qualitative trend generally follows the traditional baroclinic growth theory; however, from a quantitative perspective, minimum SLP does not decrease linearly with increasing baroclinicity; decreases are less rapid in the warmer/moister simulations than in the colder/drier runs. As also present in the univariate baroclinicity experiment, there is noisiness to the minimum SLP field, partially due to the coarser horizontal grid spacing of the model. Another factor could be the chaotic nature of convection, which has been previously demonstrated to play a greater role in ETCs at warmer temperatures. Moreover, the “threshold temperature” (at which convection begins to limit development) is colder in beta-plane experiments than in the  $f$ -plane experiments presented in Chapter 3. These differences will be explored in greater detail later in Section 4-7.

Using the same line of analysis as in the univariate tests, Figure 4-6 displays the simulation-maximum EKE value for each of the 121 runs in the bivariate test. The parameter space exhibits the presence of multiple regimes, with the lower half of the figure demonstrating a coherent response function characterized by increasing values of maximum EKE as baroclinicity increases, in addition to some sensitivity to temperature – a clear codependence on both environmental characteristics. This pattern is similar to the  $f$ -plane results in Section 3-4, with the temperatures for the maximum value of EKE and the coherent response boundary transposed to cooler values than in the  $f$ -plane bivariate experiment, a difference expanded upon in Section 4-7. Warmer than approximately 298 K, ETCs (at all baroclinicities) shift into a new response regime. Response to increases in both variables is non-monotonic and inconsistent, with a secondary maximum between 304 K – 308 K. The only qualitative conclusion possible is an increase in EKE within more strongly baroclinic environments, similar to the qualitative conclusion made in the bivariate minimum SLP results. Finally, it should be noted that given the results in both Chapter 3, and in the univariate results presented in Section 4-3, the minimum in the upper left-hand corner of the diagram is expected. Environments in this portion of the parameter space are warm and moist, but lack significant baroclinicity – the critical ingredient for ETC development.

#### ***4-5: Inclusion of a Spherical Coriolis Configuration***

As discussed in Section 4-2, the beta-plane is a linear approximation of Earth's Coriolis force commonly used in idealized modeling. However, in order to test the accuracy of the beta-plane approximation and robustness of our results, we run a third set of univariate tests with a configuration more representative of Earth's actual Coriolis force, using a spherical formulation,

$f=2\Omega*\sin(\varphi)$ , where  $f$  is the Coriolis parameter,  $\Omega$  represents the Earth's angular speed of rotation,  $7.292 \times 10^5 \text{ rad s}^{-1}$ , and  $\varphi$  is the latitude in radians. The center of the domain is anchored at  $43^\circ\text{N}$  latitude, so that the domain represents  $3^\circ - 83^\circ\text{N}$  latitude. We repeat the two moist univariate sensitivity tests, the results of which are presented in Figure 4-7a (moist univariate baroclinicity test) and Figure 4-7b (moist bulk temperature univariate test).

Comparison of Figure 4-7a with Figure 4-4a, the corresponding results on the beta-plane configuration, reveals strong similarity in response between the simplified beta-plane and the spherical Coriolis configuration. Increasing domain baroclinicity yields stronger ETCs, with a slight muddling of the signal between jet amplitude factors of 0.8 and 1.2. It should also be noted that, on the whole, ETCs within this test are slightly stronger than their beta-plane counterparts. Similarities extend to comparisons between the univariate bulk temperature tests in the spherical Coriolis configuration (Fig. 4-7b) and beta-plane configuration (Fig. 4-4b). Again, strength response is similar, with only a slight shift in the temperature of the weakest ETC (as measured by average column-summed EKE) from 300 K in the beta-plane configuration to 304 K in the spherical Coriolis configuration. Again, ETCs in domains with spherical Coriolis configurations are stronger than their counterparts, but the general response function remains robust. Thus, while the beta-plane is a simplified approximation of the actual Coriolis force, the accuracy of the approximation in the midlatitudes is reasonable enough to draw robust conclusions from the simpler beta-plane configuration.

#### ***4-6: Discussion***

Within the three beta-plane experiments (univariate baroclinicity, univariate bulk temperature, and bivariate baroclinicity-temperature), there are several complex response

behaviors requiring further analysis. For the univariate baroclinicity test (wherein all runs are at a bulk temperature case of 300 K), an expected increase of strength with increasing environmental baroclinicity is present in the minimum SLP, while the EKE response is comparatively muddled. Moreover, in the univariate bulk temperature test, ETC strength surprisingly decreases in both metrics before slightly increasing at the warmest temperatures. Finally, in the bivariate test, the responses for both metrics are noisy, especially in the warmer portions of the parameter space. To understand possible response function inconsistencies, moist processes with nonlinear behavior must be considered. And so, we once again return to examining the role of convection within the beta-plane experiments.

While difficult to precisely quantify and compare convective activity between ETCs, we can obtain a close approximation by comparing the amounts of convective and non-convective precipitation. Figure 4-8 displays both of these quantities (averaged across the entire domain and over the entire simulation) for the bivariate parameter space, with Figure 4-8a displaying convective precipitation, and Figure 4-8b displaying non-convective precipitation, as partitioned by the convective scheme active within the model. Figure 4-8a demonstrates the strong correlation between temperature, moisture, and convective activity. Convective precipitation increases non-linearly with increasing temperature, with 2 K steps at warmer temperatures yielding more precipitation. In addition, there is a dependence on baroclinicity, as increasing the domain baroclinicity leads to decreases in convective precipitation amount. Therefore, the environments most conducive to convective activity are the warmest and most weakly baroclinic domains.

Figure 4-8b demonstrates that in the warmest environments, ETCs in high baroclinicity domains produce the largest amounts of non-convective precipitation, as expected in these

baroclinically-dominated situations. While increases in temperature and moisture play equally important roles in non-convective precipitation, increases in moisture content complicate the comparison of convective roles between cooler and warmer runs. Therefore, we use the convective percentage of precipitation to normalize the amount of convective precipitation (Fig. 4-8a) by the total precipitation (the sum of Figs. 4-8a and 4-8b). Figure 4-8c displays these results, confirming our intuition about the role of convection and temperature. While both convective and non-convective precipitation increase with increasing temperature, gains in convective precipitation accelerate faster at warmer temperatures and lower baroclinicity values. Therefore, the highest convective percentages (exceeding 60%) are from ETCs in warm and weakly baroclinic environments. The decrease from this maximum is rapid, as decreasing the temperature by 6 K leads to a 20% decrease in the convective percentage – a clear demonstration of the rapidly increasing role convection plays in the warmest environments.

While independently significant, the increasing role of convection with temperature also has a significant impact on the dynamical environment. As in Chapter 3, the most notable quantity used to understand convective dynamical feedback is potential vorticity, popularized by Hoskins et al (1985). Figures 4-10 and 4-11 display PV anomaly analyses from the 292 K and 308 K cases in the univariate bulk temperature experiment, with green and purple shading indicating positive and negative PV anomalies, respectively. The first 12 hours of the simulation are used as the background flow. PV is broken out into 3 levels: upper-level (200 – 300 hPa), mid-level PV (600 – 700 hPa), and low-level PV (900 – 975 hPa), chosen to provide a comprehensive picture of both convection and synoptic-scale processes, while also avoiding level adjustment for different bulk temperature cases. Finally, the precipitable water vapor is plotted with sea level pressure overlaid in the bottom row of the diagram. For each ETC, this

analysis is performed four times, as shown in Figure 4-9. The first three times, A, B, and C, are fixed with regard to the simulation start time, and are chosen to highlight PV evolution during ETC development. The final time period is fixed with regard to ETC lifetime, and depicts the PV distribution at the time of maximum EKE. All times, as well as the case names, are also labeled on the figures for reference. Combined, Figures 4-10 and 4-11 demonstrate the modification of ETC cyclogenesis processes with increases in temperature, suggesting two disparate responses. These cases bring into focus the regimes first posited in Chapter 3.

The 292 K case, presented in Figure 4-10, undergoes canonical cyclogenesis, as described by Bjerknes (1919) or Shapiro and Keyser (1990), for example. The upper-level PV forms a dipole, with the SLP minimum between a positive western PV anomaly and an eastern negative PV anomaly, shown on the top row of Figure 4-10. Simultaneously, mid-level PV exhibits no significant deviation from the background state, indicating a lack of widespread diabatic heating above 500 – 600 hPa. Finally, the low-level PV anomaly is centered on the SLP minima, indicative of the low-level circulation (and associated vorticity) associated with the developing ETC at the surface. As the ETC develops further by Time C, the low-level PV field coincides with the location of the warm conveyor belt (WCB), a region of warm, moist air ascending ahead of the cold frontal region. The WCB is visible in the precipitable water vapor product in the bottom row of Figure 4-10 as a tongue of moist air (in blue) extending to the north. The changing morphology of the WCB should be noted, as it narrows significantly towards maturity. ETC evolution also feeds back onto the large scale dynamical forcing. Upper-level PV deforms from the initial dipole and mirrors the counter-clockwise circulation of the ETC, with the positive anomaly advected southeastward, and the negative anomaly advected northward. Positive PV anomalies also develop at mid-levels, mirroring the path of parcels in the

WCB. In the 292 K case, the impact of convection is minimal to nonexistent, with the ETC responding to large-scale, synoptic forcing mechanisms.

While the 292 K case demonstrates canonical baroclinic wave development, the 308 K case, presented in Figure 4-11, reveals how vigorous convection disturbs baroclinic cyclogenesis processes. At time A, the PV dipole surrounding the SLP minimum is present, but with clear convective modification, as evidenced by the inconsistent edges and irregular shape of the negative anomaly. Such irregularity is indicative of convection underlying the 200 – 300 hPa layer in those regions. Further evidence of deep convection below 300 hPa is present in the mid- and low-level PV anomalies at Time A. Mid-level and low-level positive PV anomaly morphology matches structures expected in a diabatic Rossby vortex (DRV) as described by Moore and Montgomery (2004, 2005) and as in the  $f$ -plane results presented in Chapter 3. Positive PV anomalies stretching to the south and east of the SLP minimum at mid-levels are reminiscent of a mesocyclone and reflect DRV-induced circulation. The DRV present early in the cyclogenesis process includes a WCB-esque feature in precipitable water vapor, visible at Time A in Figure 4-11. This DRV is responsible for the initial strengthening present in minimum SLP and average EKE timelines of the 308 K case in Figure 4-4b, the first of two growth periods in both timelines, before strengthening briefly pauses.

Examination of Times B and C, at the beginning and end of the pause in development, illuminates possible reasons for the peculiar dual-development timeline present in the 308 K case (as well as the 300 and 304 K cases, albeit less visibly). By this time, the DRV has largely dissipated, although the resulting SLP minimum is still visible on the western end of the broad horizontal SLP minimum that has formed. Low-level PV anomalies still bear the signature of the DRV at Time B as well, as a small southeasterly-oriented PV streamer is still visible over the

center of the broad SLP minimum. However, the predominant forcing for continued cyclogenesis is now synoptic-scale, as at upper-levels, the positive PV anomaly present to the west of the ETC has moved east, and sits just off of the western edge of the broad SLP minimum, encouraging large-scale ascent over the ETC. As a result, the dominant PV pattern of the ETC now reflects the strung-out streamer in the 292 K case, with one key exception. Due to the influence of the DRV in early stages of cyclogenesis, the WCB is shifted well to the east of the SLP minimum and sits at the edge of the map at Time B. Although more environmental moisture is present in the 308 K case than in the 292 K case, moisture transport of the WCB is misplaced, and so the environment must adjust. This adjustment is visible in the precipitable water vapor map at Time C, where two green tongues indicate ongoing consolidation of the two WCBs: one from the initial DRV, and one forming as the ETC undergoes synoptic-scale cyclogenesis. By Time C, on the ninth day of the simulation, there are no recognizable PV features from the initial DRV, formed 72 hours prior. Nevertheless, the DRV makes a lasting impact on the ETC through modification of the environment. DRVs lead to weaker ETCs in warmer environments by reducing the conversion efficiency of available baroclinic energy. Note, however, that this is not immediately evident when examining the PV anomaly and precipitable water vapor fields for the 292 K and 308 K cases at time D, their peak EKE strength. As in the 292 K case, the WCB in the 308 K case narrows along the eastern side of the SLP minimum, and looks similar in PV fields, with PV anomalies at mid- and low-levels coincident with the WCB, and upper-level positive PV anomalies above the southern half of the cyclone. While both ETCs look similar at maturity, they represent the different pathways of cyclogenesis present in the parameter space.

#### ***4-7: Comparison of Beta-Plane and $f$ -Plane Results***

In completing identical sets of sensitivity experiments for both the  $f$ -plane and beta-plane configurations, comparisons can illuminate general characteristics of ETCs in changing environments. When initially making cross-experiment comparisons of strength metrics, it seems that no similarities exist; however, closer examination reveals that the system behaves similarly between Coriolis configurations. In illustration of this point, Figure 4-12 displays the simulation-maximum EKE value for a range of  $f$ -plane and beta-plane simulations within the moist univariate bulk temperature experiment. Note that for each of the configurations, the range of bulk temperatures used has been extended, with the beta-plane ensemble ranging between 276 K – 308 K, and the  $f$ -plane ranging between 288 K – 312 K. While figures displaying the entire EKE timeline for both tests (Fig. 3-3b and Fig. 4-4b) do not immediately reveal similarities, plotting simulation-maximum values reveals a generalized response, regardless of Coriolis configuration.

This generalized response function has two distinct features. The first of these is a parabolic function with a local maximum at approximately 284 K for the beta-plane configuration and approximately 296 K for the  $f$ -plane configuration. These parabolic responses are relatively symmetric about the local maximum, and cover the majority of the cooler end of the parameter space. The second begins at a clear breakpoint of 300 K in the beta-plane and 308 K in the  $f$ -plane configuration and is a (possibly) linear regime where simulation-maximum EKE increases with temperature. This regime's linearity is unknown, as for simulations warmer than 308-312 K, the model configuration becomes unstable and must be modified. Moreover, these temperatures approach the upper limit of expectations in a future climate. Nevertheless, we can confidently conclude that there is a clear regime shift in the warmest end of the parameter space.

Correlating the breakpoints in Figure 4-12 to the sensitivity test results in Chapter 4, it is clear that increased convection (and associated diabatic heating), specifically the initiation of diabatic Rossby vortices, is likely the trigger mechanism for response regime change. At simulations greater than the 296 K bulk temperature case, several characteristics of DRVs appear. Firstly, in Figure 4-4b, the 300 K – 308 K cases all demonstrate some variation of two-stage strengthening. While the two stages are most noticeable in the 308 K case, examination of the EKE timeline for the 300 K case reveals that there are two maximums present, but much closer in time than the warmer cases. Such two-stage strengthening is not present in the 296 K case. Furthermore, the bivariate maximum EKE results (Fig. 4-6) show a two-stage distinction, with the coherency of the response function breaking down at temperatures warmer than 300 K. This breakpoint value also explains the muddled response of the univariate baroclinicity test on the beta-plane (Fig. 4-4a). Given that all runs for that test are performed at a bulk temperature case of 300 K, the influence of convection prevents the beta-plane results from duplicating the clear result of the  $f$ -plane baroclinicity test (Fig. 3-3a). The factors behind the breakpoint transposition between the two Coriolis planes are still unclear, however.

In understanding the response shift between Coriolis configurations, it should be noted that the setup formulation for all three tests is identical – all simulations begin in a balanced state. The key difference is the makeup of the forces balanced. In balancing the initial state with a non-constant Coriolis parameter, slight differences to the jet profile (and thus also the temperature field, since the model begins in thermal wind balance) result in slightly different temperature profiles between nominally identical  $f$ -plane and beta-plane cases. The cross-section in Figure 4-13 displays these initial differences in temperature at the center of the domain – in the beta-plane runs, there is warming at levels below the jet maximum, and slight cooling above.

Taken as a whole, these slight differences (with a maximum difference of less than 4 K) result in a steeper lapse rate within the beta-plane cases. Thus, the beta-plane runs are marginally more unstable than their  $f$ -plane counterparts – making them more prone to convection at lower thresholds of temperature and moisture. Increasing convection leads to DRV initiation at cooler temperatures (relative to the  $f$ -plane results), resulting in DRV interference with cyclogenesis and regime shift at a lower temperature threshold in the beta-plane sensitivity test. This indirect impact of Coriolis configuration on initial lapse rate and regime breakpoint confirms the convective influence on the response of ETCs to temperature.

#### ***4-8: Conclusions***

In including latitudinally-varying Coriolis parameters in our idealized setup, we were able to capture a more realistic picture of ETCs, as the Coriolis force plays a non-negligible role in midlatitude dynamical systems. Primarily, we utilized a linear beta-plane approximation, although a spherical Coriolis parameter was tested to confirm the results of the beta-plane experiments. As in Chapter 3, which utilized an  $f$ -plane, we performed variations on three primary experiments: Dry and moist variations of a univariate baroclinicity sensitivity test, dry and moist variations of a univariate bulk temperature test, and a moist bivariate test which simultaneously modified baroclinicity and bulk temperature.

After confirming correct operation of the model setup in the dry variations of the univariate test, we repeated the two univariate experiments with moist processes. In the baroclinicity test, there was an increase in ETC strength with increasing baroclinicity, as measured by minimum SLP and maximum EKE. While this response was also identified in the corresponding  $f$ -plane test, the increasing influence of convection at cooler temperatures results

in a slightly muddled response in comparison. As expected, increases in non-convective precipitation are also present in ETCs within the most baroclinic environments. Moving to the univariate bulk temperature experiment, the activation of moist processes results in significant response modification as compared to the dry variation. Minimum SLP generally increases with increasing temperature, indicating weakening of ETCs in warmer and moister environments. Furthermore, simulation-maximum EKE of the ETC during the simulation shows a clear non-monotonic response to temperature, decreasing with increasing temperature between 288 K – 300 K, before slightly increasing again at bulk temperatures warmer than 300 K. During development, the EKE and minimum SLP timelines of the three warmest ETCs are characterized by a two-stage strengthening process, brought about by the initiation of DRVs in the domain, which act to interfere with traditional baroclinic cyclogenesis and limit ETC strength. DRVs are highlighted through a PV anomaly analysis early in ETC development, and signal the presence of a new regime of cyclogenesis, visible in univariate and bivariate results.

Together, the  $f$ -plane and beta-plane results presented in Chapters 3 and 4 demonstrate a generalized response of ETC to changes in both baroclinicity and bulk temperature/moisture. ETC response to increases in baroclinicity is relatively straightforward – with increasing baroclinicity, strength increases, especially in cases where convection plays a limited role. However, the response to increased bulk temperature/moisture is much more complicated and can be broken down into 3 regimes. Figure 4-14 presents a simplified sketch of these regimes and their relation to simulation-maximum EKE values. The first of these regimes, the baroclinic regime, is at the coolest end of the spectrum, and represents ETCs that grow at a slow to moderate pace. Increasing temperature and moisture in these ETCs contributes to convection and diabatic heating that increases strength. Further increases in temperature beyond the baroclinic

regime lead to the second regime, where ETCs are diabatically-limited. In these ETCs, while development may be more rapid, convection constricts the ETC by vertically redirecting momentum – resulting in a smaller, weaker ETC. These two regimes make up the parabolic arc that spans much of the parameter space. Finally, the warmest regime is characterized by the rapid development of diabatic Rossby vortices, with convection responsible for PV production at mid-levels. In this diabatically-driven regime, DRVs accelerate development, but interfere with baroclinic cyclogenesis, resulting in simulation-maximum EKE values that scale linearly with increasing temperature. While these regimes represent a nearly-complete inclusion of moist atmospheric processes, our modeling setup still lacks one key element – radiation. The inclusion of radiation brings about further complexity, explored next in Chapter 5.

Experiment #	Description	# of Runs	Southern Boundary Surface Initialization Temperatures (K)	Jet Amplitude Factors
1	Univariate Baroclinicity Test	6	[300]	[0.4, 0.6, 0.8, 1.0, 1.2, 1.4]
2	Univariate Bulk Temperature Test	6	[288, 292, 296, 300, 304, 308]	[1.0]
3	Bivariate Test	121	[288, 290, 292, 294, 296, 298, 300, 302, 304, 308]	[0.8, 0.84, 0.88, 0.92, 0.96, 1.00, 1.04, 1.08, 1.12, 1.16, 1.20]

**Table 4-1.** Beta-plane experiment descriptions.

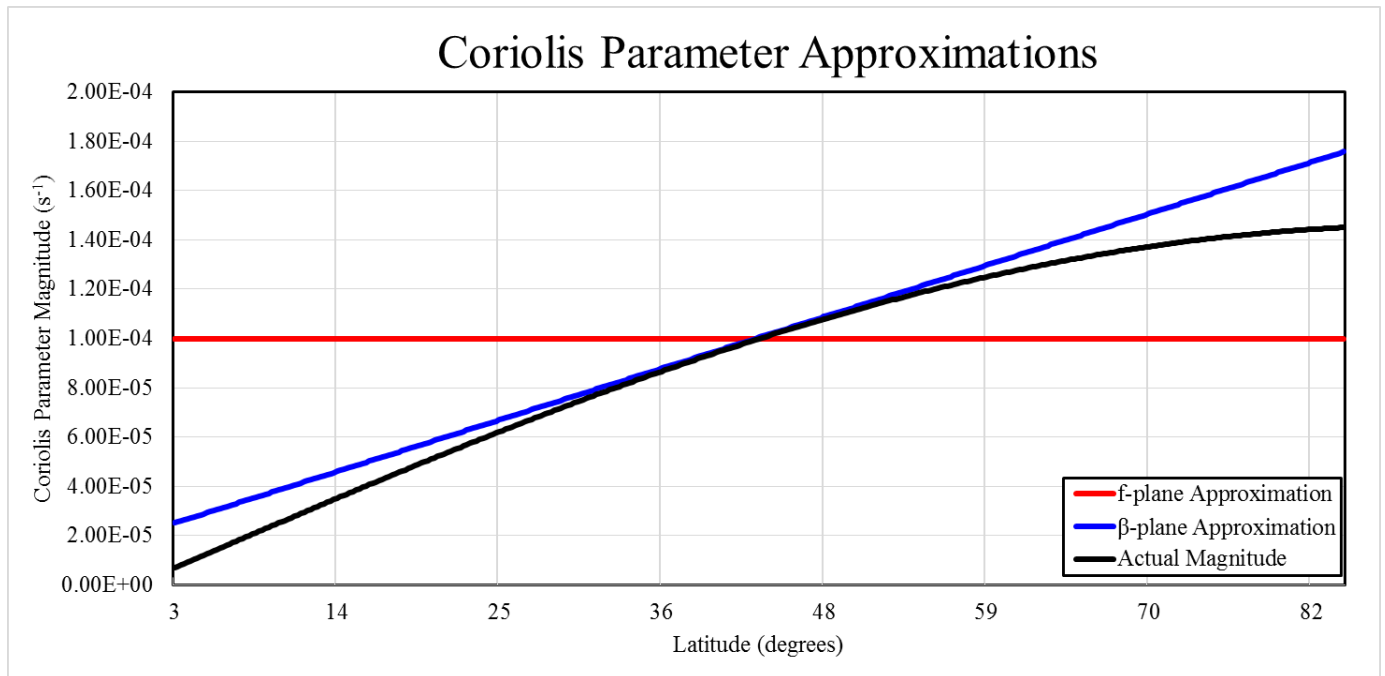


**Figure 4-1.** Magnitudes of the Coriolis parameter approximations ( $f$  plane in red, beta-plane in blue) and the calculated Coriolis parameter (for a sphere), for latitudes within the idealized channel domain used for sensitivity experiments.

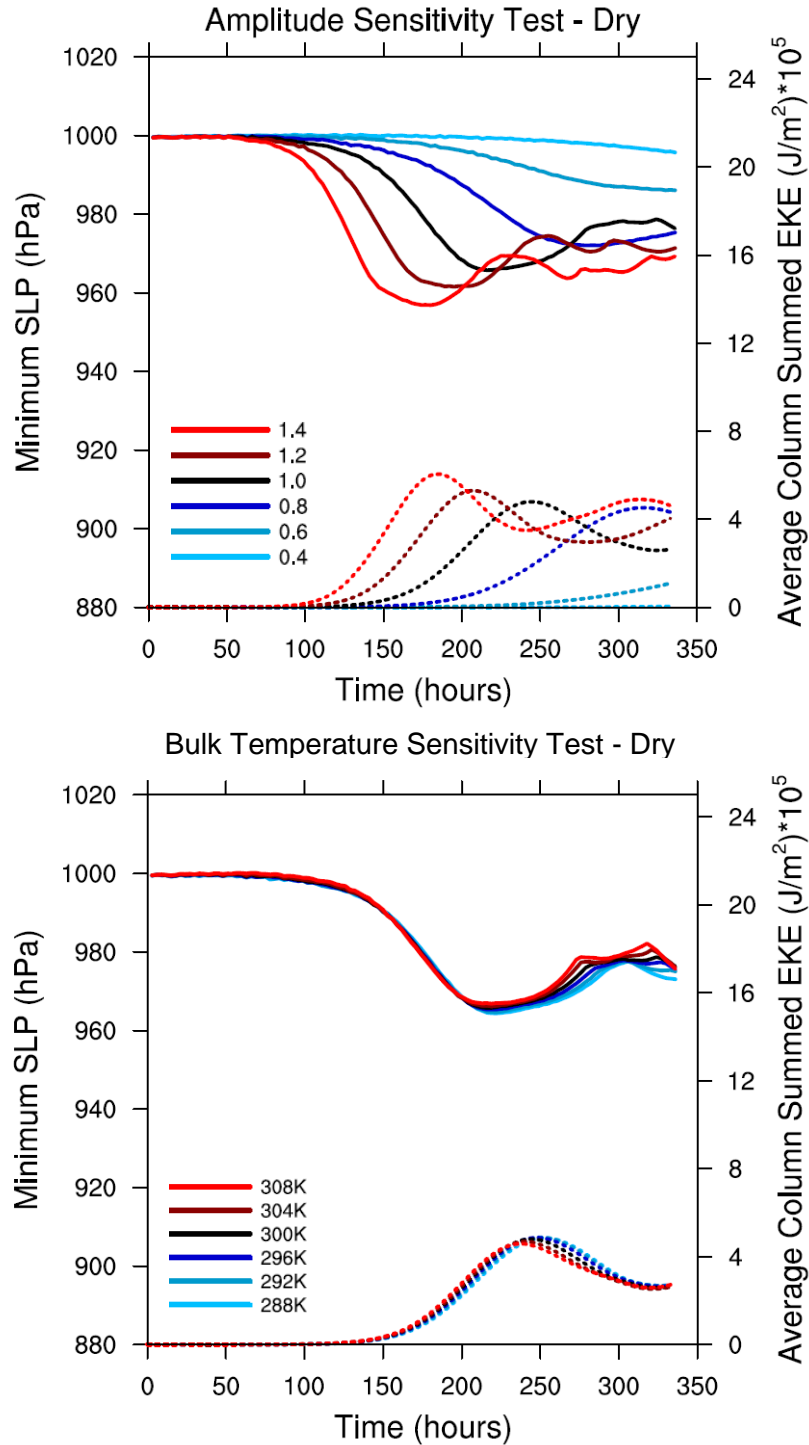


**Figure 4-2.** Average column-summed EKE (dashed lines) and minimum SLP (solid lines) for the 6 runs spanning the dry baroclinicity univariate test (Figure 4-2a, top panel) and dry bulk temperature univariate test (Figure 4-2b, bottom panel) on a beta-plane.

### Bulk Temperature Sensitivity Test – No Surface Fluxes

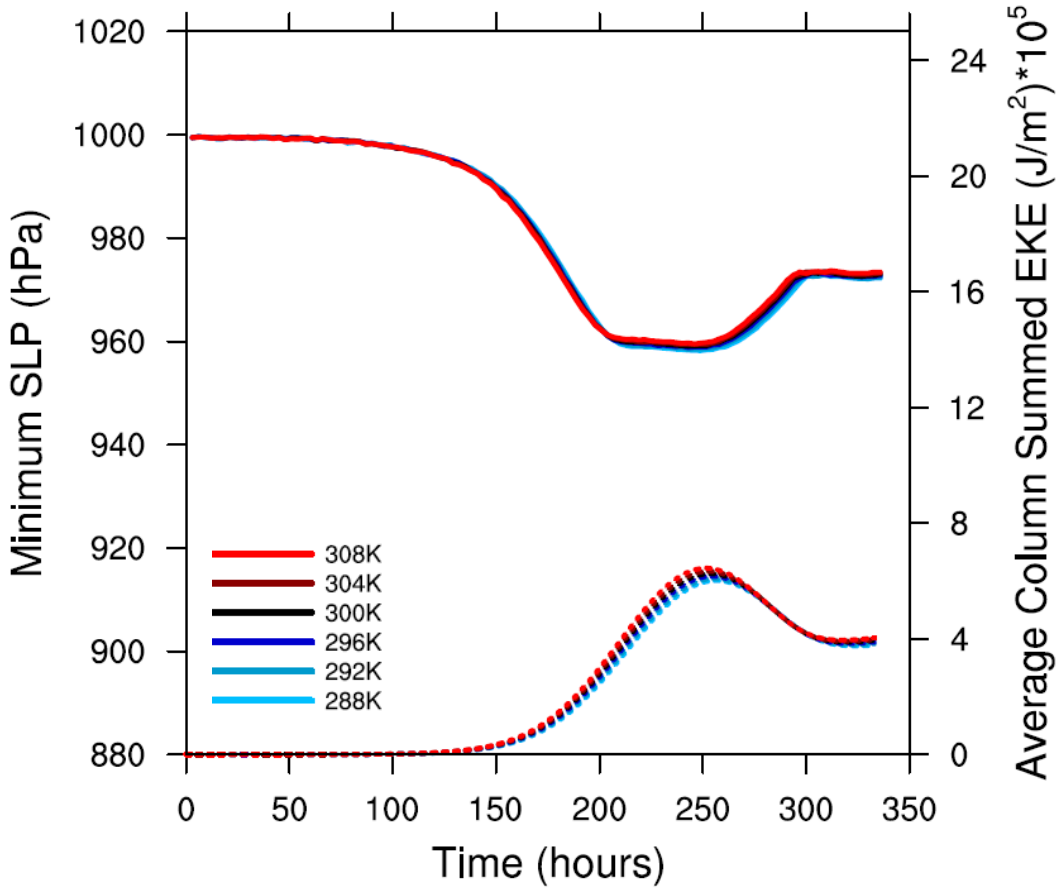


**Figure 4-3.** Average column-summed EKE (dashed lines) and minimum SLP (solid lines) for the 6 runs spanning the dry baroclinicity univariate test on a beta-plane, run without surface fluxes.

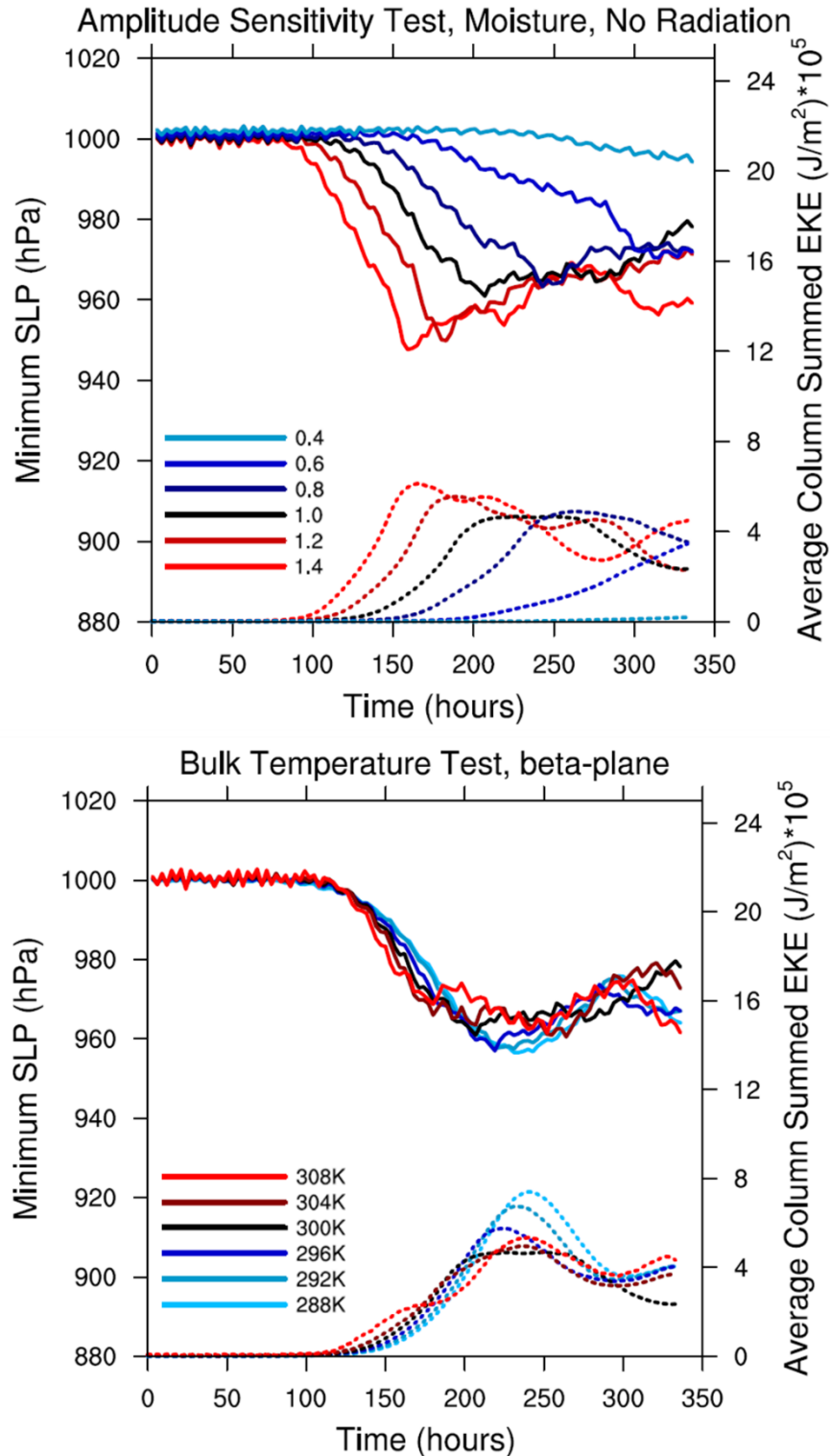


**Figure 4-4.** Average column-summed EKE (dashed lines) and minimum SLP (solid lines) for the 6 runs spanning the moist baroclinicity univariate test (Figure 4-4a, top panel) and moist bulk temperature univariate test (Figure 4-4b, bottom panel) on a beta-plane.

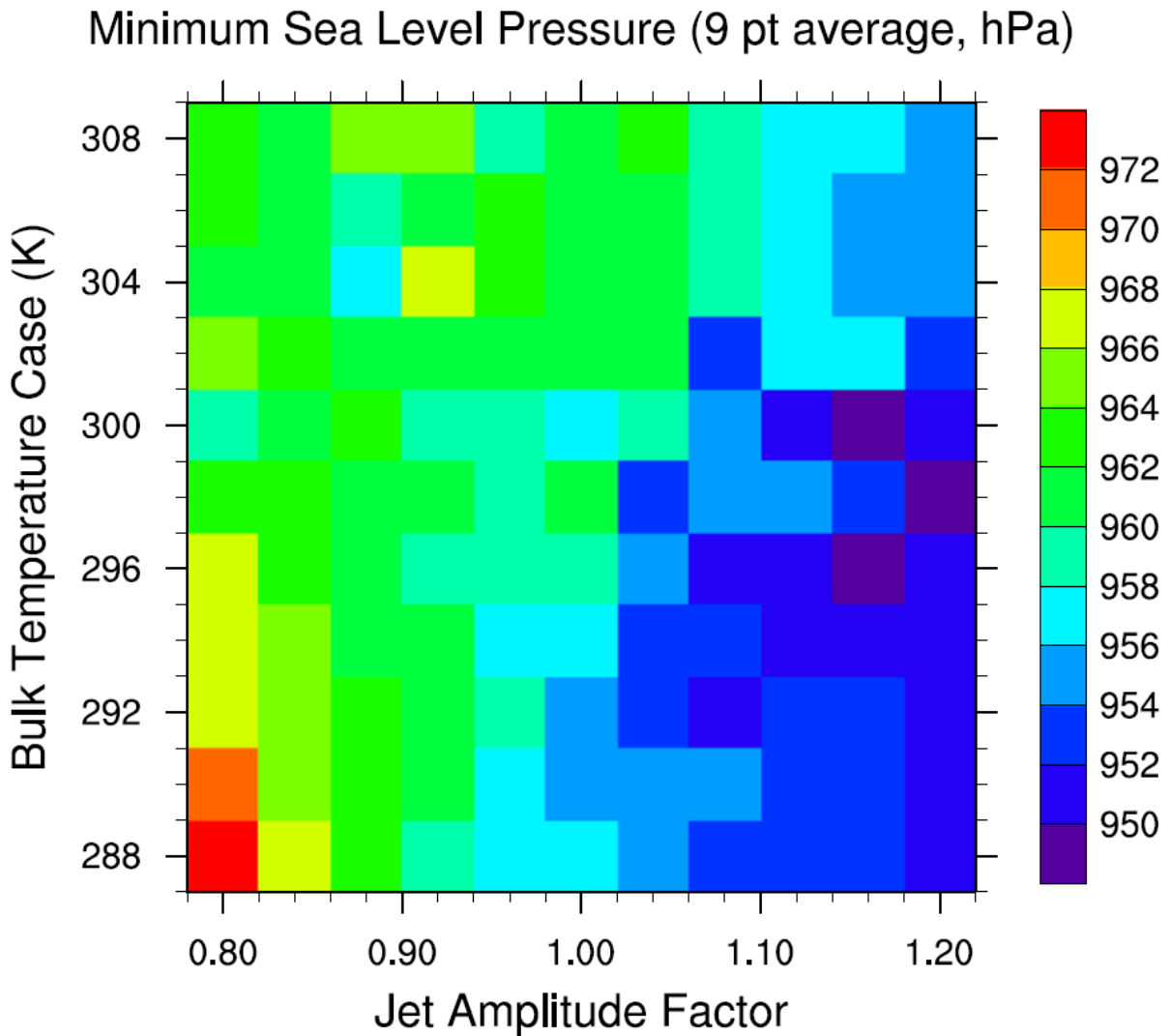


**Figure 4-5.** Minimum SLP (in hPa) during the lifetime of each ETC tested in the bivariate sensitivity test on a beta-plane. The 9pt minimum SLP is determined by taking the average SLP of a 3 by 3 gridpoint box centered on the minimum SLP point in the domain.

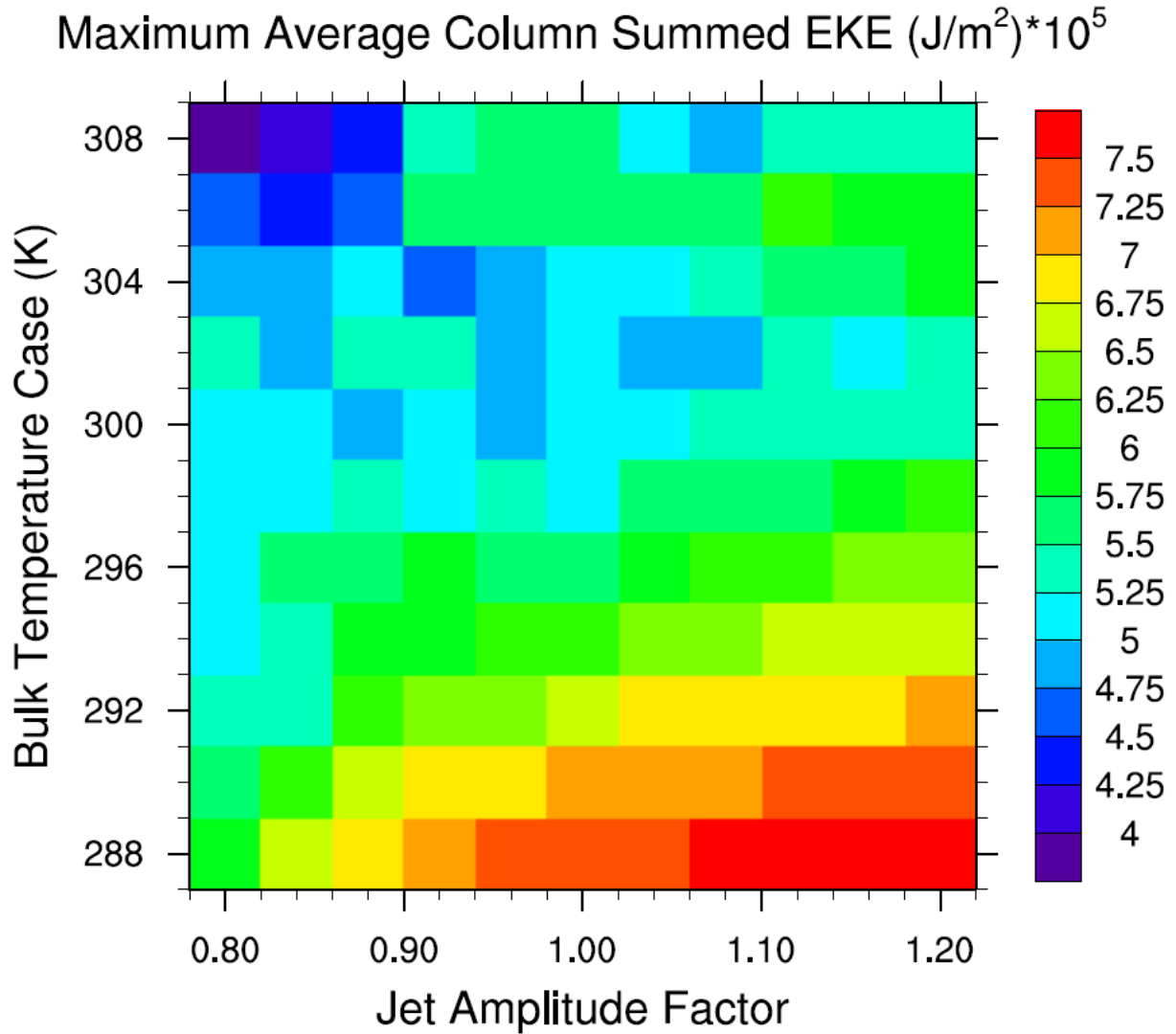


**Figure 4-6.** Maximum value of the average column-summed EKE (in  $(\text{J/m}^2) \cdot 10^5$ ) during the lifetime of each ETC tested in the bivariate sensitivity test on a beta-plane.

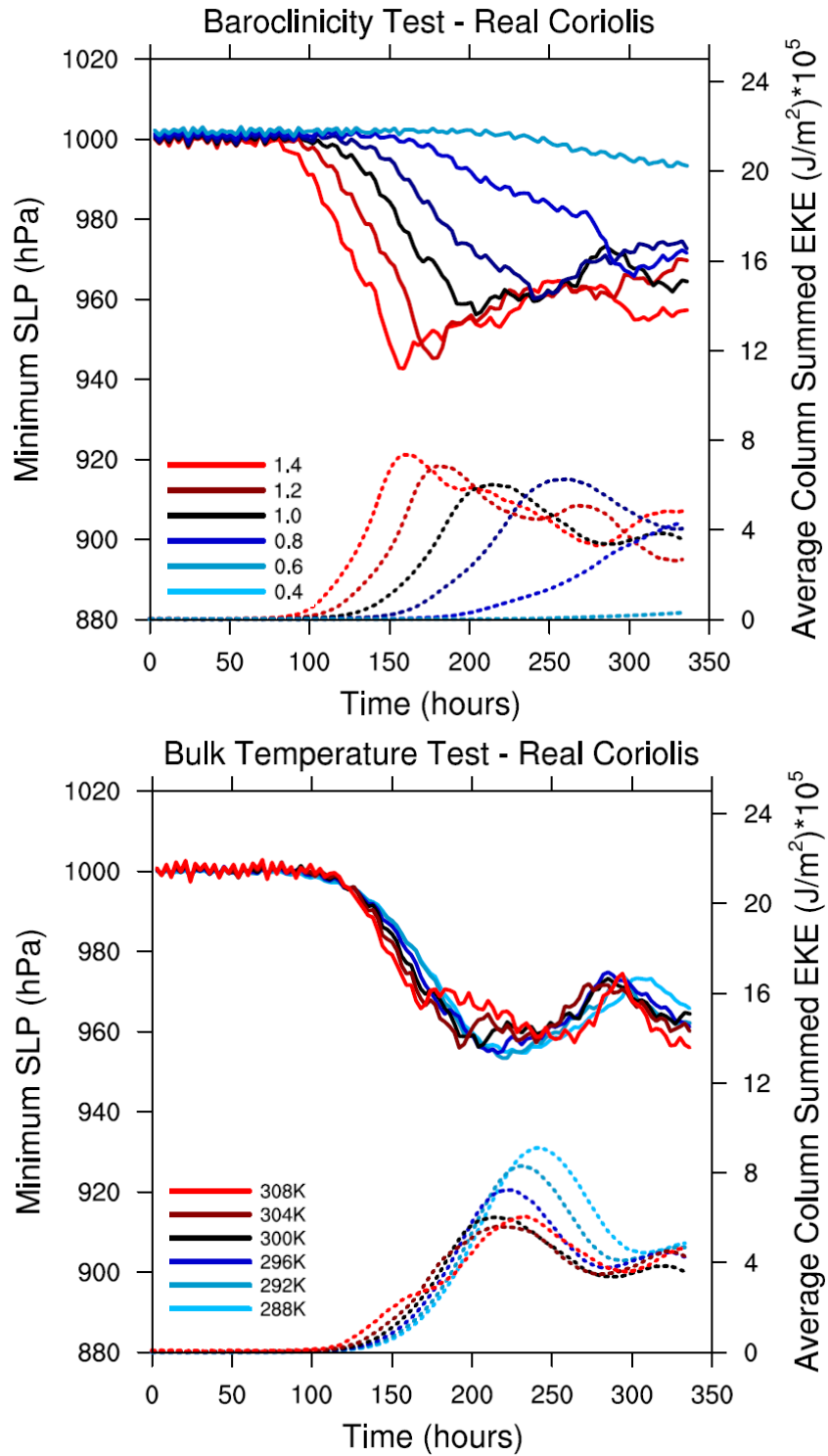


**Figure 4-7.** Average column-summed EKE (dashed lines) and minimum SLP (solid lines) for the 6 runs spanning the moist baroclinicity univariate test (Figure 4-7a, top panel) and moist bulk temperature univariate test (Figure 4-7b, bottom panel), run with a spherical Coriolis configuration.

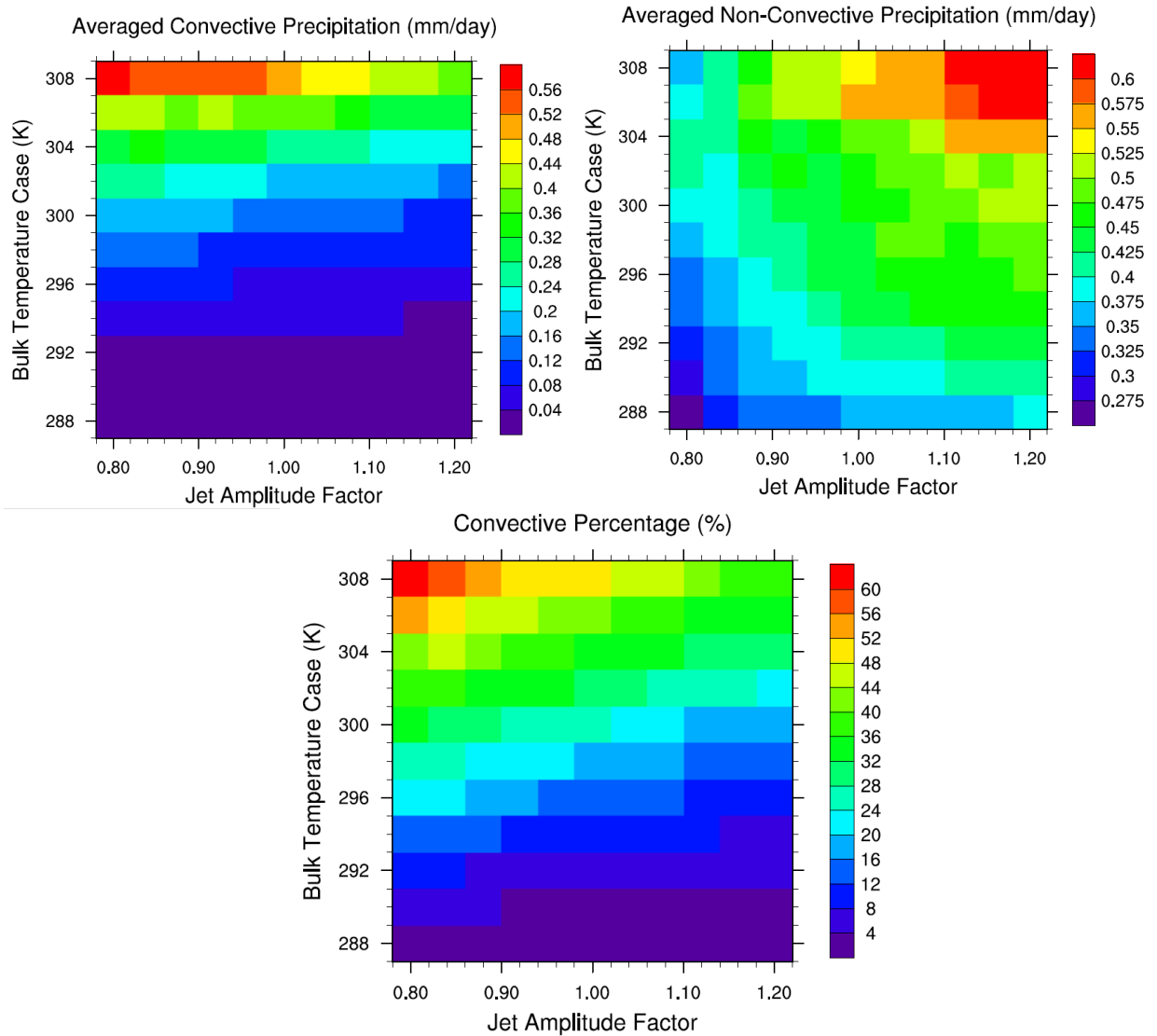


**Figure 4-8.** Averaged (over the full domain and entire simulation) values of convective precipitation (mm/day, Figure 4-8a), non-convective precipitation (mm/day, Figure 4-8b), and convective percentage of precipitation (Figure 4-8c) for each ETC in the bivariate sensitivity test on a beta-plane.

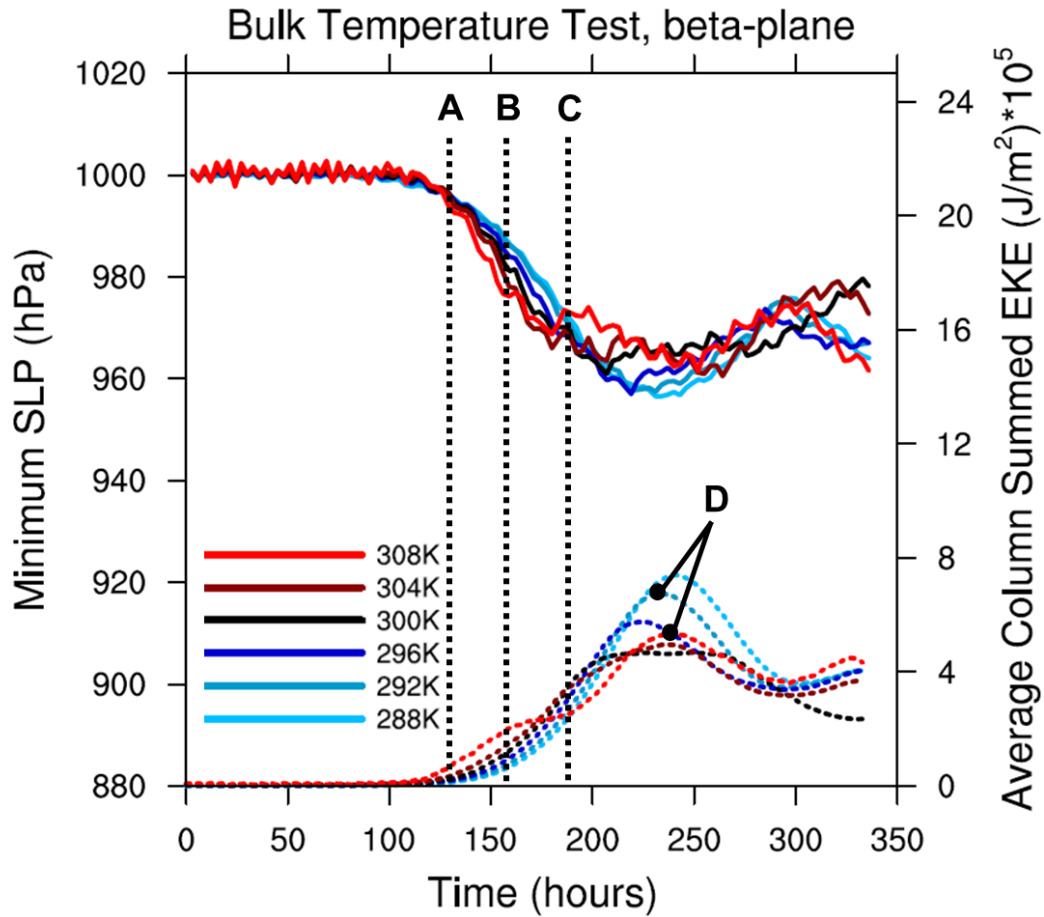
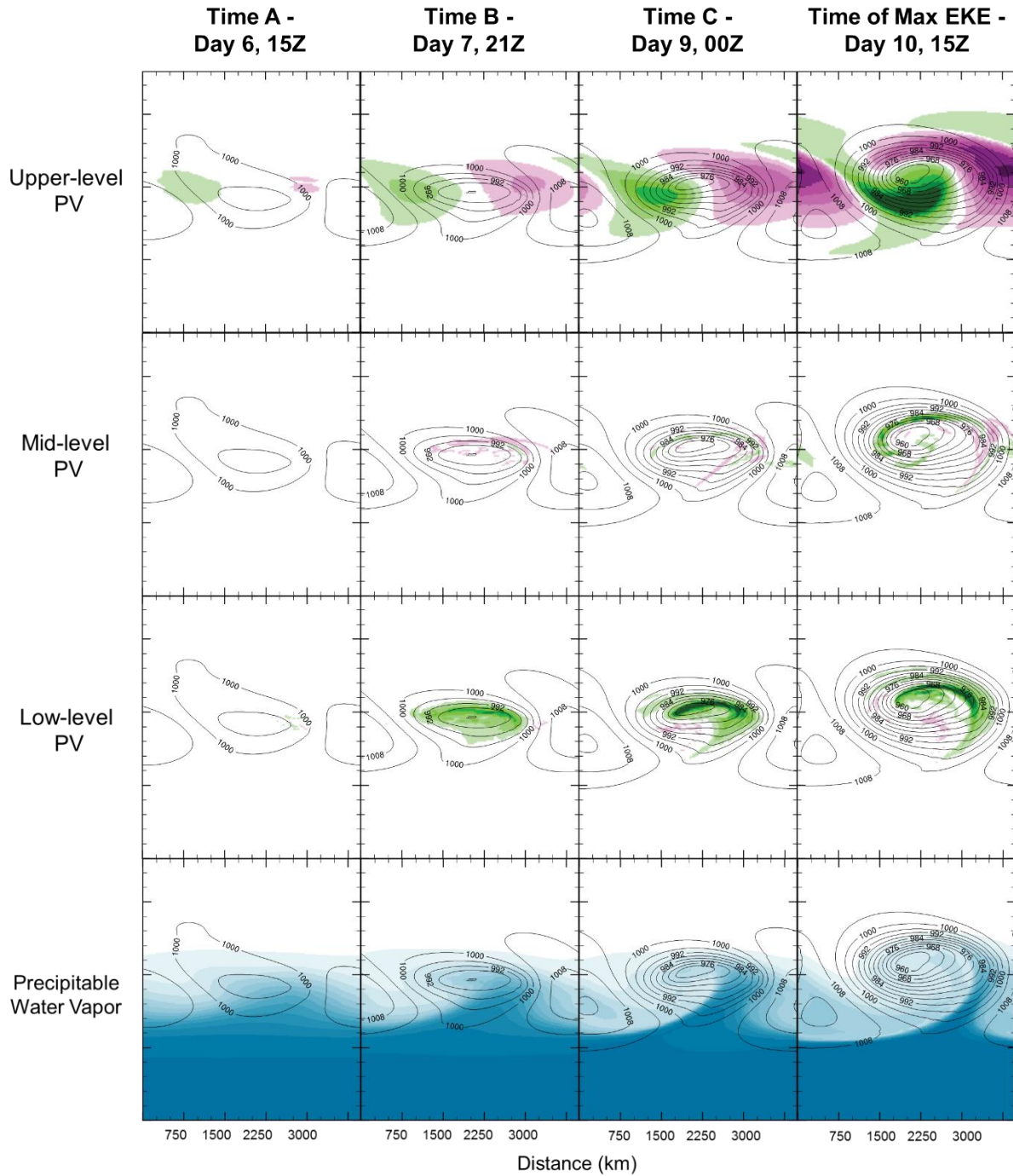


**Figure 4-9.** Times A-D of the four-panel analysis overlaid on the average column-summed EKE (dashed lines) and minimum SLP (solid lines) for the 6 runs spanning the moist bulk temperature univariate test on a beta-plane. Time D is at the time of maximum EKE.

## 292K Case



*Top Row:* 200-300 hPa Potential Vorticity Anomaly [calculated off of 0-12 hour average, PVU]  
*Second Row:* 600-700 hPa Potential Vorticity Anomaly, displayed only where relative humidity is greater than 80% [PVU]  
*Third Row:* 900-975 hPa Potential Vorticity Anomaly, displayed only where relative humidity is greater than 80% [PVU]  
*Fourth Row:* Precipitable Water Vapor [inches]

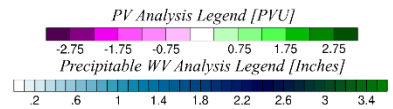
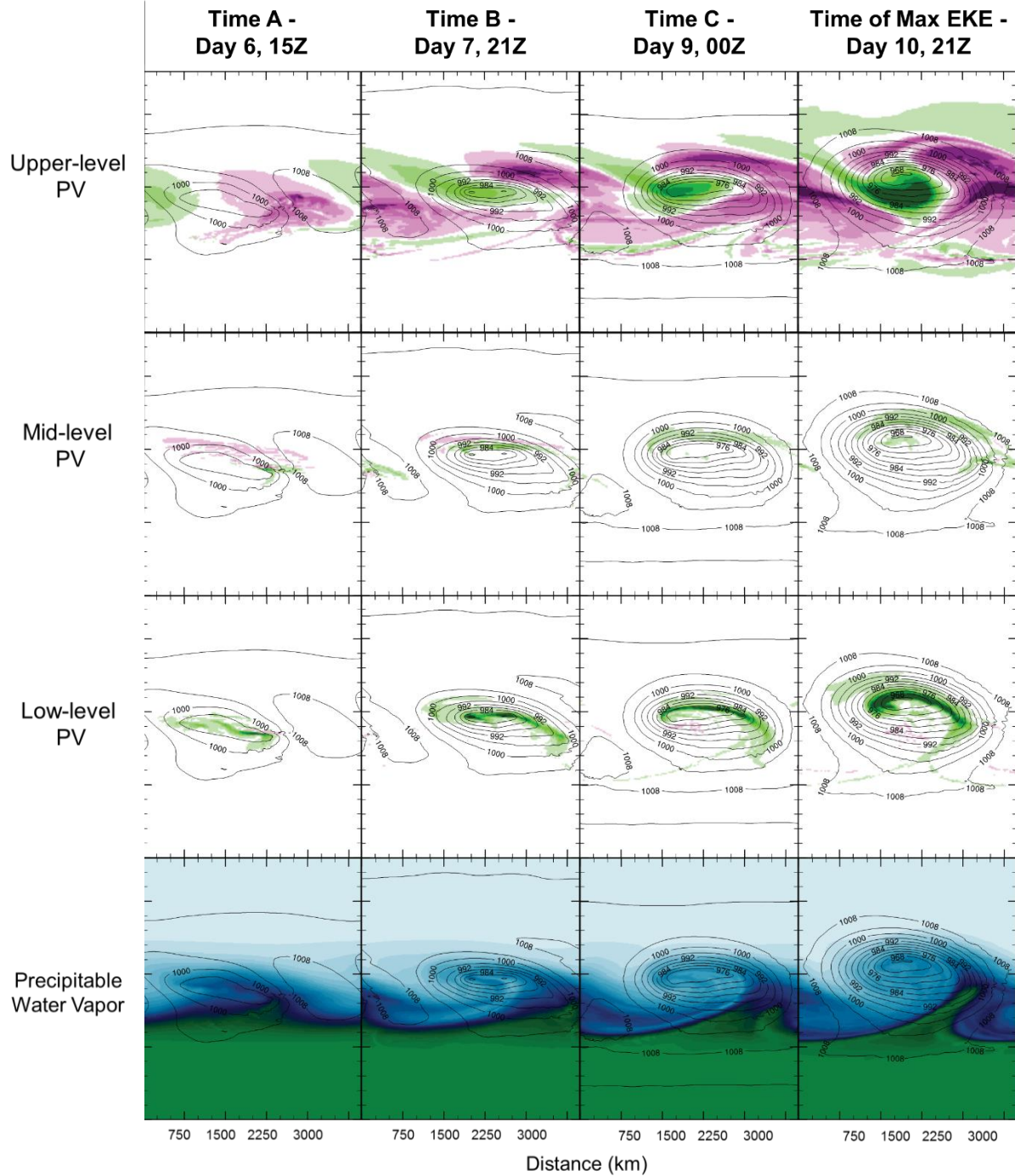


**Figure 4-10.** Four-panel PV anomaly and precipitable water vapor analysis, conducted at Times A, B, and C (indicated in Figure 4-9) and at the time of maximum EKE, with overlaid sea level pressure contours (hPa) for the 292 K bulk temperature case on a beta-plane.

## 308K Case



*Top Row:* 200-300 hPa Potential Vorticity Anomaly [calculated off of 0-12 hour average, PVU]  
*Second Row:* 600-700 hPa Potential Vorticity Anomaly, displayed only where relative humidity is greater than 80% [PVU]  
*Third Row:* 900-975 hPa Potential Vorticity Anomaly, displayed only where relative humidity is greater than 80% [PVU]  
*Fourth Row:* Precipitable Water Vapor [inches]

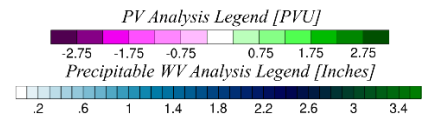


**Figure 4-11.** Four-panel PV anomaly and precipitable water vapor analysis, conducted at Times A, B, and C (indicated in Figure 4-9) and at the time of maximum EKE, with overlaid sea level pressure contours (hPa) for the 308 K bulk temperature case on a beta-plane.

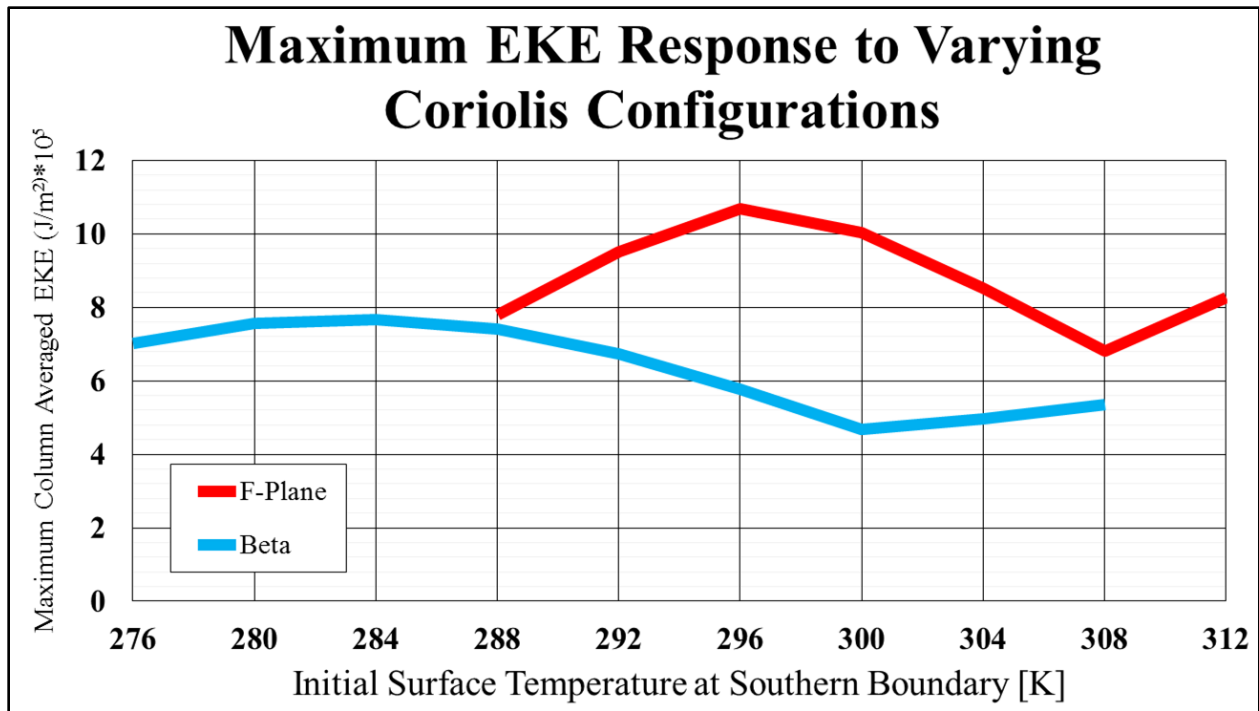


**Figure 4-12.** Maximum EKE response to changes in temperature/moisture content for both f-plane and beta-plane configurations. The jet amplitude factor is equal to 1.0 for all runs.

## Initialization Temperature Difference (K)

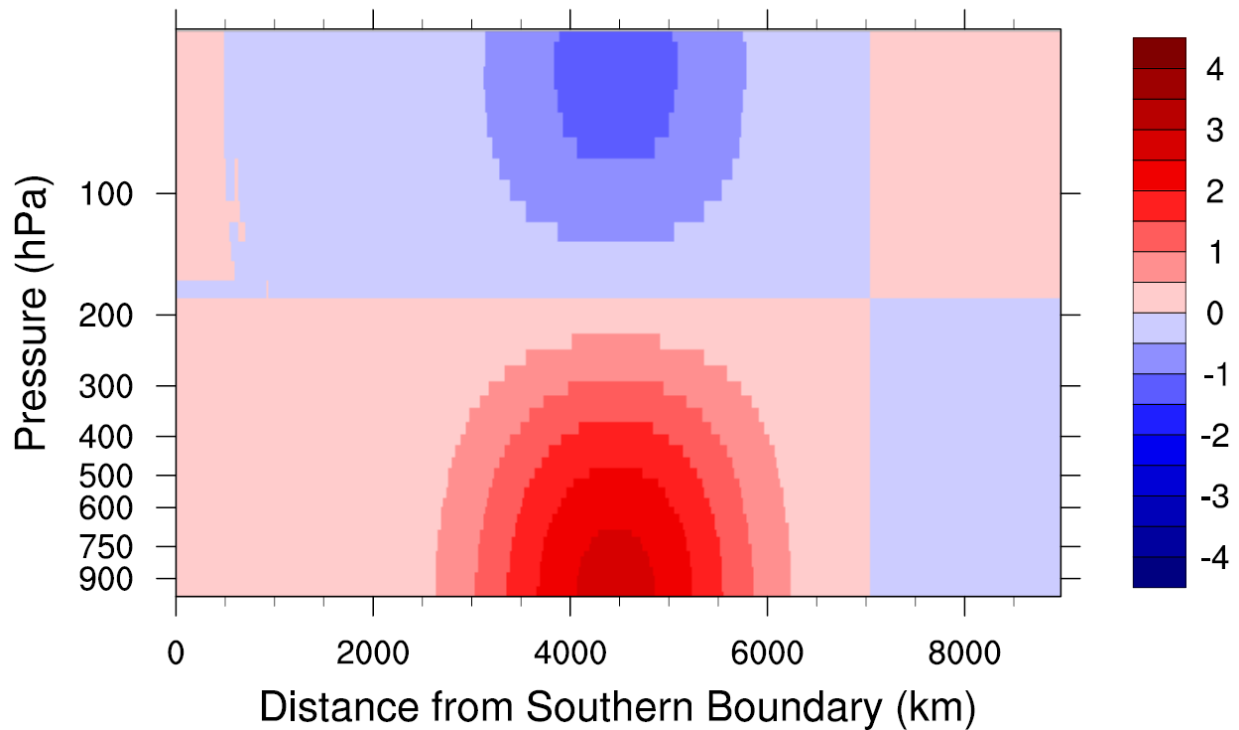


**Figure 4-13.** Cross-section of initial domain temperature differences (in K) between the beta-plane and  $f$ -plane configurations. Differences are taken for the control case at a bulk temperature of 300 K and jet amplitude factor of 1.0, with the southern boundary on left and northern boundary on the right of the figure. Red (blue) colors indicate that the beta-plane simulation is warmer (colder) than its  $f$ -plane analog.

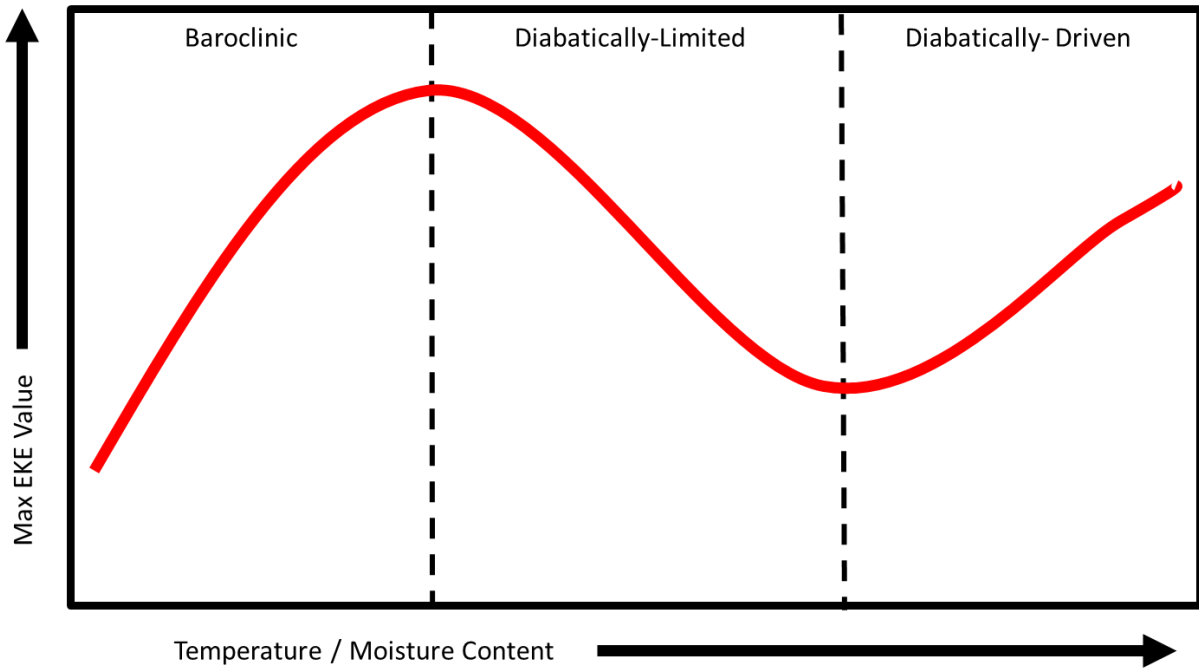


**Figure 4-14:** Sketch (not to scale) demonstrating the three regimes of extratropical cyclogenesis present in the parameter space, overlaid on a generalization of the maximum EKE response to temperature.

## **Chapter 5: The Impact of Radiative Processes on Extratropical Cyclones**

### ***5-1: Introduction***

In constructing the model configurations within the past two chapters, we expanded on previous idealized sensitivity literature, improving the realism of environmental perturbation mechanisms and considering simultaneous modification of both temperature and baroclinicity. Noting that virtually all of the current literature has neglected the impact of radiation on the baroclinic life cycle, we now advance our experiments by including radiative processes – bringing our model even closer to a full representation of the Earth’s climate system and providing an additional pathway for energy into and out of the system. However, the addition of radiative processes goes far beyond the simple inclusion of an external forcing onto the system. More crucial to the dynamical processes within ETCs is the path of the energy inside the system. Radiative absorption and emission by major and trace atmospheric gases along with countless cloud droplet interactions exerts a potentially tremendous dynamical influence.

Among all atmospheric constituents, radiative interactions with water vapor are some of the most important in the climate system. Water vapor was first recognized as a major atmospheric absorber of thermal radiation over 250 years ago (Tyndal, 1861), even though it makes up 1 – 4% of the atmosphere’s mass. From a climate context, continuum absorption of radiation within the 10- $\mu\text{m}$  window by water vapor is most crucial to understanding its impacts on the Earth’s radiative balance. Furthermore, an increase in atmospheric moisture capacity within a changing climate adds significant uncertainty. The water vapor feedback – a positive

feedback loop wherein the trapping of radiation by water vapor heats the planet, resulting in more atmospheric water vapor which traps even more heat – combines with the related cloud and lapse rate feedbacks to produce “most of the simulated climate feedback and most of its inter-model spread” (IPCC 2014). Therefore, for the fullest realization of future climates, radiative processes must be considered. Until now we have omitted them, building a solid foundation by understanding ETC sensitivity in non-radiative environments.

Establishing this foundation also allows our upcoming experiments to have dual utility: understanding not just ETC sensitivity in future climate conditions, but also evaluating ETC sensitivity to radiative processes – a field that has largely been neglected in current study. Some recent work has approached the subject, largely dealing with the cloud radiative effect on ETCs from an observational perspective. Work by Tselioudis and Konsta (2017) has identified the modification of shortwave and longwave radiative cloud effects with the poleward shift of high clouds in midlatitude storm tracks. This northward expansion is perhaps due also to the expansion of the Hadley cell (Tselioudis et al. 2016). Observational work by Polly and Rossow (2016) showed that the cloud radiative effect exerts a net cooling for all groups of the  $10^6$  ETCs they analyzed, with the cooling enhanced by greater cyclone depth. However, no modeling work seems to have considered radiative effects on ETCs from a sensitivity perspective.

Instead, we can look to the tropical cyclone community for some guidance on radiative effects in dynamical systems, especially with regards to cloud radiative forcing (CRF). In attempting to reduce the forecast error of hurricane forecasting, Fovell and Su (2007) considered microphysical and cumulus schemes within forecast models, finding that indeed, cloud processes have an effect on storm motion over as short a time period as 48 hours. This was extended by Fovell et al. (2009), which noted that the use of different microphysical schemes led to different

physical structures within tropical cyclones. Interestingly, these differences only appeared when CRF was enabled within the model, indicating that radiative impact on tropical cyclones is primarily through microphysical processes (Fovell et al. 2010). Physically, longwave absorption by the anvil leads to enhanced convective heating, which feeds back into the wind field (Bu et al. 2014). A fuller explanation of all these processes is covered in a review by Fovell et al. (2016) as well, but is omitted here, given the differences in large-scale dynamical forcing between ETCs and tropical cyclones.

With the configuration options of the WRF model and the flexibility of our modeling configuration, we aim to start discussion about the effects of radiative processes on ETCs by performing similar univariate and bivariate experiments to Chapter 4, now with radiative processes enabled. The specifics of the modeling configuration are outlined in Section 5-2, with the results of the univariate and bivariate experiments presented in Sections 5-3 and 5-4. Section 5-5 contains discussion of the dynamical features present within these experiments. Section 5-6 presents a suite of experiments designed to ease the transition between non-radiative and radiative configurations, allowing attribution of response variability. Finally, our findings are summarized in Section 5-7.

### ***5-2: Methods and Experiment Design***

As in previous chapters, we again utilize the Weather Research and Forecasting Model, Version 3.5.1, to create idealized sensitivity tests, the configuration of which is largely outlined in Chapter 2. For the experiments in this chapter, we use an identical beta-plane setup as in the previous chapter, with one key modification. Having explored ETC response in environments without radiative processes, we now enable both shortwave and longwave radiative processes.

For shortwave radiation, we use the MM5/Dudhia shortwave scheme (Dudhia 1989), which has a diurnal cycle and accounts for clear-air scattering, water vapor absorption, and cloud albedo/absorption. We opt to use settings within this scheme to emulate insolation levels typical for January, as frequency maxima for ETCs in the North Pacific, Great Lakes, and Eastern Seaboard occurs during the January – March timeframe (Colucci 1976; Eichler and Higgins 2006). For longwave radiation, we use the Rapid Radiative Transfer Model (RRTM) scheme, based on Mlawer et al. (1997), using the correlated- $k$  method and preset tables for longwave processes across 16 bands for interactions with water vapor, ozone, CO<sub>2</sub>, and accounting for cloud optical depth. By addition of these two schemes, we move our model configuration closer to reality, building on the foundation set in Chapters 3 and 4.

As in Chapters 3 and 4, we design our experiments for comparability with past results. Therefore we again plan three experiments as listed in Table 5-1. As before, the first two experiments are 6-simulation univariate experiments testing ETC sensitivity to bulk temperature and baroclinicity, with the final experiment being a 121-simulation bivariate test which utilizes simultaneous changes within the range of the univariate experiments.

The inclusion of radiative processes diverges from previous experiments in Chapters 3 and 4 by adding an energy pathway into the system. Confirming that the added insolation does not overwhelm environmental differences we wish to examine, Figure 5-1a presents differences in zonally averaged 700 hPa temperature between latitudes one-quarter and three-quarters of the way into the domain from the south. These differences are presented over the first 139 hours of the simulations in the univariate baroclinicity test. Even with radiation enabled, temperature differences due to variations in baroclinicity are consistent and represent the variation intended. Similarly, Figure 5-1b presents the full-domain averaged temperature for the first 139 hours of

the simulations in the univariate bulk temperature experiment. Once again, insolation and/or radiative cooling do not cause convergence of these runs. Satisfied that these simulations still represent the environmental modifications intended, we analyze the results of our sensitivity experiments.

### ***5-3: Univariate Sensitivity Results***

As in previous chapters, we first examine the strength of the ETCs from the moist univariate sensitivity experiments, with Figure 5-2 presenting the minimum SLP and EKE results of the moist univariate baroclinicity experiment. All ETCs reach peak strength in both metrics during the 14 day simulation period, except for the weakest run with a jet amplitude factor of 0.4. And, while in previous chapters, changes in domain baroclinicity have been shown to alter the peak strength of the SLP and EKE metrics for ETCs, the impact of radiation on ETC development stands out in Figure 5-2. Radiation appears to be an equalizer, especially with regards to EKE, where all ETCs with jet amplitude factors greater than 0.6 reach similar simulation-maximum EKE values between  $7-8 \times 10^5 \text{ J/m}^2$ . Minimum SLP is variable with sudden strengthening and deepening, although as in previous experiments, results towards the end of the timeline in these systems should be ignored due to unrealistic storm self-interaction. Although simulation-minimum SLP values are also relatively similar at approximately 950 hPa, this is often due to secondary cyclogenesis later in the simulation. If only the first phase of cyclogenesis is considered, baroclinicity is a controlling factor on simulation-minimum SLP, deepening with increasing values of the jet amplitude factor before leveling out in the most baroclinic domains. While the addition of radiative processes muddles the relationship between domain baroclinicity and ETC strength, a signal of more rapid ETC genesis and development is

still present. Within more baroclinic domains, cyclogenesis occurs sooner, shrinking to as soon as 4 days in the most baroclinic domain. Deepening rates between cyclogenesis and maturity are also greater, with the ETC in the most baroclinic domain deepening 50 hPa in 72 hours, compared to with 50 hPa in 90 hours in the control simulation with a jet amplitude factor of 1.0.

Following the univariate baroclinicity experiment, we again consider the effect of increasing temperature and moisture on ETC development. In Chapters 3 and 4, these factors were demonstrated to have an effect on the dynamical environment through moist processes such as convection. With radiation now included, Figure 5-3 displays the results of both strength metrics for the univariate bulk temperature experiment. Before analyzing the entire experiment, the early EKE plateau observed between 30 and approximately 120 hours in the warmer simulations (greater than 296 K) should be addressed. In the warmest simulations, initial convective available potential energy (CAPE) values in the southern portion of the domain are high, exceeding 3000 J/kg, as demonstrated in Figure 5-4, a zonally-averaged initial sounding of the 304 K simulation, one-quarter of the way into the domain (from the south). Within this sounding, plotted on a Skew-T Log-P diagram, the black line indicates the environmental temperature and blue line indicates the environmental dewpoint. The red dashed line is the theoretical temperature of a parcel raised from the surface and allowed to freely convect, and indicates the boundary of integration for CAPE, calculated as the area between the black and red lines. This convectively primed environment adjusts towards radiative-convective equilibrium in the southern (tropical) portion of the domain early in the simulation, and the brief, local circulations induced cause an early plateau in EKE between 30 – 120 hours. Considering its absence in counterpart simulations without radiative processes, this adjustment might seem artificial. However, as previously mentioned, the addition of radiation adds energy pathways into

and out of the system, and radiative interactions with atmospheric constituents have a significant effect on the environment (covered in more detail in Section 5-6). Furthermore, it represents the natural tendency of the tropical atmosphere towards neutral stability. This is especially noticeable in the warmest runs, wherein the temperature profile follows the moist adiabatic lapse rate in a layer from the surface to 700 hPa between days 2-5. Most crucially, there are no direct effects on development of the ETC later in the simulation. Post-convection equilibrium states still represent similar temperature offsets, and the warmest environments still contain more moisture, a result of the Clausius-Clapeyron relationship.

Consideration of the initial convective burst aside, the ETCs within the univariate bulk temperature experiment demonstrate significant response variability, especially when compared to counterparts without radiative processes. Assembling a coherent pattern from simulation-maximum EKE values is difficult at best, with the relationship to temperature flipping 3 separate times - between 288 – 292 K, 300 – 304 K, and 304 – 308 K. Curiously, the 6 simulations seem to bunch into 3 separate response pairs. Consideration of simulation-minimum SLP values also fails to provide clarification, as the warmest run (308 K) is strongest, while also one of the weakest ETCs using simulation-maximum EKE. Using only 6 simulations, it is difficult to draw conclusions even of a qualitative nature.

Therefore, another version of the univariate bulk temperature sensitivity experiment is run, halving the steps to 2K between 288 K and 308 K. The resulting 11-run sensitivity test spans the same parameter space with more data points. The minimum SLP and average column-summed EKE metrics for this improved bulk temperature sensitivity test are presented in Figure 5-5. While cluttered, Figure 5-5 demonstrates that these 5 additional simulations allow qualitative conclusions to be drawn about moist interactions in a radiative environment. There is

a bifurcation of development in minimum SLP, divided by temperature. Generally, ETCs in cooler domains develop sooner than their warmer counterparts, with an 18 hour offset between the two sets of ETCs. However, cooler ETCs deepen slower, and so the development gap is closed approximately 50 hours later. Second, additional univariate bulk temperature simulations clarify EKE results. Again, the warmest runs have the highest rates of development. In addition, consideration of simulation-maximum EKE demonstrates a non-monotonicity similar to experiments without radiative processes – as demonstrated in Figure 5-6, which compares simulation-maximum EKE values for the univariate bulk temperature experiments with and without radiative processes. Both experiments exhibit decreases in simulation-maximum EKE with warming from 288 K – 300 K, followed by a plateauing effect/slight increase at temperatures warmer than 300 K, although the addition of radiative processes does obfuscate the response slightly. Regardless, it is clear that improved parameter space coverage shows the apparent clustering behavior of the 6-run experiment to be coincidental, not a product of sudden regime shift.

#### ***5-4: Bivariate Sensitivity Results***

As in Chapters 3 and 4, we acknowledge the incomplete nature of employing only univariate tests to explore the sensitivity of ETCs in future climatic conditions. Therefore, we again conduct bivariate experiments, simultaneously perturbing both bulk temperature and domain baroclinicity. As before, bulk temperature is stepped by 2 K from 288 K – 308 K, and the jet amplitude factor is adjusted from 0.8 to 1.2 in steps of 0.04 to create a 121-simulation bivariate experiment. This design creates an environment wherein the feedbacks and interplay between environmental characteristics is explored.

For consistency with the univariate experiments, we first revisit our two main strength metrics, simulation-minimum SLP and simulation-maximum EKE. Figure 5-7 displays the results of the simulation-minimum SLP metric within the bivariate space, with jet amplitude factor increasing along the x-axis, and bulk temperature increasing along the y-axis. In comparison to the bivariate results for the corresponding experiment without radiation (Fig. 4-5), the response is considerably noisier. However, there is one qualitative conclusion that can be made. Increases in domain baroclinicity generally yield stronger ETCs, a conclusion also reached in the corresponding non-radiation experiment. Deepening of approximately 10 hPa is present as the jet amplitude factor is increased from 0.8 to 1.2. Conversely, there is no discernable signal between simulation-minimum SLP and increasing temperature/moisture, reinforcing the dominance of baroclinicity in controlling the minimum SLP of an ETC.

While baroclinicity is the dominant factor in determining the minimum SLP of an ETC, the bivariate results for the simulation-maximum EKE in Figure 5-8 demonstrate that baroclinicity does not dominate all measures of ETC strength. Most pronounced in Figure 5-8 is an EKE maximum centered at the coldest temperatures with domain baroclinicity slightly above that of the default value (around a jet amplitude factor of 1.1). From here, the simulation-maximum value of EKE decreases along both axes – a sign of interplay between environmental characteristics. The decrease is especially rapid with regards to temperature, with simulation-maximum EKE values declining 20% after an increase of only 6 K. As in Chapter 3, we can compare the sensitivity of simulation-maximum EKE to both variables, as the 20% decrease in simulation-maximum EKE from a 6 K increase in temperature can be replicated with a 16% decrease in jet amplitude factor (from 1.1 to 0.92). From a qualitative point of view, comparison with the corresponding non-radiation experiment (Fig. 4-6) confirms that the response functions

between the two experiments are generally similar (as also demonstrated in Fig. 5-6 for univariate experiments) with a slight variation, as the maximum value of simulation-maximum EKE shifts to slightly weaker baroclinicities with radiation enabled. Rapid decreases with increasing temperature are present and a generally noisy response regime exists in the top half of the figure, above bulk temperatures of approximately 298 – 300 K, a sign of convection’s increasing role in warmer/moister environments.

Aware of the increasing role of convection, we also assess how precipitation amounts vary with increasing temperature and baroclinicity. Figure 5-9 presents three precipitation metrics, averaged over all times across the entire domain, beginning with convective precipitation (Fig. 5-9a) and non-convective precipitation (Fig. 5-9b). As expected, precipitation amounts increase in both modes with increasing temperature – a natural outcome of warmer atmospheres containing more water vapor at identical relative humidity values. In fact, convective precipitation correlates solely with bulk temperature through much of the parameter space. Only at the warmest temperatures does baroclinicity begin to play a factor, when convective precipitation decreases in the least baroclinic environments. Similarly, non-convective precipitation is generally dictated by the bulk temperature (and thus moisture content) of the simulation, although baroclinicity plays a role at cooler temperatures when ETCs rely on synoptic-scale drivers of precipitation. In these cases, convection only accounts for approximately one-third of the total precipitation, as demonstrated by Figure 5-9c, the convective percentage of precipitation. In contrast, convection accounts for more than two-thirds of all precipitation in warmest domains, despite large amounts of non-convective precipitation.

These percentages come with a caveat, however. Recalling the early EKE plateauing behavior in the univariate experiments, we can infer that there are non-ETC sources of

convective precipitation in the warmest simulations, specifically within the adjustment towards radiative-convective equilibrium. Therefore, we restrict averaging to highlight the mid-latitudes (specifically from 25 – 72°N, between the 100<sup>th</sup> and 300<sup>th</sup> row of grid points within the model) with results presented in Figure 5-10. The impact of these restrictions is evident in Figure 5-10a, as convective precipitation amounts are significantly less than when averaging is conducted over the full domain. As expected, the reverse occurs for non-convective precipitation presented in Figure 5-10b, as the average increases with spatial restriction. And while in both cases, the general response is similar regardless of averaging, domain restriction allows greater accuracy in estimating the convective fraction of precipitation (presented in Figure 5-10c). Indeed, the pattern does change here, as a co-dependence on baroclinicity is revealed (similar to the non-radiation cases in Fig. 4-8c). Percentages are lower, ranging from 20% to just over 50% in the coolest and warmest simulations, respectively. In comparison, the full domain-averaged percentages ranged between 33 – 75%, demonstrating that more realistic estimates of ETC precipitation when radiative processes are enabled requires the addition of averaging restrictions.

### ***5-5: Discussion***

While the addition of radiative processes brings our idealized simulations closer to reality, they also complicate understanding by providing additional energy pathways in and out of the system. These complications can be used to test the continued applicability of the three-regime model of ETC development proposed in Chapter 4. Therefore, we begin with understanding convection's impact in the colder simulations from the univariate bulk temperature sensitivity test. Figure 5-11 presents longitudinally-averaged Skew-T soundings one-quarter of the way into the domain (from the south), representative of the environment

advected into the ETC through the warm conveyor belt. These soundings are provided for the 288 K simulation (Fig. 5-11a) and the 296 K simulation (Fig. 5-11b), at two times: initialization (dashed lines) and 5 days into the simulation, just before cyclogenesis (solid lines). For the 288 K simulation, cooling is visible throughout the depth of the troposphere, along with a slight destabilization after 5 days. Temperatures decrease 4-5 K in the 250-500 hPa layer, while only decreasing 2-3 K near the surface, resulting in an increased lapse rate and development of minimal CAPE, which increases from 0 J/kg to 177 J/kg. The Showalter index, a difference between the 500 hPa environmental temperature and the temperature of a parcel adiabatically lifted from 850 hPa to 500 hPa, decreases from 4 to 2. While a decrease in the Showalter Index indicates the development of an environment more conducive to convection, the presence of strong lifting is still required to initiate convection (strong convection in the Showalter index is indicated by negative values). The cooling patterns of the mid-troposphere also confirm the lack of significant convection. Cooling from 700 – 250 hPa is paired with dewpoints falling 2-3K, indicating a general radiative cooling of the column, rather than cooling paired with convective maintenance of dewpoints.

In contrast, soundings from the 296 K simulation (presented in Fig. 5-11b) demonstrate the influence of convection in runs even slightly warmer than the minimum in the univariate bulk temperature experiment. As in the 288 K simulation, there is cooling throughout the depth of the troposphere. Crucially, these temperatures do not fall as far, however, with decreases of only 1-3 K from 400 hPa down to the surface – a product of convective latent heat release within the column. And, unlike the 288 K simulation, tropospheric cooling is paired with maintenance of the dewpoints throughout the column between 400 hPa and the surface, indicating convective maintenance of moisture. Further evidence of convective action is visible in the radiative cooling

and entrainment in the convective anvil above the equilibrium level of the initial sounding at approximately 340 hPa. Inertia from convective updrafts carries parcels into this region, where they mix with drier air and cool. Continued convection would be expected to raise the equilibrium level by supplying further moisture and latent heat release, and indeed, the equilibrium level rises to approximately 240 hPa by day 5. CAPE also grows approximately 75% from 594 J/kg at initiation to 1034 J/kg on Day 5. Unlike the 288 K simulation, it is clear that convective processes play a role in the ETC dynamical environment of the 296 K simulation. While similar to the transition between the baroclinic and diabatically-limited regimes first presented in Chapter 4, the potential role of convection has also been increased by mid-tropospheric radiative cooling. The resulting destabilization increases CAPE values in these simulations compared to the corresponding simulations without radiation. While both simulations are initialized with identical soundings, the addition of radiation increases CAPE by 28% (from 808 J/kg to 1034 J/kg).

The addition of radiative processes into our modeling setup also has an effect on the morphology of ETCs at maturity, which as discussed in Chapter 1, can be interpreted through several conceptual models. The oldest of these is the Norwegian model developed by Bjerknes (1919) and later Bjerknes and Solberg (1922). Most well-known in recent work is the Shapiro-Keyser model (Shapiro and Keyser 1990). These models simplify classification of frontal systems to better understand their dynamics. Factors leading to structural differences have been explored by Schultz et al. (1998), who observed that ETCs in confluent flow tend towards the Norwegian model, while ETCs in diffluent flow tend towards the Shapiro-Keyser model. With this in mind, we consider the morphology of the ETCs in our univariate bulk temperature experiment. To allow for intra-experiment comparison as well as comparison to the previous

chapter's results without radiative processes, we perform a PV anomaly analysis of the 292 K and 308 K simulations, with Figure 5-12 presenting the results for the 292 K simulation. As in Chapter 4, we break down the analysis into 3 layers: upper-level PV (200 – 300 hPa), mid-level PV (600 – 700 hPa), and low-level PV (900 – 975 hPa), chosen to provide a comprehensive picture of both synoptic-scale processes and convection. Finally, precipitable water vapor (PWV) is presented in the bottom row, with sea level pressure contours overlaid on all plots for reference. This analysis is performed at three times, chosen to represent ETC development, indicated at the top of Figure 5-12.

Developmental analysis of the ETC in the 292 K simulation begins at Time A, 150 hours into the simulation. An upper-level PV dipole aids strengthening of the ETC, with positive and negative PV anomalies to the west and east of the ETC center, respectively. The SLP minimum between is slightly elongated, with the warm conveyor belt (WCB, visible in the PWV analysis) providing the warm, moist air necessary to maintain the baroclinic lifecycle. Note, however, the skewed orientation of the WCB in this simulation, as compared to the 292 K simulation without radiation in Chapter 4 (Fig. 4-10). Here, the WCB is stretched in a southwest to northeast orientation, rather than the north-south orientation of the no radiation counterpart. 24 hours later, at time B, the WCB in Fig 5-12 is also oriented north-south, but the SLP minimum is now well to the west of the WCB and corresponding PV generation by lifting of the convectively primed inflow. In addition, the upper-level PV anomaly is encroaching on the SLP minimum, stacking the original ETC center and leading to cyclolysis at the western edge of the SLP minimum. However, this does not spell the end of the entire ETC, as at Time C (9 hours later), a new SLP minimum, well situated with regards to the upper-level forcing, forms at the triple point (the intersection of the T-shaped positive PV anomaly visible in low-level analysis at Time C of Fig.

5-12). At mid-levels, remnants of the circulation and vorticity around the original center are still noticeable, and the lower-level PV positive anomaly has taken on a T-shape, mirroring the WCB before splitting east and west. This shape is characteristic of ETCs in the Shapiro-Keyser model, where the cold front travels along the warm front, leaving the SLP minimum in its wake. Interestingly, this structure stands in stark contrast to the Norwegian-style structure presented in Figure 4-10, the same case without radiative processes. By running an identical simulation with radiative processes enabled, the resulting ETC can be classified under a different conceptual model, for reasons that still require further investigation.

Finally, we turn to the other end of the univariate bulk sensitivity test to examine how radiative processes affect the warmest run in the parameter space, demonstrated in previous chapters to exhibit non-canonical development. To this end, Figure 5-13 presents a PV anomaly and PWV analysis of the 308 K simulation. As before, PV anomalies are divided into the same layers as in the 292 K PV anomaly analysis, and the last row of the figure presents the simultaneous PWV analysis. This analysis is repeated at 4 different times, selected to represent development to maturity of the ETC, and listed at the top of Figure 5-13. At Time A, in the leftmost column of the figure, the dynamical environment of the warmest simulation is substantially different than the 292 K simulation, just 150 hours in (the same time as Time A in Fig. 5-12). The upper-level PV anomaly lacks a dipole structure around the SLP minimum, and there is evidence of significant convective modification of the environment – an array of incoherent positive and negative anomalies at mid-levels. At lower levels, there are two SLP minima developing at either end of a broader V-shaped SLP minimum. Upper-level synoptic conditions favor strengthening of the eastern SLP minimum, and as is visible in the PWV product, the WCB favors the eastern SLP minimum, transporting conditionally stable air primed

for convection, as demonstrated in Figure 5-14, a longitudinally-averaged sounding from the inflow region. CAPE values greater than 3700 J/kg are paired with a low LFC (level of free convection, above which parcels can rise unabated) of 949 hPa, indicative of a prime convective environment. In addition, there is significant precipitable water content (visible in the PWV product in bright green) at the base of the V-shaped SLP minimum.

The extreme CAPE values and instability in the inflow parcels is released immediately upon lifting in the WCB, and by Time B, just 15 hours later, a diabatic Rossby vortex has formed, as previously seen in Chapters 3 and 4. A new SLP minimum forms south of the original two, and positive PV anomalies associated with intense convection at the new minimum are visible at mid-levels at Time B in Figure 5-13. Low-level PV associated with the strengthening low-level vorticity and circulation of the DRV are visible as well, as all three SLP minima exhibit low-level, positive PV anomaly maxima. However, this new circulation is also in an excellent synoptic environment to undergo bombogenesis, a central pressure fall of greater than 1 bergeron (defined as  $24 * \left( \frac{\sin(\varphi)}{\sin(60^\circ)} \right) hPa$ ) in 24 hours (Sanders and Gyakum, 1980), where  $\varphi$  represents the latitude of the cyclone center. The WCB continues to provide warm, moist air, while the upper-level PV gradient is amplified by negative PV anomalies aloft due to convection along the trajectory of the previous WCB. Therefore, by Time C (15 hours later), the DRV deepens 24 hPa, well beyond the minimum deepening rate required for bombogenesis classification. It is the dominant SLP minimum in the domain, with a clearly defined WCB trajectory directly into the center of circulation. PV anomaly analysis shows impressive positive anomalies around the SLP minimum at both the low- and mid-levels of the atmosphere, and the DRV still sits in the steepest part of the PV gradient at upper-levels – an ideal synoptic environment for further deepening. Thus, the DRV merges with existing anomalies around the

old SLP minimum and transitions into a full-fledged ETC, drawing on the baroclinicity created by such tight circulation to sustain deepening to maturity, presented at Time D, the time of maximum EKE. By this time, the ETC has deepened another 20 hPa to a minimum SLP of approximately 944 hPa. A tight spiral of positive PV anomalies at the lowest levels indicates impressive low-level vorticity, continuing even into the mid-levels, where the center of the ETC is still well marked. Note that at this point, the initial DRV has transitioned into an ETC, as the strong supply of moisture from the WCB is well to the east, leading to reduced convection in and around the ETC center. While the evolutionary path of the ETC in this 308 K simulation is rather convoluted, a DRV still plays a large role early in the developmental timeline, similar to the warmest runs in the corresponding runs without radiative processes. Enabling radiation makes the DRV more intense and significant in the development process, placing the warmest end of the univariate bulk temperature test within the diabatically-driven regime of ETCs.

### ***5-6: Understanding the Root of Radiative Effects***

While all of the univariate bulk temperature experiments performed in Chapters 3-5 have demonstrated some variation on the three regimes of ETC cyclogenesis and development, the most obvious discontinuity in response occurs with the addition of radiative effects into the model. Unlike the transition between  $f$ -plane and beta-plane models, the addition of radiative processes encompasses numerous atmospheric interactions. Radiative processes include both insolation and emitted longwave radiation, with further complexity added from interactions with non-water vapor gases (e.g., carbon dioxide and ozone), water vapor, cloud-sized and precipitation-sized particles (both liquid and ice). Therefore, attempting to understand the increase in response complexity by simply comparing runs with and without radiative processes

is extraordinarily difficult. This may be the reason there has been little work done to date focusing on the effect of radiative processes on ETCs and extratropical cyclogenesis.

The complexity of this situation can be alleviated within the numerical modelling framework. Just as “non-physical” suites of simulations with no radiative processes are possible, we can selectively disable radiative interactions with certain atmospheric constituents, reducing the gap between suites of simulations. Following this approach, WRF is modified to produce two “semi-radiative” versions of the univariate bulk temperature experiment. The first of these follows work done by Fovell et al. (2010, 2014), who found that the interaction of microphysics and radiative processes plays a crucial role in determining the structure and path of modeled tropical cyclones, indicating that cloud radiative forcing (CRF) mechanisms are the primary conduits for radiative impact in these systems. Following this line, our first semi-radiative experiment removes cloud radiative forcing from the model, rendering liquid water and ice invisible to both shortwave and longwave radiation. For ease of reference, this experiment is termed the “No CRF” experiment. Our second semi-radiative experiment goes one step further to bridge the gap between the No CRF experiment and experiments without radiation. For this experiment, the WRF code is further modified to render all water vapor in the atmosphere invisible to shortwave and longwave radiation. In this “No Vapor” experiment, the only radiative interactions with the idealized environment are at the surface and non-water vapor gas-phase interactions within the atmosphere.

In adding these two semi-radiative experiments, we compile a four-suite sensitivity experiment that can pinpoint the class of radiative processes with the largest effect on ETCs. Figure 5-15 presents the strength metrics for all 4 suites of simulations in this continuum, beginning with the full radiative experiment (Fig. 5-15a), the No CRF experiment (Fig. 5-15b),

the No Vapor experiment (Fig. 5-15c), and the No Radiation experiment (Fig. 5-15d). When the cloud radiative forcing is removed between Figures 5-15a and 5-15b, there is a clear effect on the response of the experiment, with the 308 K simulation now developing to full strength soonest, rather than exhibiting the DRV-induced delay present in the full radiative experiment. In addition, the developmental timelines of the coldest ETCs are delayed. Qualitatively speaking, however, responses generally are similar between the No CRF and full radiative experiments, indicating that unlike in tropical cyclones, the cloud radiative effect does not play a dominant role in shaping ETC strength and characteristics. Instead, a further comparison from the No CRF experiment in Figure 5-15b to the No Vapor experiment presented in Figure 5-15c demonstrates that the interactions of radiative processes with water vapor are the dominant factor in the response shift between experiments with radiative processes enabled and disabled. With vapor interactions disabled, the strength metrics closely reflect the results of the same experiment without any radiative processes (Fig. 5-15d). While determining the exact mechanism by which water vapor exerts such a strong effect on extratropical cyclogenesis requires further work beyond this dissertation, it is likely that the cause is related to absorption and emission in the infrared spectrum, where water vapor is an important atmospheric constituent.

While it is clear that atmospheric water vapor serves as the most important link between radiative processes and ETC cyclogenesis/development, it should be noted that there are still differences between the No Vapor experiment and the No Radiation experiment. These differences include developmental delays in cooler simulations, an earlier EKE increase in warmer simulations, and the disappearance of a clear two-stage strengthening in the warmest runs of the experiment. To pinpoint this final piece of the puzzle, soundings from the control 300 K simulation in both experiments are presented in Figure 5-16, with the No Vapor sounding

presented in Figure 5-16a, and the No Radiation sounding presented in Figure 5-16b. Both simulations are zonally averaged at a latitude representative of the inflow region, one quarter of the way into the domain (from the south). While similar, these soundings have two crucial differences that expose radiative influence even when water in all forms is invisible to radiation. First, the addition of radiation leads to a moistening of the lowest levels, as evidenced by the close proximity of the dewpoint and temperature at lower levels – a change likely due to surface interactions with radiation. However, surface processes cannot explain the general cooling of the troposphere in the No Vapor case, where gas-phase interactions with radiation are the likely culprit, as all other atmospheric constituents are invisible to incoming and outgoing radiation. Taken as a whole, these four experiments demonstrate that simply activating the radiative processes without including interactions is not enough to cause dramatic response change. The key is radiative interactions with water, primarily in its vapor state, that has the dramatic effect on response. The interactions of radiation with water in liquid and solid forms also exert a secondary influence on ETC development, but are not the primary driver, unlike tropical cyclones.

### ***5-7: Conclusions***

To bring our idealized experiments closer to reality, radiative processes were activated within the model. These processes included diurnal insolation, atmospheric emission and reflection, as well as interaction with numerous atmospheric constituents. As before, we performed three primary experiments: a univariate bulk temperature experiment, a univariate baroclinicity experiment, and a bivariate experiment. In understanding the results of the strength metrics from these experiments, the early action of convection working to equilibrate the

southern portion of the domain must be noted, mimicking similar natural convection in tropical regions. Examination of the strength metrics for both univariate tests reveals a dramatically different set of response functions when compared to the non-radiation results in Chapter 4. ETCs in the univariate baroclinicity tests are all similar in strength, although differences in the developmental timeline are still clearly visible.

For better understanding of the univariate bulk temperature experiment, an additional 5 runs were added, halving the step size between runs to 2 K. This additional coverage showed the pairing of the original 6-run experiment to be a coincidental result of run selection, and while the addition of radiation did obfuscate results, a similar response in simulation-maximum EKE was found between the corresponding experiments with and without radiative processes enabled. Expansion of these experiments into the bivariate parameter space found further noise from radiative processes; however, clear trends were observed in simulation-maximum EKE for colder runs, with a non-monotonic response present once again. After filtering the results with consideration for the initial convective adjustment, increases in non-convective and convective precipitation were found with increases in temperature. Non-convective precipitation also increased with increasing domain baroclinicity, as in the corresponding experiment without radiative processes. In partitioning the precipitation, it was found that ETCs in the warmest and most weakly baroclinic environments contained the highest fraction of convective precipitation, exceeding one-half of the total precipitation.

Further dynamical analysis of the simulations within the univariate bulk temperature experiment revealed that along the colder end of the experiment, ETCs underwent cyclical cyclogenesis, with new SLP minima growing from the triple point of the parent low pressure center. ETCs also favored a morphology that more closely resembled the Shapiro-Keyser

conceptual model, rather than Norwegian model reflected in the morphologies of experiments without radiation – the reasons for which require further investigation into exactly how radiative processes affect the flow regimes in these experiments. In the warmest case, DRV generation was once again found to be an important part of ETC genesis, with multiple minima forming before a resultant DRV underwent bombogenesis and merged into the ETC at-large. Such development processes indicate that the warmest portions of the parameter space, even when radiative processes are activated, are still in the diabatically-driven regime of ETC development.

Finally, the jump between simulations with and without radiative processes was smoothed by the addition of two semi-radiative runs, wherein various atmospheric species of water were made invisible to all forms of radiation. This further subdivision of radiative influences isolated the effects of cloud radiative forcing, water vapor interactions, and gas-phase interactions within ETCs. Unlike tropical cyclones, which have been shown to be highly influenced by cloud radiative forcing, ETCs in this experiment were most impacted by the interaction of radiation and water vapor, likely in the infrared spectrum. The exact mechanisms by which this affects the dynamical environment are yet unknown, and require further investigation, especially given the current deficiencies in understanding the effects of radiation on ETCs.

Experiment #	Description	# of Runs	Southern Boundary Surface Initialization Temperatures (K)	Jet Amplitude Factors
1	Univariate Baroclinicity Test	6	[300]	[0.4, 0.6, 0.8, 1.0, 1.2, 1.4]
2	Univariate Bulk Temperature Test	6	[288, 292, 296, 300, 304, 308]	[1.0]
3	Bivariate Test	121	[288, 290, 292, 294, 296, 298, 300, 302, 304, 308]	[0.8, 0.84, 0.88, 0.92, 0.96, 1.00, 1.04, 1.08, 1.12, 1.16, 1.20]

**Table 5-1.** Radiation experiment descriptions.

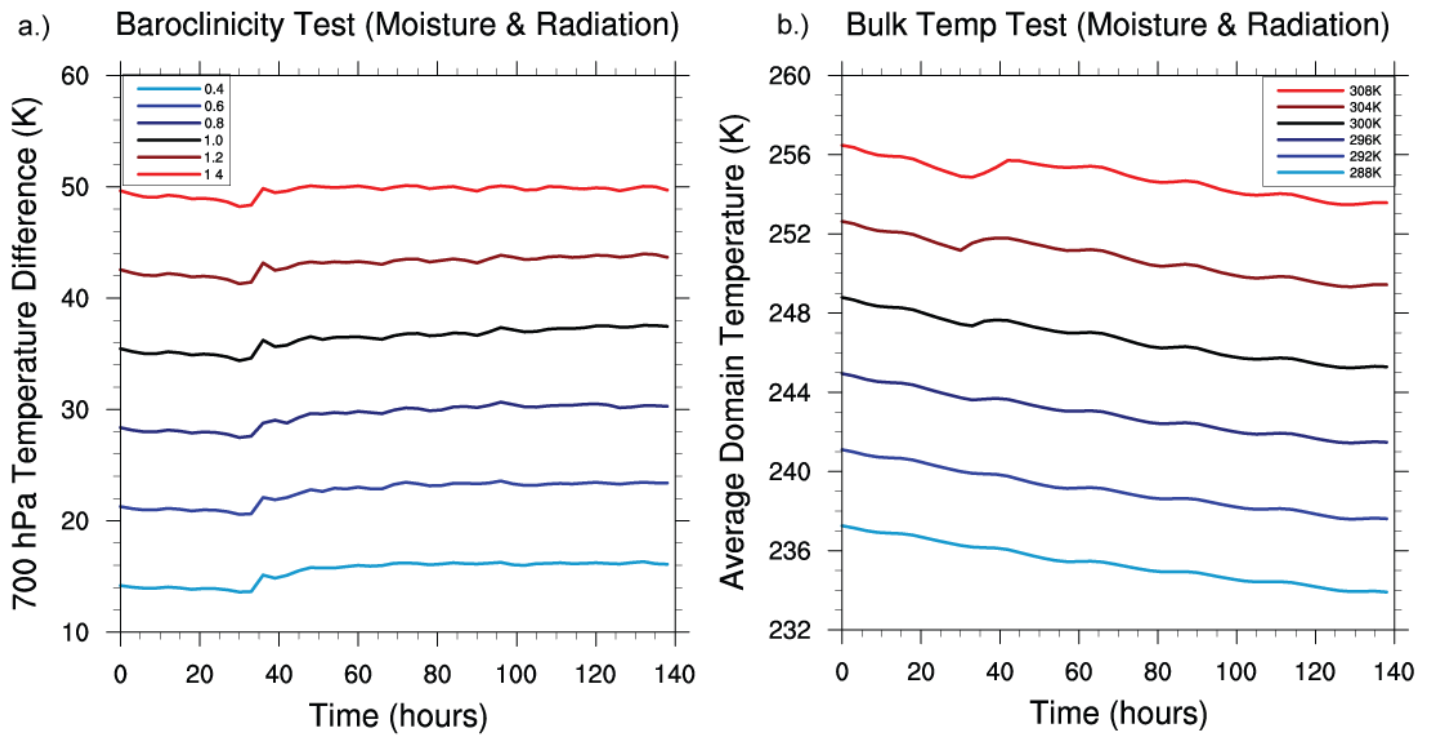


**Figure 5-1.** Figure 5-1a, left: Difference of zonally-averaged 700 hPa temperatures (K) between one-quarter and three-quarters of the way into the domain (from the south) for the univariate baroclinicity sensitivity test. Figure 5-1b, right: Full-domain averaged temperatures (K) for the univariate bulk temperature sensitivity test.

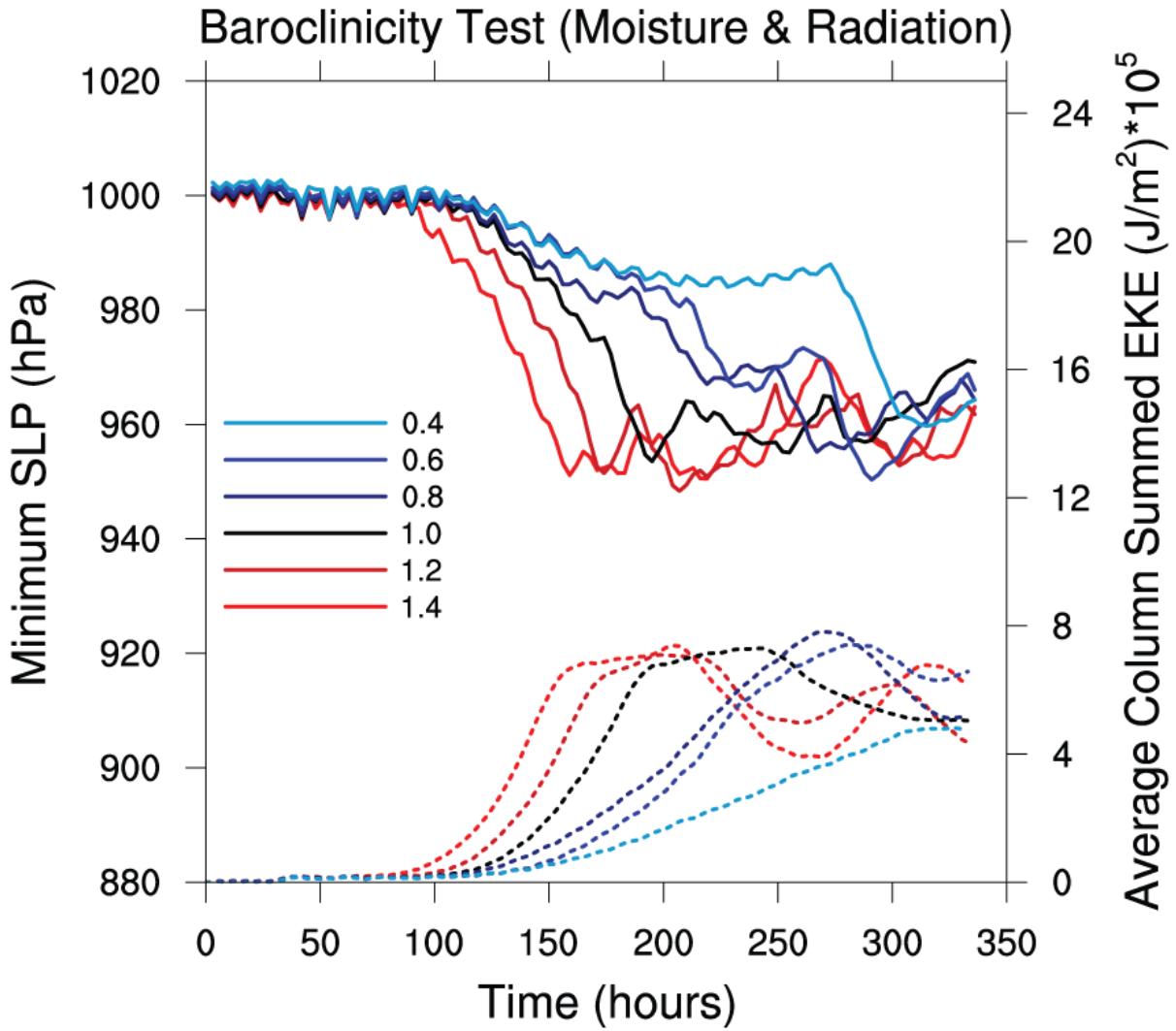


**Figure 5-2.** Average column-summed EKE (dashed lines) and minimum SLP (solid lines) for the 6 runs spanning the moist baroclinicity univariate test on a beta-plane with radiative processes enabled.

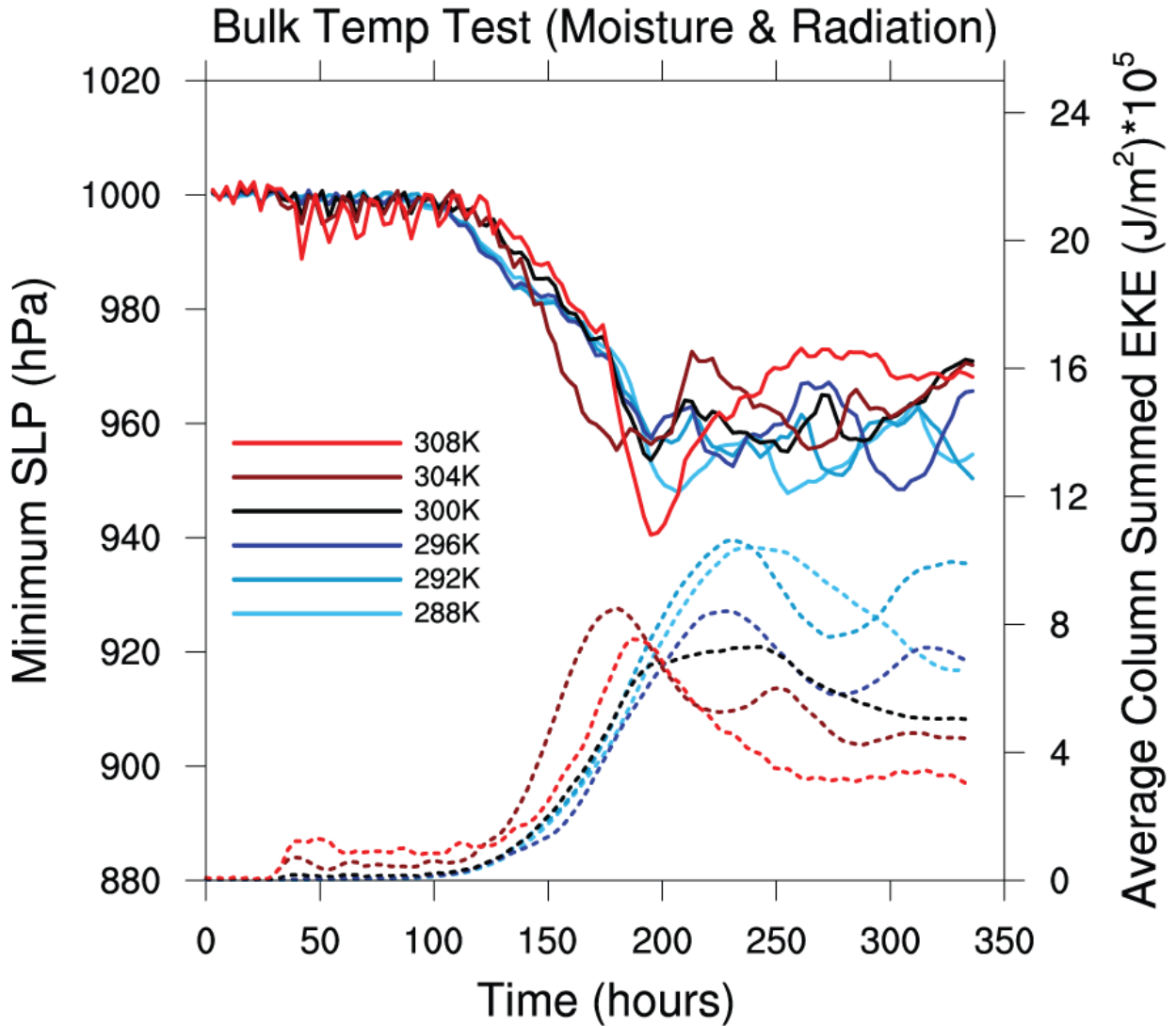


**Figure 5-3.** Average column-summed EKE (dashed lines) and minimum SLP (solid lines) for the 6 runs spanning the moist bulk temperature univariate test on a beta-plane with radiative processes enabled.

## Initial Sounding, Bulk Temperature Case = 304 K

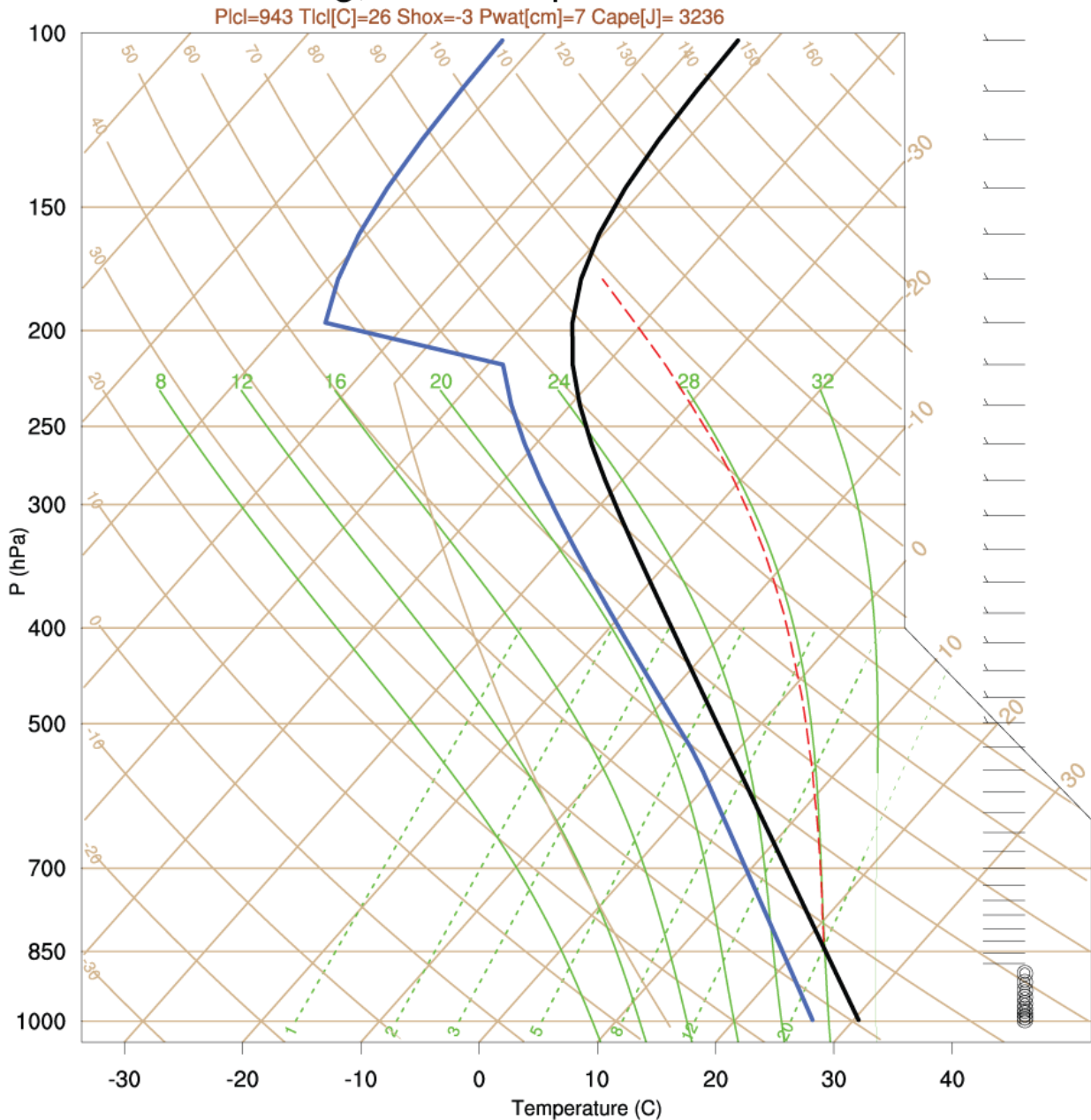


**Figure 5-4.** Longitudinally-averaged atmospheric profile taken one-quarter of the way into the domain (from the south) at initialization of the 304 K simulation on a beta-plane with radiative processes enabled. Within this sounding, plotted on a Skew-T Log-P diagram, the black line indicates the environmental temperature and blue line indicates the environmental dewpoint. The red dashed line is the theoretical temperature of a parcel raised from the surface and allowed to freely convect, and indicates the boundary of integration for CAPE, calculated as the area between the black and red lines.

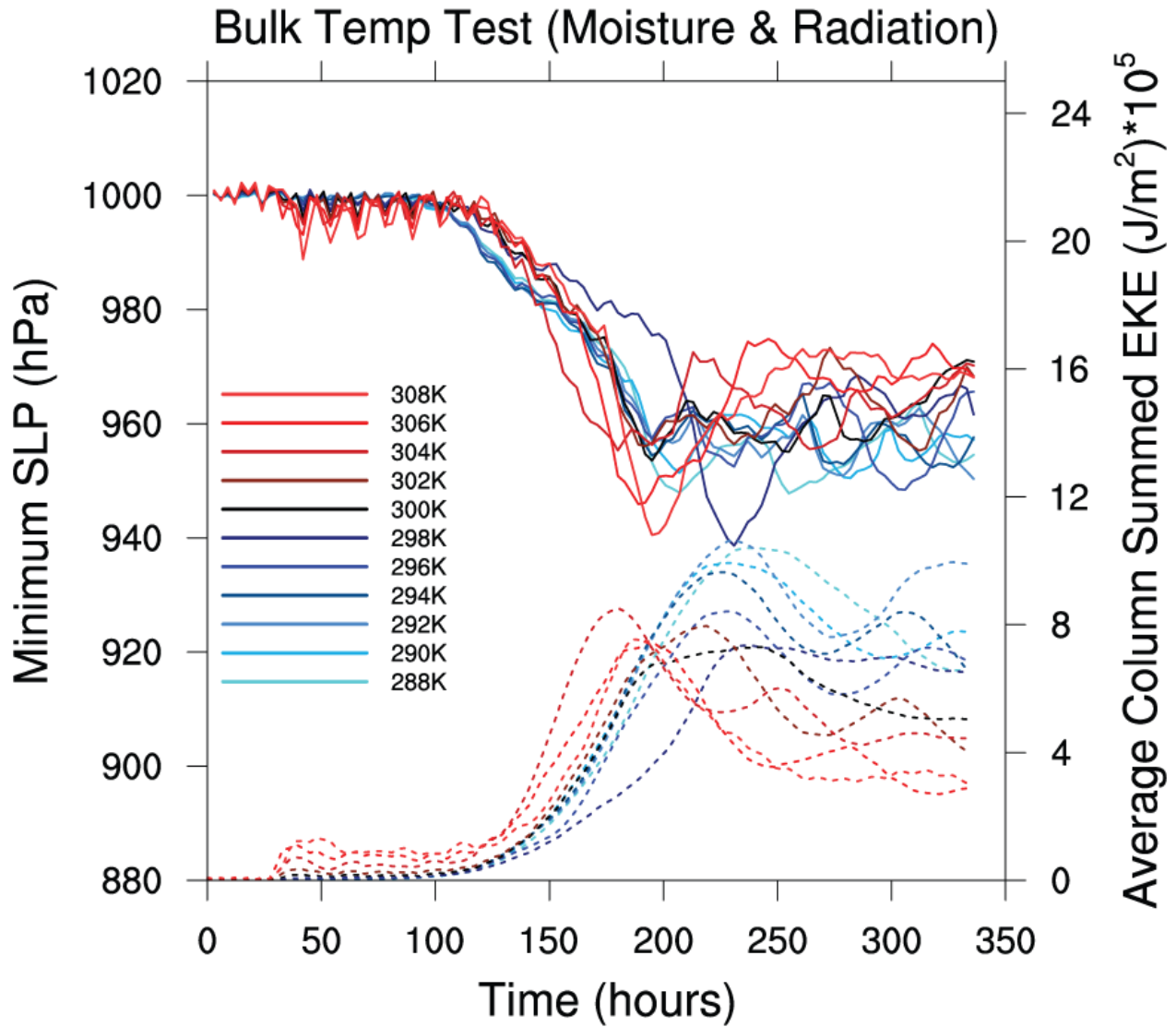


**Figure 5-5.** Average column-summed EKE (dashed lines) and minimum SLP (solid lines) for 11 runs spanning (in steps of 2 K) the moist beta-plane bulk temperature univariate test with radiative processes.

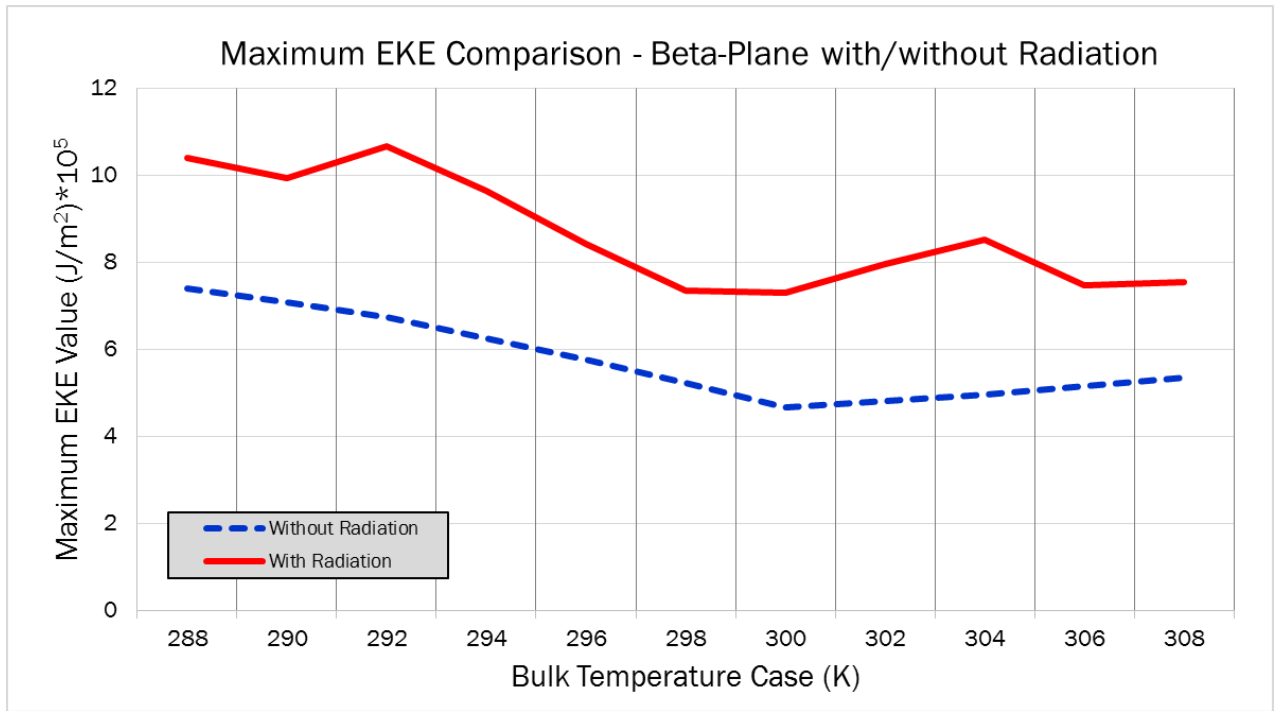


**Figure 5-6.** Maximum EKE response to changes in temperature/moisture content for beta-plane configurations with and without radiative processes enabled. The jet amplitude factor is equal to 1.0 for all runs.

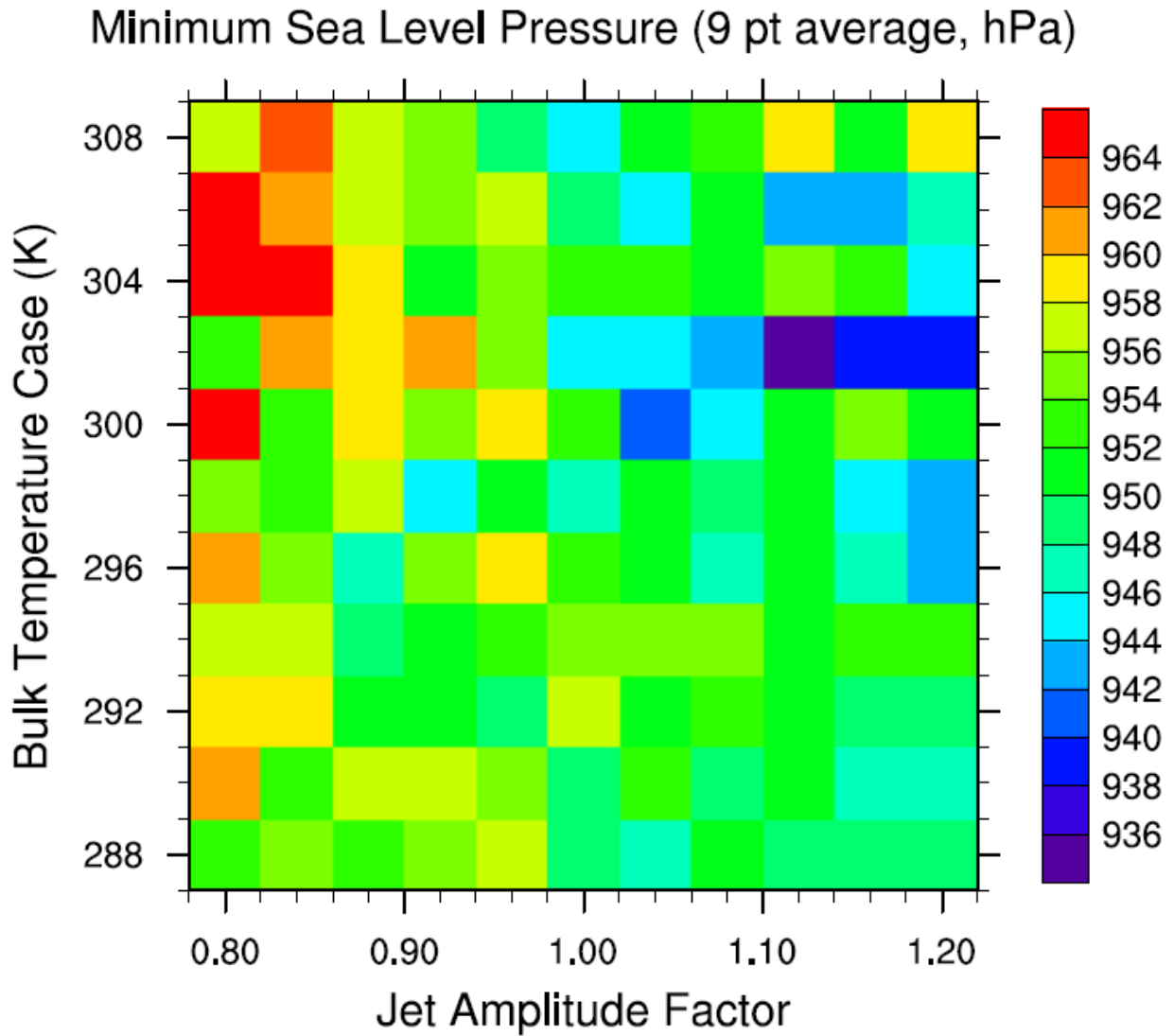


**Figure 5-7.** Minimum SLP (in hPa) during the lifetime of each ETC tested in the bivariate sensitivity test on a beta-plane with radiative processes enabled. The 9 point minimum SLP is determined by taking the average SLP of a 3 by 3 gridpoint box centered on the minimum SLP point in the domain.

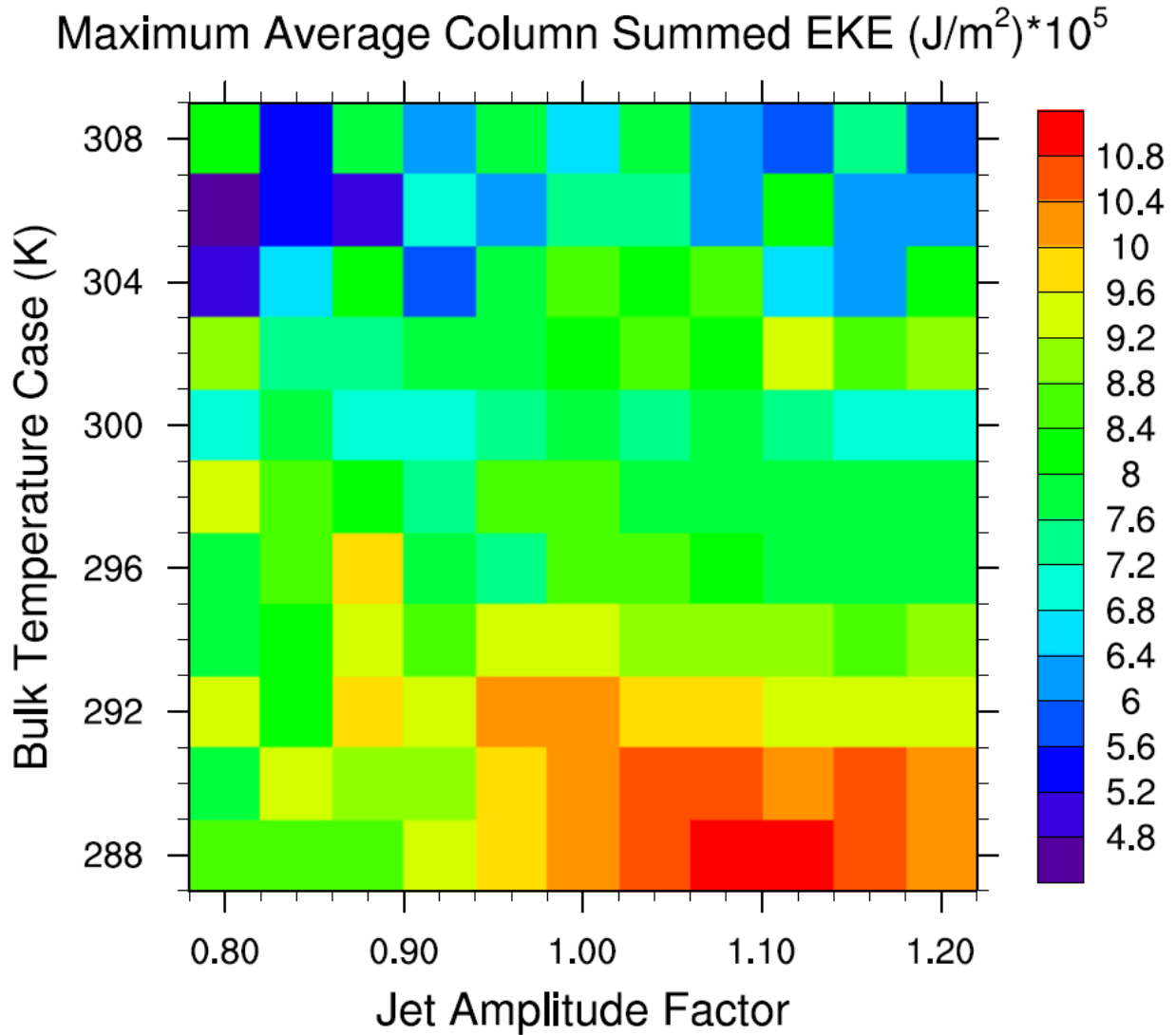


**Figure 5-8.** Maximum value of the full-domain averaged column-summed EKE (in  $(\text{J/m}^2)*10^5$ ) during the lifetime of each ETC tested in the bivariate sensitivity test on a beta-plane with radiative processes enabled.

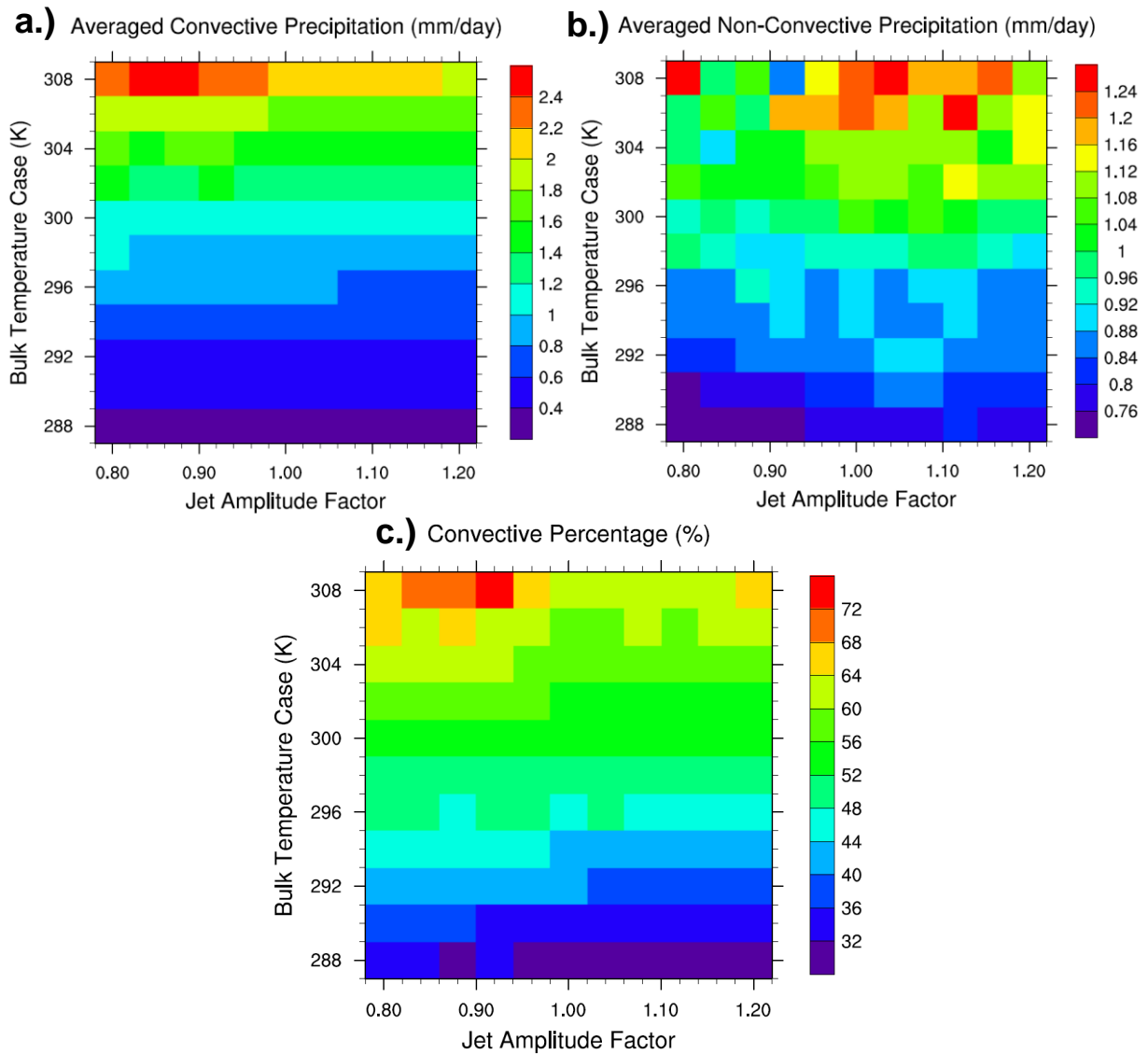


**Figure 5-9.** Temporally and spatially averaged (across the entire domain) values of convective precipitation (mm/day, Figure 5-9a), non-convective precipitation (mm/day, Figure 5-9b), and convective percentage of precipitation (Figure 5-9c) for each ETC in the bivariate sensitivity test on a beta-plane with radiative processes enabled.

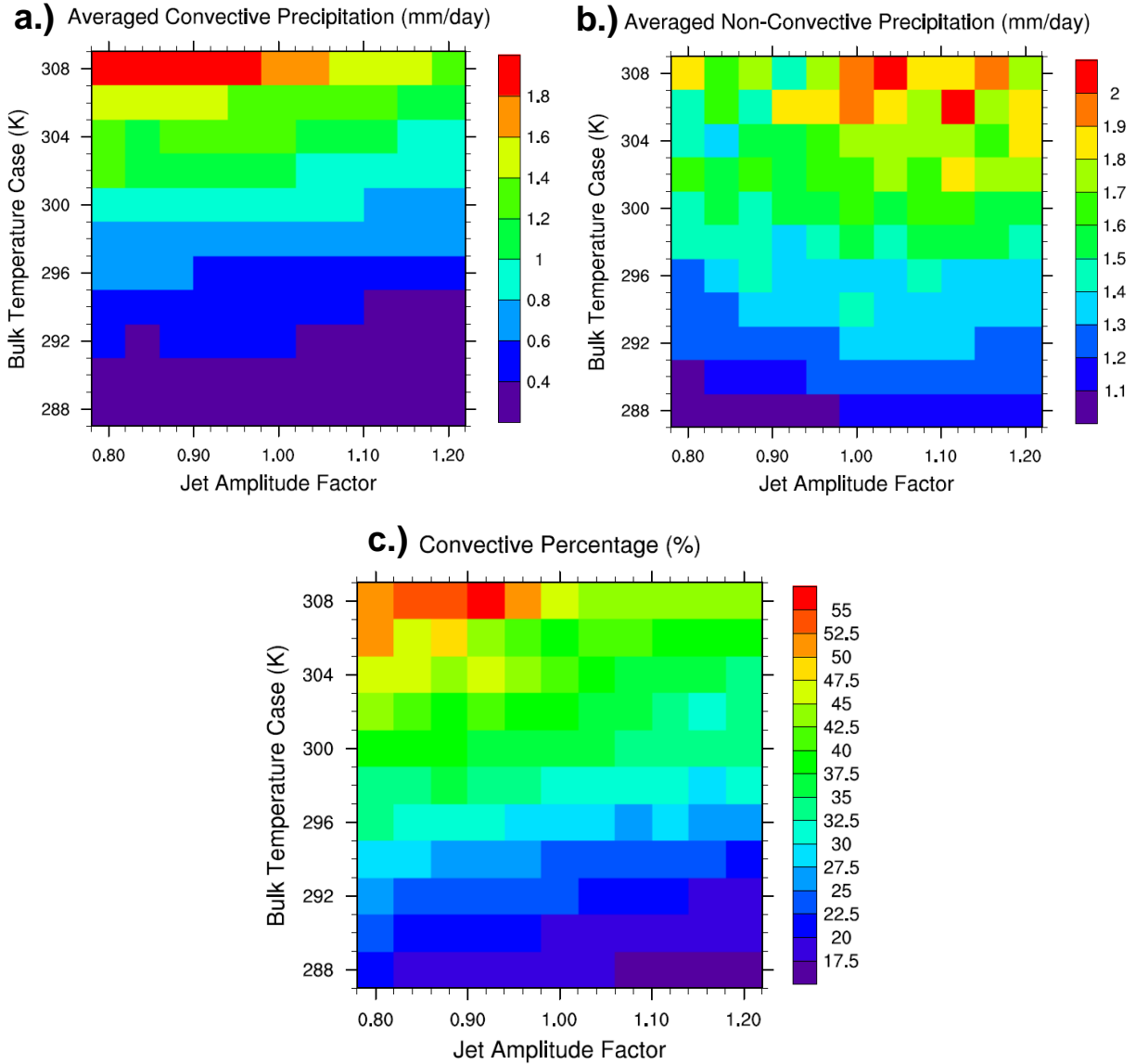
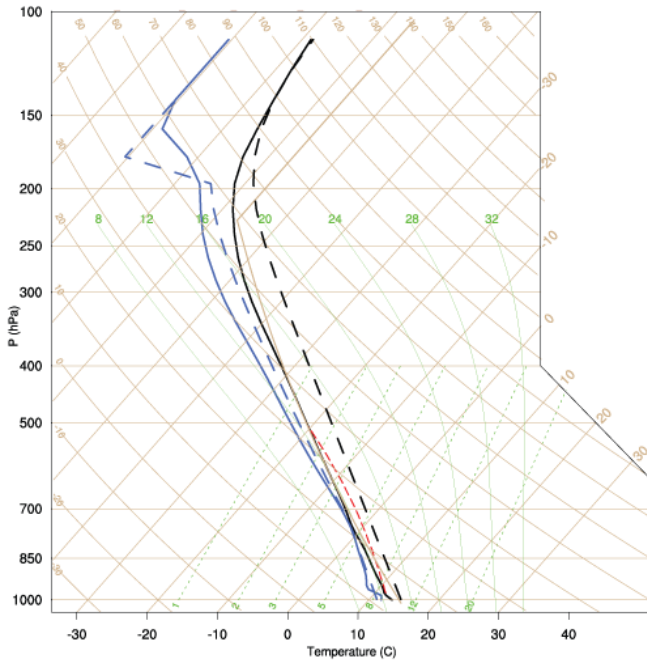


**Figure 5-10.** Temporally (over the duration of the simulation) and spatially (from 25 – 72°N, between the 100<sup>th</sup> and 300<sup>th</sup> row of grid points within the model) averaged values of convective precipitation (mm/day, Figure 5-10a), non-convective precipitation (mm/day, Figure 5-10b), and convective percentage of precipitation (Figure 5-10c) for each ETC in the bivariate sensitivity test on a beta-plane with radiative processes enabled.

a.) Initial & Day 5 Soundings, Bulk Temperature Case = 288 K



b.) Initial & Day 5 Soundings, Bulk Temperature Case = 296 K

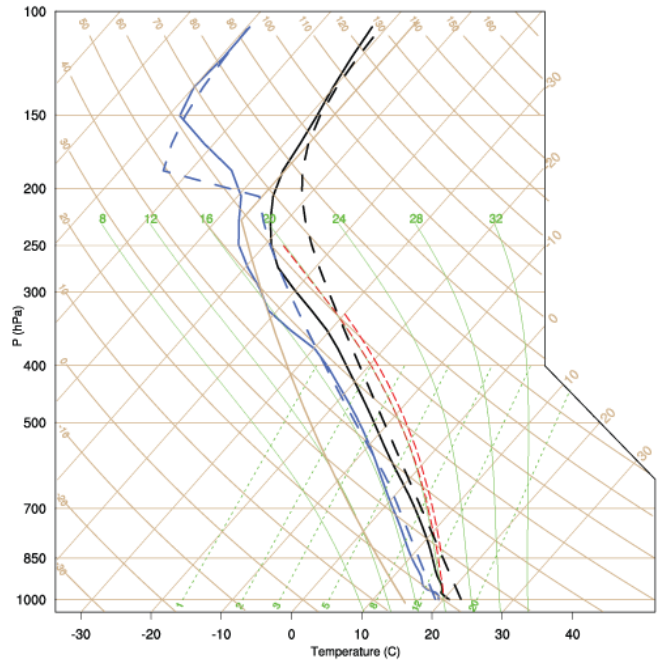


**Figure 5-11.** Longitudinally-averaged atmospheric profiles taken one-quarter of the way into the domain (from the south) at initialization of the 288 K simulation (Fig. 5-11a, dashed lines), 00Z on Day 5 of the 288K simulation (Fig. 5-11a, solid lines), initialization of the 296 K simulation (Fig. 5-11b, dashed lines), and 00Z on Day 5 of the 296K simulation (Fig. 5-11b, solid lines). Within these soundings, plotted on Skew-T Log-P diagrams, black lines indicate the environmental temperature and blue lines indicate the environmental dewpoint. Red dashed lines are the theoretical temperatures of parcels raised from the surface and allowed to freely convect, and indicate the boundary of integration for CAPE, calculated as the area between the black and red lines.

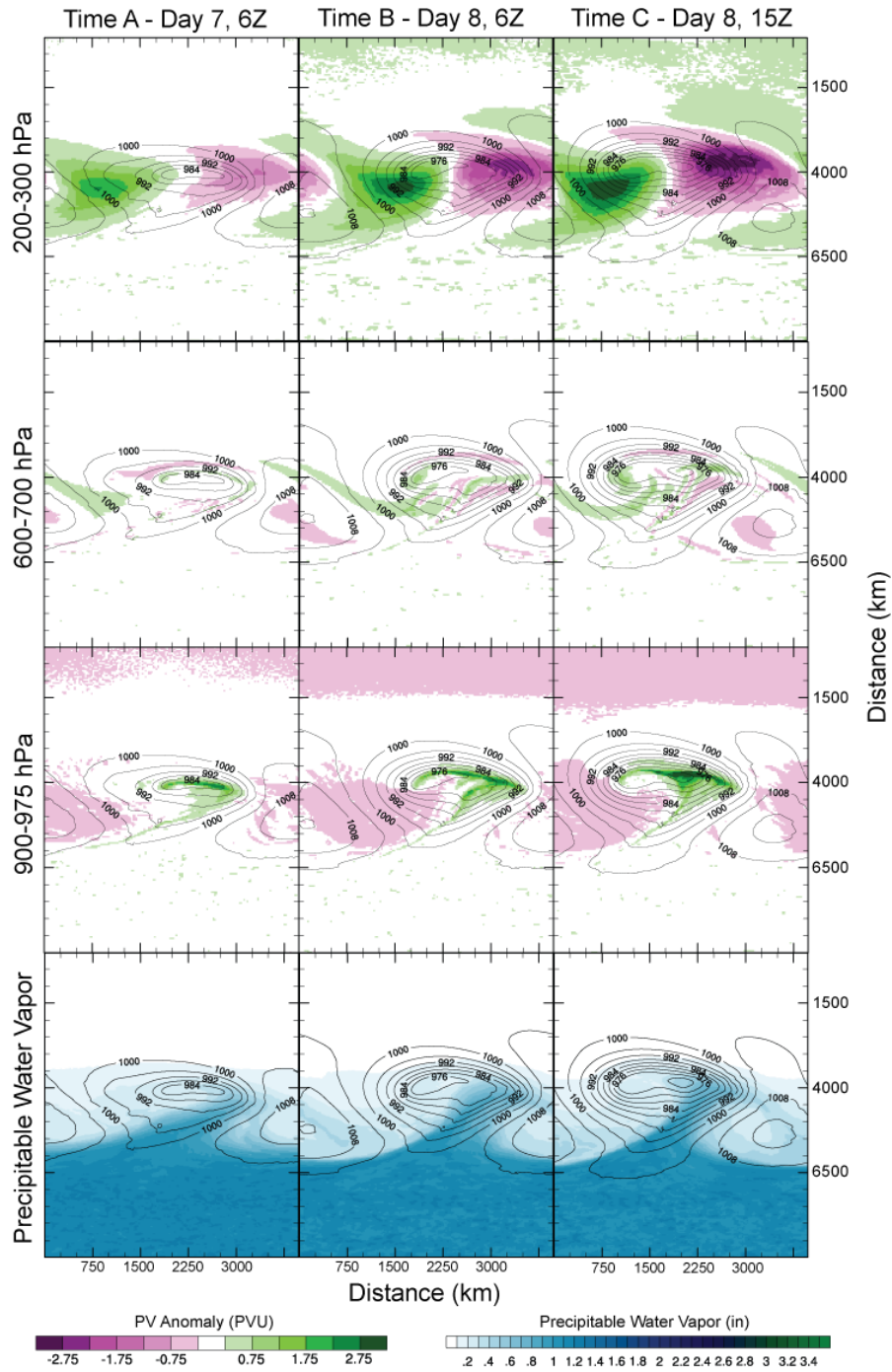


**Figure 5-12.** Four-panel PV anomaly and precipitable water vapor analysis of the 292 K bulk temperature case on a beta-plane with radiative processes enabled, conducted at Times A-C (indicated at the top of the figure), with overlaid sea level pressure contours (hPa).

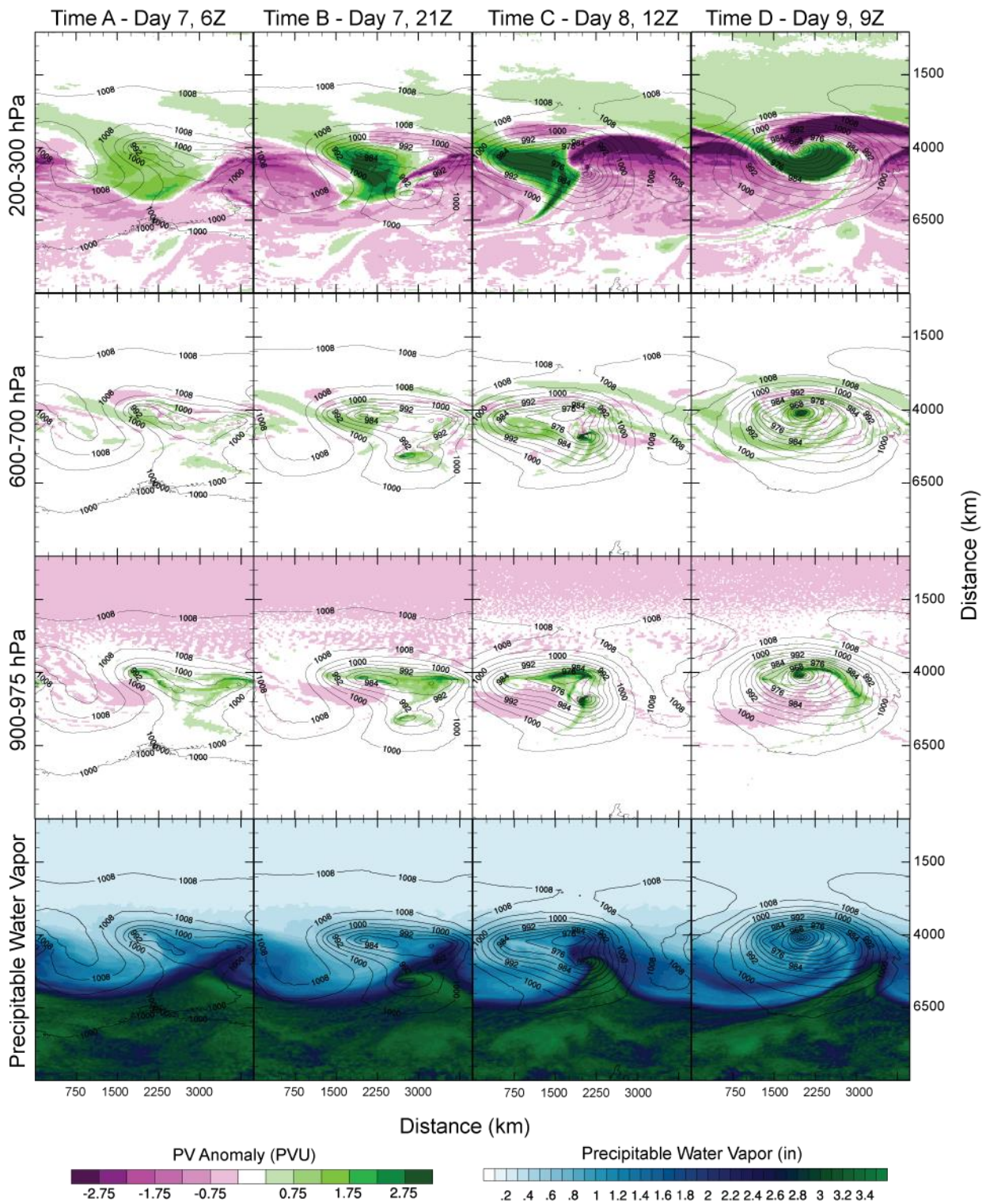


**Figure 5-13.** Four-panel PV anomaly and precipitable water vapor analysis of the 308 K bulk temperature case on a beta-plane with radiative processes enabled, conducted at Times A-D (indicated at the top of the figure), with overlaid sea level pressure contours (hPa).

## Day 7, 6:00Z Sounding, Bulk Temperature Case = 308 K

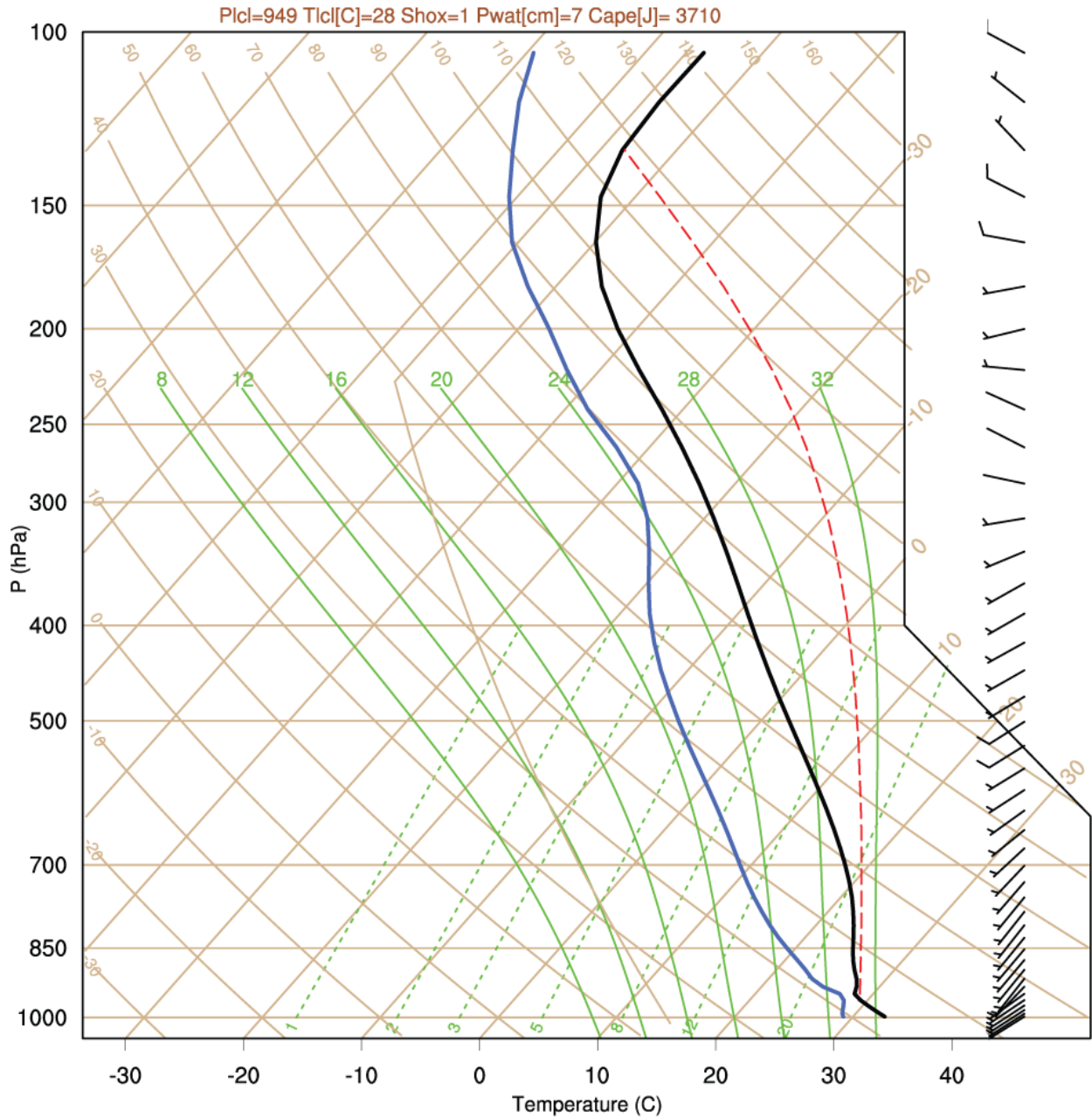


**Figure 5-14.** Longitudinally-averaged atmospheric profiles taken one-quarter of the way into the domain (from the south) at 06 Z on Day 7 of the 308 K simulation. Within these soundings, plotted on Skew-T Log-P diagrams, black lines indicate the environmental temperature and blue lines indicate the environmental dewpoint. Red dashed lines are the theoretical temperatures of parcels raised from the surface and allowed to freely convect, and indicate the boundary of integration for CAPE, calculated as the area between the black and red lines.

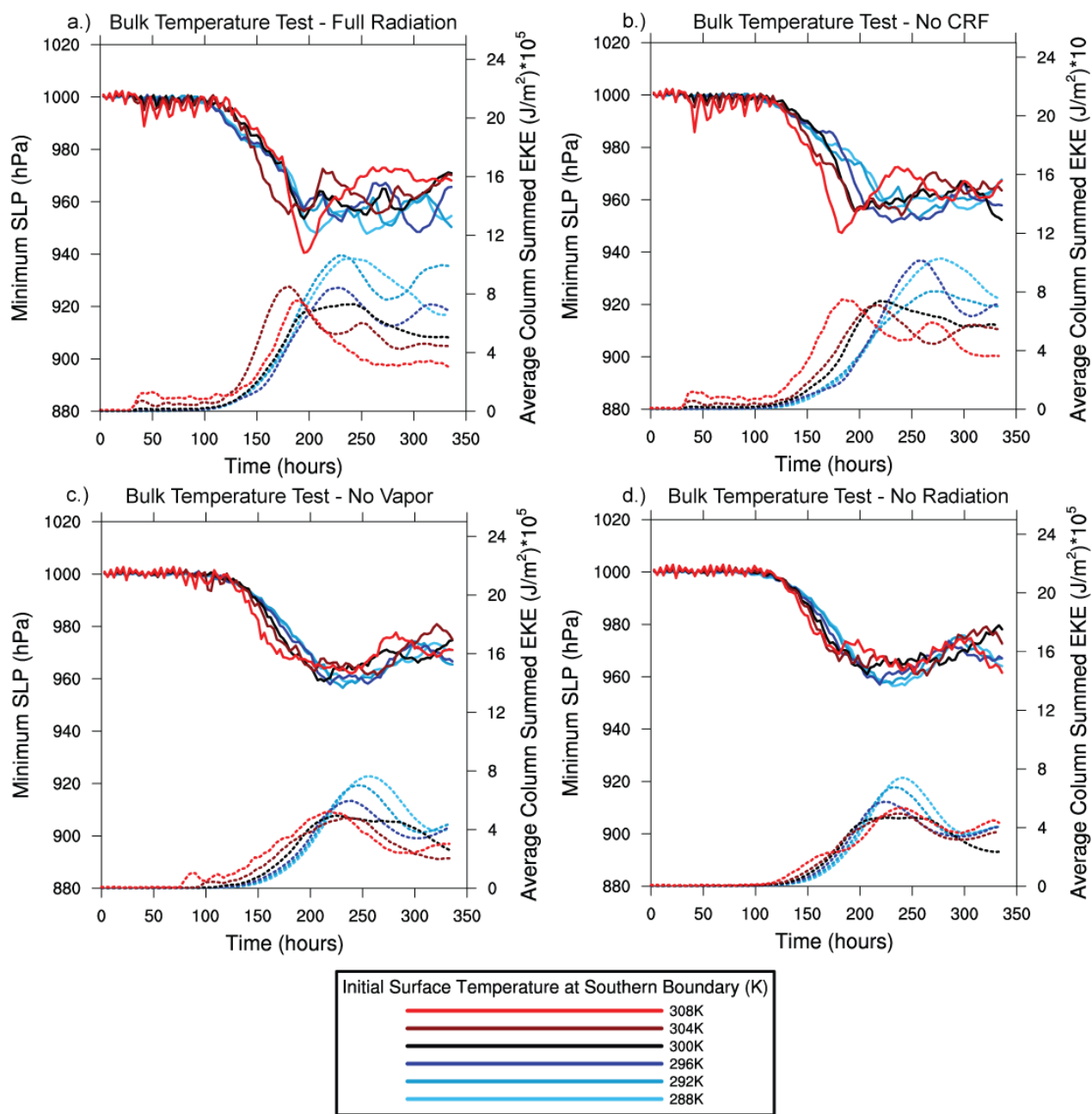
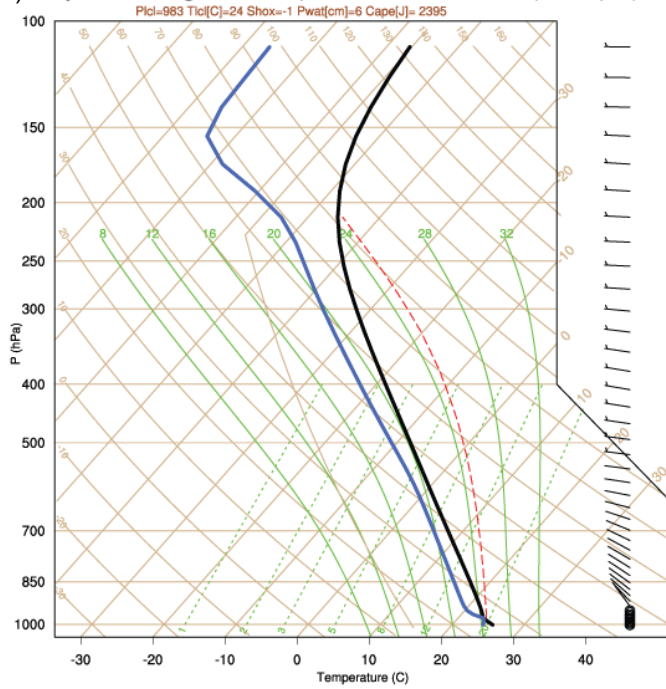


**Figure 5-15.** Average column-summed EKE (dashed lines) and minimum SLP (solid lines) for the 6 runs spanning the moist baroclinicity univariate test with radiation enabled (Fig. 5-15a), without cloud radiative forcing (Fig. 5-15b), without interactions with water in all forms, including vapor (Fig. 5-15c), and without any radiative processes (Fig. 5-15d). All experiments presented are run on a beta-plane.

a.) Day 5 Sounding, Bulk Temperature Case = 300 K (No Vapor)



b.) Day 5 Sounding, Bulk Temperature Case = 300 K (No Radiation)

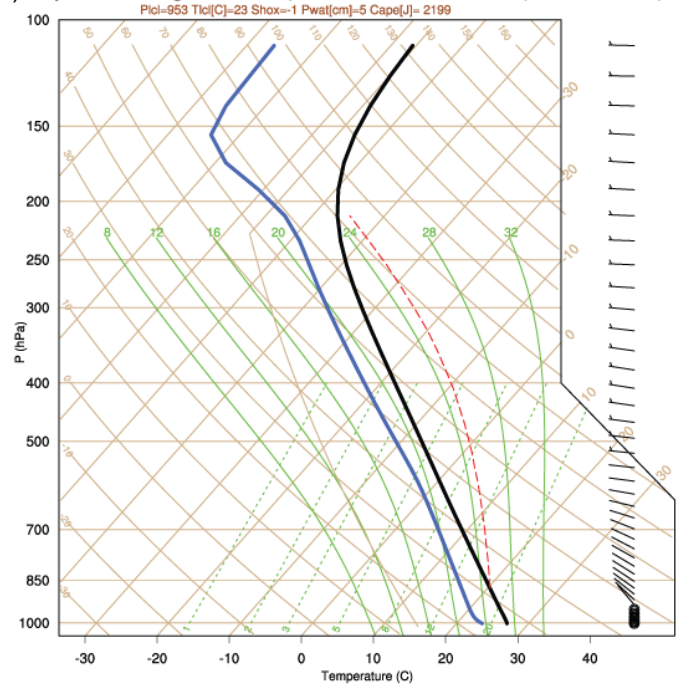


**Figure 5-16.** Longitudinally-averaged atmospheric profiles taken one-quarter of the way into the domain (from the south) at 00 Z on Day 5 of the 300 K simulation, without radiative interactions with water (Fig. 5-16a), and without all radiative processes (Fig. 5-16b). Within these soundings, plotted on Skew-T Log-P diagrams, black lines indicate the environmental temperature and blue lines indicate the environmental dewpoint. Red dashed lines are the theoretical temperatures of parcels raised from the surface and allowed to freely convect, and indicate the boundary of integration for CAPE, calculated as the area between the black and red lines.

## Chapter 6: Conclusions

Although commonly discussed in the context of rising temperatures, projected changes to the Earth's climate should be considered as much more than simply atmospheric warming. Follow-on impacts to atmospheric moisture content, equator-to-pole temperature gradients, sea surface temperatures, and stability are also critical in shaping the day-to-day conditions that impact society. In the midlatitudes of the planet, where much of the population resides, extratropical cyclones are a tangible vehicle of climate change. Their impacts include heavy precipitation, strong wind, and severe weather, all of which are potentially damaging to property and human life. It is therefore important to understand how extratropical cyclones might change in future climate conditions, with flexibility for the uncertainty involved in climate prediction.

While many previous studies have used non-physical or unrealistic methods to perturb simulations, we have created a novel initialization method that allows for natural temperature changes as a proxy for increasing moisture. Moreover, we include controls on domain baroclinicity to account for projected variation in the equator-to-pole temperature gradient, another novelty not present in the literature to this point, which often focuses on one environmental characteristic or prescribed emissions scenarios. This modeling configuration is then used to perform three successive sets experiments stepping towards a fuller realization of the Earth's climate system.

Chapter 3 presented the first step, verifying the robustness of the new initialization method in producing similar results to past literature. We begin with univariate experiments testing the sensitivity of ETCs on an  $f$ -plane to both bulk temperature (a proxy test for moisture) and baroclinicity. Consistent with Boutle et al. (2011), we find an increase in simulation-maximum eddy kinetic energy and a decrease in simulation-minimum sea level pressure with increasing baroclinicity. Also consistent with both Boutle et al. (2011) and Booth et al. (2013), we find non-monotonic responses to both simulation-maximum eddy kinetic energy and simulation-minimum sea level pressure, implying the existence of an ideal environment for ETC strength. This maximum is confirmed in the corresponding bivariate experiment, which attempts to replicate future climate conditions by simultaneously perturbing both environmental characteristics. Dynamical analysis finds increased vertical redirection of momentum in the warm conveyor belt of warmer ETCs, owing to a greater incidence of convection. Within this diabatically-limited regime, convection works to reduce the overall size of the ETC and limit its strength.

Chapter 4 extended the results of the  $f$ -plane experiments by including latitudinally-varying Coriolis configurations, primarily the linear beta-plane approximation. Inclusion of the beta-plane brought the model closer to the dynamical environment on Earth, and allowed the baroclinic wave generated to take advantage of the latitudinally-varying Coriolis parameter. Our univariate sensitivity experiments were repeated, and most notably, the response to increasing temperature was a non-monotonic response in both simulation-minimum SLP and simulation-maximum EKE, but with decreases in strength at cooler temperatures before increasing in strength at the warmest temperature. Focusing on the dynamical aspects of the warmest simulation, the existence of a diabatically-driven mode of ETC genesis was found through the

generation of a diabatic Rossby wave. In extending the bulk temperature parameter space and comparing the results on both an  $f$ -plane and a beta-plane, a qualitatively similar response of simulation-maximum EKE to changes in bulk temperature was also found, although the response function was transposed to lower temperatures in beta-plane simulations. Finally, a three-regime model of ETC genesis and development was proposed, covering baroclinic, diabatically-limited, and diabatically-driven regimes.

In Chapter 5 our model configuration considered additional energy pathways into and within the system by enabling radiative processes. The addition of radiation brought significant noise into the response functions to both strength metrics used, necessitating the use of an additional 5 runs within the univariate bulk temperature experiment. Response along both metrics looked vastly different from corresponding runs without radiative processes enabled, but comparison of results with radiative processes enabled and disabled revealed qualitative similarities in the response of simulation-maximum EKE to temperature. An increasing role of convection was visible as the convective percentage of precipitation increased with increasing temperature and moisture. Following on similar attribution studies of tropical cyclone sensitivity to radiative effects, we ran a suite of sensitivity experiments to determine the radiative processes most responsible for the shift in response behavior. Unlike tropical cyclones, which are strongly affected by cloud radiative forcing, atmospheric water vapor plays the largest role in shaping the ETC response mechanism.

In attempting to answer the outstanding question – “How do extratropical cyclones respond to varying environmental conditions?” – we offer the following methodological and scientific findings of this work as a partial answer and impetus for further exploration:

- 1.) Perturbation schemes leveraging the Clausius-Clapeyron relationship allow for more realistic perturbations of environmental moisture that do not rely on unrealistic adjustments to relative humidity or unphysical adjustments of latent heat release.
- 2.) Consideration of ETC sensitivity to multiple environmental parameters, adjusted simultaneously, enhances our understanding of system response and allows for flexibility across various cyclogenetic environments and climate scenarios.
- 3.) While the choice of Coriolis configuration in idealized ETC modeling may seem inconsequential in dry dynamical situations, the introduction of moist processes results in significant differences between  $f$ -plane and beta-plane configurations.
- 4.) Extratropical cyclone development can be divided into three regimes within climate-relevant environments:
  - a. Baroclinic – Existing within cooler environments, ETC cyclogenesis is by canonical methods. Diabatic heating from convection may play a small role in development, but does not hinder conversion of baroclinic potential energy.
  - b. Diabatically-Limited – In environments slightly warmer than those of the baroclinic regime, frequent convection redirects momentum vertically, resulting in a steeper WCB, and horizontal scale contraction. While these ETCs may be deeper than those in the baroclinic regime, they are less energetic, in the cyclone-summed sense.
  - c. Diabatically-Driven – At temperatures even warmer than the diabatically-limited regime, diabatic heating from convection dominates, serving as a surrogate for canonical PV gradients in cyclogenesis. Diabatic Rossby vortices develop initially before vortex merger leads to ETC development.

- 5.) The inclusion of radiative processes consistently strengthens ETCs. Moreover, with the addition of radiative processes, ETCs resemble the conceptual model of Shapiro and Keyser (1990), rather than the Norwegian cyclone model (Bjerknes, 1919).
- 6.) Unlike tropical cyclones, which are affected largely by cloud radiative forcing (Fovell et al. 2010; Bu et al. 2014), radiative processes primarily affect ETCs through their interaction with atmospheric water vapor.

The exact mechanism by which atmospheric water vapor affects ETC dynamics is left for future work – one of many promising directions that experiments in this dissertation could be extended and/or enhanced. Further exploration of the radiative effects on ETCs is a fascinating area of exploration, given its neglect to this point in the literature. In addition, while the consideration of simultaneously perturbing two environmental characteristics adds flexibility to the discussion of ETC response modification, perturbation schemes and variables can be further improved upon by adding considerations of relative humidity and sea surface temperature, for example, creating multivariate explorations of ETCs in future climates. Constructing such an experiment would also allow for relationships to be quantified between input parameters and output metrics, and significant work is already underway along this line of inquiry, with a 5-parameter pilot experiment consisting of 100 runs completed.

Such multivariate experiments require the use of creative techniques to explore these large parameter spaces, in order to avoid data volume and computational issues – increasingly relevant in an era of “big data”. Similar issues have beset efforts to enhance this work by removing its dependence on convective parameterizations. Promising work is underway to replicate these experiments at a 4 km grid spacing, as results between a pilot high resolution simulation and the control 25 km simulation presented in this dissertation were nearly identical.

However, considerations of data volume (greater than 5TB of data is produced per experiment), and data analysis have yet to be resolved. In addition, precipitation analysis for these simulations will require an algorithm to partition non-convective and convective precipitation. Such an algorithm has not been developed in the ETC community (although it does exist in the tropical cyclone community), and so additional tools need to be developed. These tools, along with continually growing computational power, will help us to further unlock the sensitivity behaviors of these behemoths of the midlatitudes.

## References

- Ahmadi-Givi, F., G. C. Graig, and R. S. Plant, 2004: The dynamics of a midlatitude cyclone with very strong latent-heat release. *Q. J. R. Meteorol. Soc.*, 130, 295–323, doi:10.1256/qj.02.226.
- Allen, M. R., and W. J. Ingram, 2002: Constraints on future changes in climate and the hydrologic cycle. *Nature*, 419, 224–232, doi: 10.1038/nature01092.
- American Meteorological Society, cited 2017: Extratropical Cyclone. Glossary of Meteorology. Available online at [http://glossary.ametsoc.org/wiki/Extratropical\\_cyclone](http://glossary.ametsoc.org/wiki/Extratropical_cyclone)].
- Balasubramanian, G. and M.K. Yau, 1994: The Effects of Convection on a Simulated Marine Cyclone. *J. Atmos. Sci.*, 51, 2397–2417
- Bjerknes, J., 1919: On the structure of moving cyclones. *Mon. Weather Rev.*, 47, 95–99.
- Bjerknes, J., and H. Solberg, 1922: Life cycle of cyclones and the polar front theory of atmospheric circulation. *Geofys. Publ.*, 3 (1), 1–18.
- Boettcher, M. and H. Wernli, 2013: A 10-yr Climatology of Diabatic Rossby Waves in the Northern Hemisphere. *Mon. Wea. Rev.*, 141, 1139–1154
- Boettcher, M., & Wernli, H., 2015: Diabatic Rossby waves in the Southern Hemisphere. *Quarterly Journal of the Royal Meteorological Society*, 141(693), 3106–3117.
- Booth, J. F., L. Polvani, P. O’Gorman, and S. Wang, 2015: Effective Stability in a Moist Baroclinic Wave, *Atmos Res Lett*, 16: 56–62.
- Booth, J. F., S. Wang, and L. M. Polvani, 2013: Midlatitude storms in a moister world: lessons from idealized baroclinic life cycle experiments. *Clim Dyn*, 41, 787–802.
- Boutle IA, Beare RJ, Belcher SE, Brown AR, Plant RS, 2010: The moist boundary layer under a mid-latitude weather system. *Boundary-Layer Meteorology*, 134, 367–386.
- Boutle IA, Belcher SE, Plant RS, 2011: Moisture transport in mid-latitude cyclones. *Q. J. R. Meteorol. Soc.*, 137, 360–367.
- Browning, K. A., 2004: The sting at the end of the tail: Damaging winds associated with extratropical cyclones. *Quarterly Journal of the Royal Meteorological Society*, 130(597), 375–399.
- Bu, Y. P., Fovell, R. G., & Corbosiero, K. L., 2014: Influence of cloud–radiative forcing on tropical cyclone structure. *Journal of the Atmospheric Sciences*, 71(5), 1644–1662.

- Caballero, R. and J. Hanley, 2012: Midlatitude Eddies, Storm-Track Diffusivity, and Poleward Moisture Transport in Warm Climates. *J. Atmos. Sci.*, 69, 3237–3250,
- Čampa, J., and H. Wernli, 2012: A PV perspective on the vertical structure of mature midlatitude cyclones in the Northern Hemisphere. *J. Atmos. Sci.*, 69, 725–740
- Catto, J. L., C. Jakob, G. Berry, and N. Nicholls, 2012: Relating global precipitation to atmospheric fronts. *Geophys. Res. Lett.*, 39, L10805
- Catto, J.L., L.C. Shaffrey, and K.I. Hodges, 2011: Northern Hemisphere Extratropical Cyclones in a Warming Climate in the HiGEM High-Resolution Climate Model. *J. Climate*, 24, 5336–5352, <https://doi.org/10.1175/2011JCLI4181.1>
- Chagnon, J. M., Gray, S. L. and Methven, J., 2013: Diabatic processes modifying potential vorticity in a North Atlantic cyclone. *Q. J. R. Meteorol. Soc.* 139: 1270–1282
- Champion AJ, Hodges KI, Bengtsson LO, Keenlyside NS, Esch M, 2011: Impact of increasing resolution and a warmer climate on extreme weather from Northern Hemisphere extratropical cyclones. *Tellus*, 63A, 893–906.
- Chang, C. B., Perkey, D. J., & Kreitzberg, C. W., 1982: A numerical case study of the effects of latent heating on a developing wave cyclone. *Journal of the Atmospheric Sciences*, 39(7), 1555-1570.
- Chang, E. K., Lee, S., & Swanson, K. L., 2002: Storm track dynamics. *Journal of Climate*, 15(16), 2163-2183.
- Chang, E.K. and S. Song, 2006: The Seasonal Cycles in the Distribution of Precipitation around Cyclones in the Western North Pacific and Atlantic. *J. Atmos. Sci.*, 63, 815–839, <https://doi.org/10.1175/JAS3661.1>
- Charney, J. G., 1947: The dynamics of long waves in a baroclinic westerly current. *J. Meteorol.*, 4, 136–162 , doi:10.1175/1520-0469(1947)004<0136:TDOLWI>2.0.CO;2.
- Charney, J.G. and A. Eliassen, 1964: On the Growth of the Hurricane Depression. *J. Atmos. Sci.*, 21, 68–75
- Chen, S. H., & Sun, W. Y., 2002: A one-dimensional time dependent cloud model. *Journal of the Meteorological Society of Japan. Ser. II*, 80(1), 99-118.
- Colucci, S. J., 1976: Winter Cyclone Frequencies over the Eastern United States and Adjacent Western Atlantic,—. *Bulletin of the American Meteorological Society*, 57(5), 548-553.
- Craig, G., & Cho, H. R., 1988: Cumulus heating and CISK in the extratropical atmosphere. Part I: Polar lows and comma clouds. *Journal of the atmospheric sciences*, 45(19), 2622-2640.
- Davies, H.C., C. Schär, and H. Wernli, 1991: The Palette of Fronts and Cyclones within a Baroclinic Wave Development. *J. Atmos. Sci.*, 48, 1666–1689, [https://doi.org/10.1175/1520-0469\(1991\)048<1666:TPOFAC>2.0.CO;2](https://doi.org/10.1175/1520-0469(1991)048<1666:TPOFAC>2.0.CO;2)
- Davis, C. A., 1992: A potential vorticity analysis of the importance of initial structure and condensational heating in observed cyclogenesis. *Mon. Weather Rev.*, 120, 2409-2428.

- Davis, C. A., and K. A. Emanuel, 1991: Potential vorticity diagnostics of cyclogenesis. *Mon. Weather Rev.*, 119, 1929–1953. doi:10.1175/1520-0493(1991)119<1929:PVDOC>2.0.CO;2.
- Davis, C. A., M. T. Stoelinga, and Y.-H. Kuo, 1993: The integrated effect of condensation in numerical simulations of extratropical cyclogenesis. *Mon. Weather Rev.*, 121, 2309–2330, doi:10.1175/1520-0493(1993)121<2309:TIEOCI>2.0.CO;2.
- Deveson, A. C. L., Browning, K. A. and Hewson, T. D. 2002: A classification of FASTEX cyclones using a height-attributable quasi-geostrophic vertical-motion diagnostic. *Q. J. R. Meteorol. Soc.*, 128: 93–117.
- Dudhia, J., 1989: Numerical study of convection observed during the winter monsoon experiment using a mesoscale two-dimensional model. *Journal of the Atmospheric Sciences*, 46(20), 3077-3107.
- Dudhia, J., 1993: A nonhydrostatic version of the Penn State-NCAR Mesoscale Model: Validation tests and simulation of an Atlantic cyclone and cold front. *Mon. Weather Rev.*, 121, 1493-1513.
- Eady, E. T., 1949: Long Waves and Cyclone Waves. *Tellus*, 1: 33–52. doi:10.1111/j.2153-3490.1949.tb01265.x
- Eckhardt, S., Stohl, A., Wernli, H., James, P., Forster, C., & Spichtinger, N., 2004: A 15-year climatology of warm conveyor belts. *Journal of climate*, 17(1), 218-237.
- Eichler, T., & Higgins, W., 2006: Climatology and ENSO-related variability of North American extratropical cyclone activity. *Journal of climate*, 19(10), 2076-2093.
- Emanuel, K. A., M. Fantini, and A. J. Thorpe, 1987: Baroclinic instability in an environment of small stability to slantwise moist convection. Part I: Two-dimensional models. *J. Atmos. Sci.*, 44, 1559–1573, doi:10.1175/1520-0469(1987)044<1559:BIIAEO>2.0.CO;2.
- Fantini, M., 1993: A numerical study of two-dimensional moist baroclinic instability. *Journal of the atmospheric sciences*, 50(9), 1199-1210.
- Fantini, M., 1995: Moist Eady waves in a quasigeostrophic three-dimensional model. *Journal of the atmospheric sciences*, 52(13), 2473-2485.
- Feldstein, S.B. and I.M. Held, 1989: Barotropic Decay of Baroclinic Waves in a Two-Layer Beta-Plane Model. *J. Atmos. Sci.*, 46, 3416–3430, [https://doi.org/10.1175/1520-0469\(1989\)046<3416:BDOBWI>2.0.CO;2](https://doi.org/10.1175/1520-0469(1989)046<3416:BDOBWI>2.0.CO;2)
- Field P. R., A. Gettelman, R. B. Neale, R. Wood, P. J. Rasch and H. Morrison, 2008: Cyclone compositing to constrain climate model behavior using satellite observations. *J. Clim.*, 21, 5887-5903.
- Field, P. R., and R. Wood, 2007: Precipitation and cloud structure in midlatitude cyclones. *J. Clim.*, 20, 233-254.
- Frei, C., C. Schär, D. Lüthi, and H. C. Davies, 1998: Heavy precipitation processes in a warmer climate. *Geophys. Res. Lett.*, 25, 1431–1434, doi:10.1029/98GL51099.

- Frierson, D.M., I.M. Held, and P. Zurita-Gotor, 2006: A Gray-Radiation Aquaplanet Moist GCM. Part I: Static Stability and Eddy Scale. *J. Atmos. Sci.*, 63, 2548–2566, <https://doi.org/10.1175/JAS3753.1>
- Fovell, R. G., and H. Su, 2007: Impact of cloud microphysics on hurricane track forecasts, *Geophys. Res. Lett.*, 34, L24810, doi:10.1029/2007GL031723.
- Fovell, R. G., K. L. Corbosiero, and H.-C. Kuo , 2009: Cloud microphysics impact on hurricane track as revealed in idealized experiments, *J. Atmos. Sci.*, 66, 1764–1778.
- Fovell, R. G., K. L. Corbosiero, A. Seifert, and K.-N. Liou, 2010: Impact of cloud-radiative processes on hurricane track, *Geophys. Res. Lett.*, 37, L07808, doi:10.1029/2010GL042691.
- Fovell, R.G., Bu, Y.P., Corbosiero, K.L., Tung, W.W., Cao, Y., Kuo, H.C., Hsu, L.H. and Su, H., 2016: Influence of cloud microphysics and radiation on tropical cyclone structure and motion. *Meteorological Monographs*, 56, 11-1.
- Gall, R., 1976: Structural Changes of Growing Baroclinic Waves. *J. Atmos. Sci.*, 33, 374–390,
- Grams, C. M., and Coauthors, 2011: The key role of diabatic processes in modifying the upper-tropospheric wave guide: a North Atlantic case-study. *Q. J. R. Meteorol. Soc.*, 137, 2174–2193. doi: 10.1002/qj.891.
- Green, J. S. A., 1970: Transfer properties of the large-scale eddies and the general circulation of the atmosphere. *Q.J.R. Meteorol. Soc.*, 96: 157–185.
- Grell, G. A., and D. Dévényi, 2004: A generalized approach to parameterizing convection combining ensemble and data assimilation techniques, *Geophys. Res. Lett.*, 29(14),
- Hartmann, D. L., 1994: *Global Physical Climatology*. Academic Press, 411 pp.
- Hawcroft, M. K., L. C. Shaffrey, K. I. Hodges, and H. F. Dacre, 2012: How much Northern Hemisphere precipitation is associated with extratropical cyclones? *Geophys. Res. Lett.*, 39, L24809, doi:10.1029/2012GL053866.
- Held, I. M., & Soden, B. J., 2000: Water vapor feedback and global warming. *Annual review of energy and the environment*, 25(1), 441-475.
- Held, I., and B. Soden, 2006: Robust responses of the hydrological cycle to global warming. *J. Clim.*, 19, 5686–5699.
- Hong S-Y, Noh Y, Dudhia J, 2006: A new vertical diffusion package with an explicit treatment of entrainment processes. *Mon Weather Rev.*, 134, 2318–2341.
- Hoskins, B. J., M. E. McIntyre, and A. W. Robertson, 1985: On the use and significance of isentropic potential vorticity maps. *Q. J. R. Meteorol. Soc.*, 111, 877–946.
- Hoskins, B. J., & Hodges, K. I., 2002: New perspectives on the Northern Hemisphere winter storm tracks. *Journal of the Atmospheric Sciences*, 59(6), 1041-1061.
- Hoskins, B. J., & Hodges, K. I., 2005: A new perspective on Southern Hemisphere storm tracks. *Journal of Climate*, 18(20), 4108-4129.

- Igel, A. L., and S. C. van den Heever, 2014: The role of latent heating in warm frontogenesis. *Q. J. R. Meteorol. Soc.*, 140, 139–150, doi:10.1002/qj.2118.
- Igel, A.L., S.C. van den Heever, C.M. Naud, S.M. Saleeby, and D.J. Posselt, 2013: Sensitivity of warm frontal processes to cloud-nucleating aerosol concentrations. *J. Atmos. Sci.*, 70, 1768-1783.
- IPCC, 2014: Climate Change 2014: Synthesis Report. Contribution of Working Groups I, II and III to the Fifth Assessment Report of the Intergovernmental Panel on Climate Change [Core Writing Team, R.K. Pachauri and L.A. Meyer (eds.)]. IPCC, Geneva, Switzerland, 151 pp.
- Jablonowski C, Williamson DL. 2006: A baroclinic instability test case for atmospheric model dynamical cores. *Q. J. R. Meteorol. Soc.* 132: 2943–2975.
- Joos, H. and Wernli, H., 2012: Influence of microphysical processes on the potential vorticity development in a warm conveyor belt: a case-study with the limited-area model COSMO. *Q. J. R. Meteorol. Soc.* 138: 407–418. doi: 10.1002/qj.934
- Jung, T., S. K. Gulev, I. Rudeva, and V. Soloviov, 2006: Sensitivity of extratropical cyclone characteristics to horizontal resolution in the ECMWF model. *Q. J. R. Meteorol. Soc.*, 132, 1839–1857.
- Kain, J.S., and J.M. Fritsch, 1993: Convective parameterization for mesoscale models: The Kain-Fritsch scheme. The representation of cumulus convection in numerical models. *Meteor. Monogr.*, No. 24, Amer. Meteorol. Soc., 165-170.
- Kuo, H., 1949: Dynamic instability of two-dimensional nondivergent flow in a barotropic atmosphere *J. Meteor.*, 6, 105–122,
- Kuo, Y.-H., M. A. Shapiro, and E. G. Donall, 1991: The interaction between baroclinic and diabatic processes in a numerical simulation of a rapidly intensifying extratropical marine cyclone. *Mon. Weather Rev.*, 119, 368-384.
- Kuo, Y-H., and R. J. Reed, 1988: Numerical simulations of an explosively deepening cyclone in the eastern Pacific. *Mon. Weather Rev.*, 116, 2081–2105.
- Lapeyre, G., and I. M. Held, 2004: The role of moisture in the dynamics and energetics of turbulent baroclinic eddies. *J. Atmos. Sci.*, 61, 1693–1710
- Li F, Collins WD, Wehner MF, Williamson DL, Olson JG, 2011: Response of precipitation extremes to idealized global warming in an aqua-planet climate model: towards a robust projection across different horizontal resolutions. *Tellus* 63A, 876–883
- Lin, Y. L., Farley, R. D., & Orville, H. D., 1983: Bulk parameterization of the snow field in a cloud model. *Journal of Climate and Applied Meteorology*, 22(6), 1065-1092.
- Mak, M., 1982: On moist quasi-geostrophic baroclinic instability. *J. Atmos. Sci.*, 39, 2028–2037
- Marciano, C. G., G. M. Lackmann, and W. A. Robinson, 2015: Changes in U.S. east coast cyclone dynamics with climate change. *J. Clim.*, 28, 468–484, doi:10.1175/JCLI-D-14-00418.1.

- Mlawer, E. J., Taubman, S. J., Brown, P. D., Iacono, M. J., & Clough, S. A., 1997: Radiative transfer for inhomogeneous atmospheres: RRTM, a validated correlated-k model for the longwave. *Journal of Geophysical Research: Atmospheres*, 102(D14), 16663-16682.
- Moore, R. W., and M. T. Montgomery, 2004: Reexamining the dynamics of short-scale, diabatic Rossby waves and their role in midlatitude moist cyclogenesis. *J. Atmos. Sci.*, 61, 754–768.
- Moore, R. W., and M. T. Montgomery, 2005: Analysis of an idealized, three-dimensional diabatic Rossby vortex: A coherent structure of the moist baroclinic atmosphere. *J. Atmos. Sci.*, 62, 2703–2725.
- Moore, R. W., Montgomery, M. T., & Davies, H., 2013: Genesis criteria for diabatic Rossby vortices: A model study. *Monthly Weather Review*, 141(1), 252-263.
- Morrison, H., J. Curry, and V. Khvorostyanov, 2005: A New Double-Moment Microphysics Parameterization for Application in Cloud and Climate Models. Part I: Description. *J. Atmos. Sci.*, 62, 1665–1677, doi: 10.1175/JAS3446.1.
- Morrison, H., and A. Gettelman, 2008: A new two-moment bulk stratiform cloud microphysics scheme in the NCAR Community Atmosphere Model, version 3 (CAM3). Part I: Description and numerical tests. *J. Clim.*, 21, 3642–3659, doi:10.1175/2008JCLI2105.1.
- Morrison, H., G. Thompson, and V. Tatarskii, 2009: Impact of cloud microphysics on the development of trailing stratiform precipitation in a simulated squall line: Comparison of one- and two-moment schemes. *Mon. Wea. Rev.*, 137, 991–1007, doi:10.1175/2008MWR2556.1.
- Nieman, P. J., and M. A. Shapiro, 1993: The life cycle of an extratropical marine cyclone. Part I: Frontal-cyclone evolution and thermodynamic air–sea interaction. *Mon. Weather Rev.*, 121, 2153–2176.
- O’Gorman, P.A. and T. Schneider, 2008: Energy of Midlatitude Transient Eddies in Idealized Simulations of Changed Climates. *J. Climate*, 21, 5797–5806, <https://doi.org/10.1175/2008JCLI2099.1>
- Olson, J. B., and B. A. Colle, 2007: A modified approach to initialize an idealized extratropical cyclone within a mesoscale model. *Mon. Weather Rev.*, 135, 1614–1624, doi:10.1175/MWR3364.1.
- Overland, J.E., Wang, M., 2010: Large-scale atmospheric circulation changes are associated with the recent loss of Arctic sea ice. *Tellus*, 62A, 1–9.
- Parker, D. J., and A. J. Thorpe, 1995: Conditional convective heating in a baroclinic atmosphere: A model of convective frontogenesis. *J. Atmos. Sci.*, 52, 1699–1711
- Pavan, V., Hall, N. & Blackburn, M., 1999: The importance of moisture distribution for the growth and energetics of mid-latitude systems. *Annales Geophysicae* (1999) 17: 242.
- Pepler, A. S., A. Di Luca, F. Ji, L. V. Alexander, J. P. Evans, and S. C. Sherwood (2016), Projected changes in east Australian midlatitude cyclones during the 21st century, *Geophys. Res. Lett.*, 43, 334–340, 3

- Petterssen, S. and Smebye, S. J., 1971: On the development of extratropical cyclones. *Q. J. R. Meteorol. Soc.*, 97: 457–482.
- Pfahl, S., P. A. O’Gorman, and M. S. Singh, 2015: Extratropical cyclones in idealized simulations of changed climates. *J. Clim*, 28, 9373–9392
- Pierrehumbert, R. T., 2002: The hydrologic cycle in deep-time climate problems. *Nature*, 419(6903), 191-198.
- Plant, R. S., Craig, G. C. and Gray, S. L., 2003: On a threefold classification of extratropical cyclogenesis. *Q. J. R. Meteorol. Soc.*, 129: 2989–3012.
- Polly, J. B., & Rossow, W. B., 2016: Cloud Radiative Effects and Precipitation in Extratropical Cyclones. *Journal of Climate*, 29(18), 6483-6507.
- Polvani, L. M., and J. G. Esler, 2007: Transport and mixing of chemical air masses in idealized baroclinic life cycles. *J. Geophys. Res.*, 112, D23102.
- Posselt, D. J., and J. E. Martin, 2004: The effect of latent heat release on the evolution of a warm occluded thermal structure. *Mon. Weather Rev.*, 132, 578–599
- Ranson, M., Kousky, C., Ruth, M., Jantarasami, L., Crimmins, A., & Tarquinio, L., 2014: Tropical and extratropical cyclone damages under climate change. *Climatic change*, 127(2), 227.
- Raymond, D. J., and H. Jiang, 1990: A Theory for Long-Lived Mesoscale Convective Systems. *J. Atmos. Sci.*, 47, 3067–3077.
- Reed, R. J., A. J. Simmons, M. D. Albright, and P. Unden, 1988: The role of latent heat release in explosive cyclogenesis: Three examples based on ECMWF operational forecasts. *Wea. Forecast.*, 3, 217-229.
- Reeves, H. D., and G. M. Lackmann, 2004: An Investigation of the Influence of Latent Heat Release on Cold-Frontal Motion. *Mon. Weather Rev.*, 132, 2864-2881.
- Rossby, C. G., 1936: Dynamics of steady ocean currents in the light of experimental fluid mechanics. Massachusetts Institute of Technology and Woods Hole Oceanographic Institution.
- Rossby, C-G., 1939: Relation between variations in the intensity of the zonal circulation of the atmosphere and the displacements of the semi-permanent centers of action. *J. Marine Res.*, 2, 38-55.
- Rotunno, R., W.C. Skamarock, and C. Snyder, 1994: An Analysis of Frontogenesis in Numerical Simulations of Baroclinic Waves. *J. Atmos. Sci.*, 51, 3373–3398,
- Sanders, F., & Gyakum, J. R., 1980: Synoptic-dynamic climatology of the “bomb”. *Monthly Weather Review*, 108(10), 1589-1606.
- Schemm S, Wernli H, Papritz L., 2013: Warm conveyor belts in idealized moist baroclinic wave simulations. *J. Atmos. Sci* 70: 627–652.

- Schemm, S., H. Wernli, and L. Papritz, 2013: Warm Conveyor Belts in Idealized Moist Baroclinic Wave Simulations. *J. Atmos. Sci.*, 70, 627–652,
- Schneider, T., P. A. O’Gorman, and X. J. Levine, 2010: Water vapor and the dynamics of climate changes, *Rev. Geophys.*, 48, RG3001,.
- Screen, J. A., and I. Simmonds, 2013: Exploring links between Arctic amplification and mid-latitude weather, *Geophys. Res. Lett.*, 40, 959–964,
- Screen, J.A. and I. Simmonds, 2010: The central role of diminishing sea ice in recent Arctic temperature amplification, *Nature*, 464, 1334–1337.
- Serreze, M.C. and R.G. Barry, 2011: Processes and impacts of Arctic amplification: A research synthesis, *Glob Planet. Chang*, 77, 85–96.
- Shaw, T.A., Baldwin, M., Barnes, E.A., Caballero, R., Garfinkel, C.I., Hwang, Y.T., Li, C., O’Gorman, P.A., Rivière, G., Simpson, I.R. and Voigt, A., 2016: Storm track processes and the opposing influences of climate change *Nat. Geosci.* 9 656–64
- Shapiro, L. J., and D. Keyser, 1990: Fronts, jet streams, and the tropopause. *Extratropical Cyclones: The Erik Palmén Memorial Volume*, C. W. Newton and E. O. Holopainen, Eds., *Amer. Meteorol. Soc.*, 167–191.
- Sherwood, S. C., R. Roca, T. M. Weckwerth, and N. G. Andronova, 2010: Tropospheric water vapour, convection and climate. *Rev. Geophys.*, 48, RG2001
- Simmons, A.J. and Hoskins, B.J., 1977. Baroclinic instability on the sphere: Solutions with a more realistic tropopause. *J. Atmos. Sci.*, 34, 581-588.
- Simmons, A.J. and B.J. Hoskins, 1978: The Life Cycles of Some Nonlinear Baroclinic Waves. *J. Atmos. Sci.*, 35, 414–432
- Simons, T.J., 1972: The Nonlinear Dynamics of Cyclone Waves. *J. Atmos. Sci.*, 29, 38–52,
- Simpson, I. R., Shaw, T. A., & Seager, R., 2014: A diagnosis of the seasonally and longitudinally varying midlatitude circulation response to global warming. *Journal of the Atmospheric Sciences*, 71(7), 2489-2515.
- Skamarock WC, Klemp JB, Dudhia J, Gill DO, Barker DM, Duda M, Huang X-Y, Wang W, Powers JG, 2008: A description of the advanced research WRF Version 3, NCAR Technical Note <http://www.mmm.ucar.edu/people/skamarock/>
- Small, R. J., and Coauthors, 2008: Air–sea interaction over ocean fronts and eddies. *Dyn. Atmos. Oceans*, 45, 274–319.
- Smith, P., P. Dare, and S. Un, 1984: The Impact of Latent Heat Release on Synoptic-Scale Vertical Motions and the Development of an Extratropical Cyclone System. *Mon. Weather Rev.*, 112, 2421–2430,
- Snyder, C. and R.S. Lindzen, 1991: Quasi-geostrophic wave-CISK in an unbounded baroclinic shear. *J. Atmos. Sci.*, 48, 78-88.

- Stoelinga, M. T., 1996: A potential vorticity-based study of the role of diabatic heating and friction in a numerically simulated baroclinic cyclone. *Mon. Weather Rev.*, 124, 849–874,
- Tan, Z., F. Zhang, R. Rotunno, and C. Snyder, 2004: Mesoscale Predictability of Moist Baroclinic Waves: Experiments with Parameterized Convection. *J. Atmos. Sci.*, 61, 1794–1804
- Terpstra A, Spengler T., 2015: An initialization method for idealized channel simulations. *Mon. Weather. Rev.* 143, 2043–2051..
- Thorncroft, C. D., Hoskins, B. J. and McIntyre, M. E., 1993: Two paradigms of baroclinic-wave life-cycle behaviour. *Q.J.R. Meteorol. Soc.*, 119: 17–55. doi:10.1002/qj.49711950903
- Trenberth, K. E., & Stepaniak, D. P., 2003: Covariability of components of poleward atmospheric energy transports on seasonal and interannual timescales. *Journal of climate*, 16(22), 3691-3705.
- Tselioudis, G., Lipat, B. R., Konsta, D., Grise, K. M., & Polvani, L. M., 2016: Midlatitude cloud shifts, their primary link to the Hadley cell, and their diverse radiative effects. *Geophysical Research Letters*, 43(9), 4594-4601.
- Tselioudis, G., & Konsta, D., 2017: The ‘Storm Curtain’ Effect: Poleward Shift of Clouds, Their Radiative Effects, and the Role of Midlatitude Storms. In *Perspectives on Atmospheric Sciences* (pp. 725-731). Springer International Publishing.
- Tyndal, J. 1861. On the absorption and radiation of heat by gases and vapours, and on the physical connexion of radiation, absorption, and conduction. *Philos. Mag.* 22:169–94, 273–85
- Ullrich, P. A., Reed, K. A. and Jablonowski, C., 2015: Analytical initial conditions and an analysis of baroclinic instability waves in  $f$  - and  $\beta$ -plane 3D channel models. *Q. J. R. Meteorol. Soc.*, 141, 2972–2988.
- American Meteorological Society, cited 2017: Extratropical Cyclone. *Glossary of Meteorology*. Available online at [http://glossary.ametsoc.org/wiki/Extratropical\\_cyclone](http://glossary.ametsoc.org/wiki/Extratropical_cyclone).
- University Corporation for Atmospheric Research MetEd COMET module, cited 2017: Mesoscale Banded Precipitation Print Version. Available online at [www.meted.ucar.edu/mesoprims/bandedprecip/print.htm#3.3](http://www.meted.ucar.edu/mesoprims/bandedprecip/print.htm#3.3)
- Wang S, Polvani LM, 2011: Double tropopause formation in idealized baroclinic life cycles: The key role of an initial tropopause inversion layer. *J Geophys Res.*, 116, D05108.
- Watterson IG , 2006: The intensity of precipitation during extra-tropical cyclones in global warming simulations: a link to cyclone intensity? *Tellus*, 58A, 82–97
- Whitaker, J. S., and C. A. Davis, 1994: Cyclogenesis in a saturated environment. *J. Atmos. Sci.*, 51, 889-907.

Willison, J., W. A. Robinson, and G. M. Lackmann, 2013: The importance of resolving mesoscale latent heating in the North Atlantic storm track. *J. Atmos. Sci.*, 70, 2234–2250

Zillman, J. W., & Price, P. G., 1972: On the thermal structure of mature Southern Ocean cyclones. *Aust. Met. Mag.*, 20, 34-48.